Complementary 2D/3D Imaging of Functional Materials using X-ray & Electron Microscopy

Zur Erlangung des akademischen Grades eines

Doktors der Naturwissenschaften
(Dr. rer. nat)

von der KIT-Fakultät für Chemie und Biowissenschaften
des Karlsruher Instituts für Technologie (KIT)

genehmigte

Dissertation

von

Yakub Fam

aus Lubuklinggau, Indonesia

Tag der mündlichen Prüfung: 13 Dezember 2019
Dekan: Prof. Dr. Manfred Wilhelm
Referent: Prof. Dr. Jan-Dierk Grunwaldt
Korreferent: Prof. Dr. Olaf Deutschmann

Zusammenfassung

Da es sich bei Katalysatoren und anderen Funktionsmaterialien im Allgemeinen um hierarchisch strukturierte Materialien handelt, ist zum Verständnis ihrer Mechanismen und zur Verbesserung ihrer Funktionsleistung bzw. katalytischen Eigenschaften eine detaillierte Charakterisierung auf verschiedenen Längenskalen und insbesondere unter Reaktionsbedingungen erforderlich. Da es keine einzige Methode gibt, die alle Längenskalen überbrückt, müssen darüber hinaus komplementäre Techniken kombiniert werden. Lokale Informationen lassen sich am besten unter Zuhilfenahme von 2D- oder besser noch 3D-mikroskopischen Verfahren erhalten. Zunächst wurden drei verschiedene 3D-Bildgebungstechniken mit nanoporösem Gold als Modellsystem evaluiert, und zwar ptychographische Röntgen-Tomographie, Elektronentomographie und der fokussierten Ionenstrahltomographie. So wurde die Vielseitigkeit der tomographischen Bildgebung inklusive aller Vor- und Nachteile beleuchtet, welches die Notwendigkeit sich ergänzender Techniken aufzeigte. Im Anschluss daran wurde quasi in situ ptychographische Tomographie genutzt, um den Einfluss thermischer Behandlung unter Atmosphärendruck zu untersuchen. Hierdurch sollte die Benutzerfreundlichkeit des durch elektronentomographische Techniken ergänzten Verfahrens im Hinblick auf In-situ-Studien hervorgehoben und dessen Leistungsfähigkeit in Bezug auf das Lösen von Problemstellungen bewiesen werden, die mittels ptychographischer Tomographie allein nicht gelöst werden können. Zur Ableitung eines weiteren wesentlichen Nutzens aus der 3DMikroskopie wurden die resultierenden 3D-Volumina auf Gaspermeabilitäts- und Diffusions-, elektrische und thermische Leitfähigkeitssimulationen angewendet. Anschließend wird über die Entwicklung zweier Zellen zur Durchführung vollständiger In-situ-Untersuchungen unter kontrollierten Temperatur- und Atmosphärenbedingungen bereichtet. Eine der Zellen wurde für reine 2D-(Röntgen-)Ptychographieexperimente mit simultaner ortsaufgelösten Röntgenfluoreszenzanalyse konzipiert. Die zweite Zelle erlaubt eine zusätzliche Option für winkelbegrenzte ptychographische 3D-Tomographieexperimente. Die Machbarkeitsprüfungen wurden mit mehreren katalytischen und funktionellen Materialien (Nanoporöses Gold, hierarchisch aufgebaut Zeolite, Kobalt-Manganoxid-Hohlkugeln) während der thermischen Behandlung unter definierten Gasatmosphären durchgeführt. Die vorliegende Arbeit hebt die Bedeutung von In-situ-Studien zur genauen Bestimmung der Behandlungstemperaturen unter definierten Bedingungen, zur Online-Visualisierung der Morphologie in 2D oder 3D und zur gleichzeitigen direkten Abbildung elementarer Verteilungen hervor. Darüber hinaus wurde an denselben Proben eine komplementäre Technik, die Transmissionselektronenmikroskopie, durchgeführt und damit ein weiterer Vorteil der Verwendung der Zellen aufgezeigt. Trotz der vorläufigen Ergebnisse der winkelbegrenzten ptychographischen In-situ-Tomographieexperimente in Bezug auf die Beschränkung der Datenrekonstruktion konnte vor Kurzem eine neue tomographische Rekonstruktionstechnik zur Extraktion von 3D-Bildern bei verkürzten Erfassungszeiten entwickelt werden. Zusammenfassend stellt die vorliegende Arbeit einen Ansatz zur ganzheitlichen Beschreibung mittels In-situ-3D-Bildgebung für die quantitative Analyse und Simulation von funktionellen Materialien dar.

Abstract

Catalysts and other functional materials are generally hierarchically structured materials. Hence, the detailed characterization at different length scales, and especially under reaction conditions, are necessary to unravel their mechanisms and to improve their performance and catalytic activities. Besides, a combination of several techniques is required to acquire complementary information owing to the lack of a single technique able to cover all the length scales. With respect to length, the best way to investigate is by microscopy either in 2D or more preferably in 3D. The work began with an exploration of three different 3D imaging techniques, i.e. ptychographic X-ray computed tomography, electron tomography, and focused ion beam slice-and view. Using nanoporous gold as the model, this study aimed to exhibit the versatility of 3D microscopy as a method beyond imaging as well as to confirm the necessity of complementary nature between them, where electron offers better spatial resolution and X-ray provides larger field of view. The study then continued by utilizing ptychographic X-ray computed tomography for *quasi in situ* thermal treatment of the same materials under atmospheric pressure. This study highlighted its ease of use of implementing *in situ* studies, complemented by electron tomography to prove its powerful ability to resolve what ptychographic tomography cannot. The resulting 3D volumes were then used for air permeability and CO_2 diffusion simulations, along with material's electrical and thermal conductivity simulations in order to further expose another excellent benefit from 3D microscopy. Ultimately, the work proceeded into developing two cells in order to perform full *in situ* investigations under controlled temperatures and atmospheres, where one cell was built for 2D only (X-ray) ptychography experiments with simultaneous X-ray fluorescence mapping, and the other was constructed with an additional capability for 3D limited-angle ptychographic tomography experiments. The feasibility tests were conducted using several functional materials, i.e. nanoporous gold, zeolite, and cobalt-manganese-oxides hollow sphere, as the models for thermal annealing process under specific atmospheres. This work eventually attests the importance of *in situ* studies in precisely determining the onset annealing temperatures under particular environments, to visualize the morphology online either in 2D or 3D, and to simultaneously map elemental distributions live. Moreover, a complementary technique via transmission electron microscopy was also demonstrated on the same sample, adding up another advantage in using the cells. Despite the preliminary results from *in situ* limited-angle ptychographic tomography experiments for limitation in data reconstruction, a new tomographic reconstruction technique was recently developed as a solution to acquire 3D images with shortened acquisition times. In conclusions, the work here converges into the ideal case of performing all-around *in situ* 3D imaging of functional materials for quantitative analysis and simulation.

Content

Zusammenfassung i

Abstract iii

Content v

List of Figures vii

List of Tables xiii

List of Abbreviations xv

Acknowledgment xvii

1 Introduction 1
- 1.1 Electron imaging techniques 3
  - 1.1.1 Dual-beam focused ion beam and scanning electron microscopy (FIB-SEM) 4
  - 1.1.2 Focused ion beam slice and view (FIB-SV) 5
  - 1.1.3 Transmission electron microscopy (TEM) 6
  - 1.1.4 Electron tomography (ET) 7
- 1.2 X-ray imaging techniques 7
  - 1.2.1 X-ray ptychography (XRP) 8
  - 1.2.2 Ptychographic X-ray computed tomography (PXCT) 9
  - 1.2.3 X-ray fluorescence microscopy (XRF) 9
- 1.3 Complementary X-ray (XRM) & electron microscopy (EM) 10
- 1.4 *In situ* EM and XRM 12
- 1.5 Sample preparation for electron and/or X-ray microscopy 17
- 1.6 Motivation and aim of dissertation 20

2 Multimodal *ex situ* 3D imaging studies of nanoporous gold 23
- 2.1 Background 23
- 2.2 Experimental 24
  - 2.2.1 Sample preparation 24
  - 2.2.2 Three tomographic studies 26
  - 2.2.3 Image processing and analysis 28
- 2.3 Results and Discussion 29
- 2.4 Conclusions 35

3 *Quasi in situ* 3D imaging study of thermal annealing of npAu 37
- 3.1 Background 37
- 3.2 Experimental 38
  - 3.2.1 Sample preparation 38
  - 3.2.2 *Quasi in situ* PXCT with sequential heating experiment 38
  - 3.2.3 Complementary ET measurement 39
  - 3.2.4 Data processing 39
  - 3.2.5 Numerical tomography-based simulations 40
- 3.3 Results and Discussion 42

3.4 Conclusions 56

4 *In situ* 2D/3D imaging studies of functional materials 57

4.1 Background 57

4.2 Experimental 58

4.2.1 Sample preparation and mounting 58

4.2.2 *In situ* XRP and PXCT studies 61

4.2.3 Gas flow simulation of 2G/3G cells 62

4.2.4 Data processing 62

4.3 Cell Design and Simulation 63

4.4 Case Studies 67

4.4.1 *In situ* sintering of Au colloids – early cell prototypes using 2G cell 67

4.4.2 *In situ* annealing of npAu materials in controlled gas environment using 2G cell 68

4.4.3 Rotational angle test of 3G cell for *in situ* limited-angle PXCT experiments 77

4.4.4 *In situ* annealing of $CoMnO_2$-HS in controlled gas environment using 3G cell 79

4.5 Conclusions 81

5 General Conclusions and Outlook 83

Bibliography 85

Author Contributions 101

List of Figures

Figure 1.1: Illustration of multi-scalar feature of catalysts or functional materials from atomic to macro scale. Adapted with permission from Ref (SCM 2019). 1

Figure 1.2: Principles and results between 2D and 3D imaging methods. 3

Figure 1.3: Illustration of beam paths and optical configuration in (a) FIB column and (b) SEM column; (c) geometric positions of FIB column, SEM column, and sample stage at 52° and eucentric point in FIB-SEM instrument. Adapted with permission from Ref (Meng-Burany 2010). 4

Figure 1.4: Illustration of the optimized sample geometry for FIB-SV using dual beam microscope. Adapted with permission from Ref (Holzer and Cantoni 2012). 5

Figure 1.5: Illustration of beam paths and optical configurations between (left) optical microscope and TEM under (middle) imaging mode and (right) diffraction mode. Adapted with permission from Ref (JEOL 2019). 6

Figure 1.6: Image acquisition process in ET, where images are obtained by a tilt series at a single tilt axis to generate 2D image projections. Adapted with permission from Ref (Weyland and Midgley 2004). 7

Figure 1.7: Illustration of the path of X-ray beam and experimental configuration of XRP. Adapted with permission from Ref (Thibault, Dierolf et al. 2008). 8

Figure 1.8: Illustration of the X-ray beam path and experimental configuration of PXCT. Adapted with permission from Ref (Dierolf, Menzel et al. 2010). 9

Figure 1.9: *In situ* TEM MEMS-based setup: a) Sample holder. (b) Nanoreactor inserted in the sample holder. The lid of the holder is removed for a better view. (c) Schematic diagram of the nanoreactor inserted in the sample holder (Yokosawa, Alan et al. 2012). ETEM setup: d) Schematic diagram of a differentially-pumped TEM column. Adapted with permission from Ref (Hansen, Wagner et al. 2010). 13

Figure 1.10: (a,b,d–f) *In situ* atomic-scale TEM observation of the catalyst splitting during the course of CNT growth; insets of (d–f) show FFTs from the indicated areas. (c) Schematic drawing of an elongated particle bonded with CNT layers. Scale bar is 20 nm. Adapted with permission from Ref (Huang, Farra et al. 2019). 14

Figure 1.11: ETEM analyses of the growth of surface shell on TiO_2 particles and the formation of H_2 nanobubble after UV light illumination. (a) A liquid ETEM setup with an *in situ* illumination and a liquid sample injection containing water-immersed TiO_2 particles. (b) TEM images of TiO_2 particles during photocatalysis at different times. Red arrows indicate the gas bubbles surrounding TiO_2 particles. (c) Zoomed-in images in (b). Green arrows indicate the surface shells growing and covering TiO_2 particles with times. Adapted with permission from Ref (Lu, Yin et al. 2018). 15

Figure 1.12: Scanning transmission X-ray microscopy contours of Fischer–Tropsch catalysts (a) at room temperature, (b) after reduction in H_2 at 350 °C, and (c) after CO hydrogenation at 250 °C. X-ray absorption near-edge spectroscopy spectra at (d, f, h) Fe L_2 and L_3 edges. Adapted with permission from Ref (de Smit, Swart et al. 2008). 16

Figure 1.13: Scheme of sample preparation for cross section TEM observation. 18

Figure 1.14: Method to prepare a plan-view specimen from a specific site based on the microsampling technique. Adapted with permission from Ref (Mayer, Giannuzzi et al. 2007). 19

Figure 1.15: Thickness difference of amorphous layer of Si using FIB voltages of (a) 30 kV, (b) 5 kV, and (c) 2 kV, resulting in amorphous layers of (a) 22 nm, (b) 2.5 nm, and (c) 0.5-1.5 nm thickness, respectively. Adapted with permission from Ref (Mayer, Giannuzzi et al. 2007). 20

Figure 2.1: Overview of CeO_2/npAu sample preparation for ET, PXCT, and FIB-SV (Fam, Sheppard et al. 2018). 24

Figure 2.2: Monolithic CeO_2/npAu was mounted on a stub and cut by Ga^+ beam. A small piece of material was extracted by FIB manipulation (Fam, Sheppard et al. 2018). 25

Figure 2.3: The CeO_2/npAu piece extracted from the stub was moved to a lift-out grid by FIB manipulation. This piece was then thinned down by Ga^+ beam to <300 nm thickness for ET measurement (Fam, Sheppard et al. 2018). 25

Figure 2.4: (Left) Customized Cu pin developed at cSAXS beamline (Swiss Light Source); (Middle-Right) a small piece of CeO_2/npAu from the lift-out grid was moved to the Cu pin by FIB manipulation, which was then cut into a cylindrical shape for PXCT measurement (Fam, Sheppard et al. 2018). 25

Figure 2.5: The remaining CeO_2/npAu on the stub (Figure 2.2) was cut into a rectangular prism by Ga^+ beam for FIB-SV measurement (Fam, Sheppard et al. 2018). 26

Figure 2.6: Illustration of PXCT setup at the cSAXS beamline, CH (Fam, Sheppard et al. 2018). 27

Figure 2.7: Illustration of ET setup at the INT, DE (Fam, Sheppard et al. 2018). 27

Figure 2.8: Illustration of FIB-SEM-CT setup at the LEM, DE (Fam, Sheppard et al. 2018). 28

Figure 2.9: 2D perspective of CeO_2/npAu from: (a) PXCT - orthographic slice through the phase contrast tomogram following reconstruction; (b) FIB-SV - secondary electron image of a typical surface exposed during cutting; (c) STEM image of CeO_2/npAu and (d) corresponding EDX spectrum acquired from the shaded area. (Fam, Sheppard et al. 2018) 30

Figure 2.10: Volume rendering of (a) whole and (b) bisected CeO_2/npAu pillar via PXCT; (c) whole and (d) bisected CeO_2/npAu cuboid via FIB-SV; (e) CeO_2/npAu lamella to scale (above) and magnified (below) via ET. Ortho slice planes indicated by red lines. (Fam, Sheppard et al. 2018) 31

Figure 2.11: Normalised distribution profile of (a) pore size and (b) ligament size of CeO_2/npAu from three techniques. (Fam, Sheppard et al. 2018) 32

Figure 2.12: Subvolume extraction from: (a) PXCT data and (b) selection of four PXCT subvolumes; (c) FIB-SV data and (d) selection of four FIB-SV subvolumes. All subvolumes had dimensions of 0.5*0.5*0.5 μm^3 and are highlighted in blue, volumes (b) and (d) were rendered with transparency. (Fam, Sheppard et al. 2018) 34

Figure 3.1: PXCT volume rendering of (a,b) full and (c,d) trimmed npAu sample with (e,f) pore network model before (a,c,e) and after (b,d,f) heating at 450 °C. The scalebars are 1 µm. (c,d) npAu is in yellow and pore in blue. (g) Illustration of field of view before (i) and after heating at 450 C (ii). 43

Figure 3.2: FSC for the tomograms of npAu samples before (a) and after heating at 450 °C (b) from Figure 3.1. 43

Figure 3.3: PXCT volume rendering of (a,d,g) full and (b,e,h) trimmed npAu sample with its (c,f,i) pore network model and (j) pore size distribution plot before (a-c) and after (d-f) heating at 550 °C and (g-i) 750 °C. The scalebars are 1 µm. (b,e,h) npAu is colored in yellow, whereas pore in blue. 44

Figure 3.4: FSC for the tomograms of npAu before (a) and after heating at 550 °C (b) and 750 °C (c) in Figure 3.2; CeO_2/npAu before (d) and after heating at 550 °C (e) and 750 °C (f) in Figure 3.7; $CeTiO_x$/npAu before (g) and after heating at 550 °C (h) and 750 °C (i) in Figure 3.12. 45

Figure 3.5: ET volume rendering (a) and (b) pore size distribution plot of npAu lamella (yellow = npAu and blue = pore) at room temperature. 46

Figure 3.6: PXCT volume rendering of (a,c,e) full and (b,d,f) trimmed CeO_2/npAu sample with (g) pore distribution graph before (a,b) and after (c,d) heating at 550 °C and (e,f) 750 °C. The scalebars are 1 µm. (b,d,f) CeO_2/npAu is colored in yellow, whereas pore in blue. 47

Figure 3.7: ET volume rendering of CeO_2/npAu lamella (a) at room temperature, only npAu (b), only CeO_2 particles (c) and the particle size distribution graph (d). Yellow-rendered object is npAu and blue-rendered object is CeO_2. 48

Figure 3.8: PXCT volume rendering of (a,d,g) full and (b,e,h) trimmed $CeTiO_x$/npAu sample with its (c,f,i) pore network model and (j) pore size distribution plot before (a-c) and after (d-f) heating at 550 °C and (g-i) 750 °C. The scalebar is 1 µm. (b,e,h) npAu is colored in yellow, whereas pore in blue. 49

Figure 3.9: PXCT volume rendering of a block pure npAu (a, i, q), cropped from the sample in Figure 3.3b/d/f, before (a-h) and after heating at 550 °C (i-p) and 750 °C (q-x). Fluid flow profile (b,j,r), pressure mapping (c,k,s), voltage mapping (d,l,t), CO_2 concentration profile (e,m,u), and temperature mapping (g,o,w) in a slice form and whole volume (f,n,v,h,p,x) from absolute permeability (b,j,r,c,k,s), electrical conductivity (d,l,t), molecular diffusivity (e,m,u,f,n,v), and thermal conductivity (g,o,w,h,p,x) simulation through the pore (blue in a,i,q). 52

Figure 3.10: PXCT volume rendering of a block CeO_2/npAu (a, i, q), cropped from the sample in Figure 3.6b/d/f, before (a-h) and after heating at 550 °C (i-p) and 750 °C (q-x). Fluid flow profile (b,j,r), pressure mapping (c,k,s), voltage mapping (d,l,t), CO_2 concentration profile (e,m,u), and temperature mapping (g,o,w) in a slice form and whole volume (f,n,v,h,p,x) from absolute permeability (b,j,r,c,k,s), electrical conductivity (d,l,t), molecular diffusivity (e,m,u,f,n,v), and thermal conductivity (g,o,w,h,p,x) simulation through the pore (blue in a,i,q). 54

Figure 3.11: PXCT volume rendering of a block $CeTiO_x$/npAu (a, i, q), cropped from the sample in Figure 3.8b/d/f, before (a-h) and after heating at 550 °C (i-p) and 750 °C (q-x). Fluid flow profile (b,j,r), pressure mapping (c,k,s), voltage mapping (d,l,t), CO_2 concentration profile (e,m,u), and temperature mapping (g,o,w) in a slice form and whole volume (f,n,v,h,p,x) from absolute permeability (b,j,r,c,k,s), electrical conductivity (d,l,t), molecular diffusivity (e,m,u,f,n,v), and thermal conductivity (g,o,w,h,p,x) simulation through the pore (blue in a,i,q). 55

Figure 4.1: Overview of npAu sample preparation on the MEMS chip via FIB (Fam, Sheppard et al. 2019). 59

Figure 4.2: Initial npAu extraction on a SEM stub to make a block for several samples (Fam, Sheppard et al. 2019). 59

Figure 4.3: Final cut after transfer to intermediate lift-out grid and thinning of block into a wedge (Fam, Sheppard et al. 2019). 60

Figure 4.4: Transfer and deposition of the wedge on the MEMS chip (Fam, Sheppard et al. 2019). 60

Figure 4.5: SEM images obtained during FIB preparation on Wildfire chips at DESY NanoLab: (a) ZSM5 crystal and (b) zoom in of the highlighted area; (c) npAu wedge and (d) zoom in of the highlighted area; (e) $CoMnO_2$-HS crystal and (f) zoom in of the highlighted area (Fam, Sheppard et al. 2019). 60

Figure 4.6: Illustration of the *in situ* setup for 2D and 3D ptychography at the P06 nanoprobe endstation of PETRA III 64

Figure 4.7: Illustration of disassembled 2G (right) and 3G (left) cell with their internal gas-flow volumes (highlighted above). The fully assembled setups are shown below (Fam, Sheppard et al. 2019). 64

Figure 4.8: Internal gas-flow volume and simulation of 2G cell (left) and 3G cell (right) (Fam, Sheppard et al. 2019). 65

Figure 4.9: Plot of temperature readout vs time via the integrated temperature control system, recorded during thermal annealing study of npAu sample. The valley between the fourth and fifth hour of the measurement resulted from pausing the experiment due to loss of beam (Fam, Sheppard et al. 2019). 66

Figure 4.10: XRP images (top) and Au fluorescence maps (bottom) during thermal annealing of colloidal Au: (a) room temperature (293 K), (b) 423 K, (c) 573 K, (d) 723 K, and (e) 773 K. Dark spots in phase maps and high-count zones in fluorescence maps indicate areas most rich in Au. Scale bars = 500 nm (Fam, Sheppard et al. 2019). 67

Figure 4.11: FRC of the ptychogram of AuNP (Fam, Sheppard et al. 2019). 68

Figure 4.12: Ptychography images from thermal annealing of np-Au under He environment. Overview scans: (a) before and (b) after thermal annealing. Highlighted area in (a-b) shown: (c) at 293 K, (d) 923 K after 0 min, (e) 923 K after 15 min, (f) 923 K after 30 min. Darker intensity in phase maps indicates areas rich in Au, while brighter voids indicate annealing and absence of Au ligaments. Pt glue from FIB is visible as intense features in the corners of (a-b) (Fam, Sheppard et al. 2019). 69

Figure 4.13: TEM images of np-Au: (a) before *in situ* thermal annealing and (b) zoom in on the highlighted area; (c) after *in situ* thermal annealing at 923 K and (d) zoom in on the highlighted area (Fam, Sheppard et al. 2019). 70

Figure 4.14: TEM-EDX data recorded on the nanoporous gold sample used for *in situ* ptychography. Analysis shows the presence of minor Si and Pt contaminants close to the Au ligament edges (Fam, Sheppard et al. 2019). 70

Figure 4.15: Lattice spacing measurement of fresh np-Au sample (highlighted area) via bright-field high resolution TEM, indicating d = 0.236 nm, belonging to (1 1 1) plane of Au metal (PDF 99-0056) (Fam, Sheppard et al. 2019). 71

Figure 4.16: Lattice spacing measurement of fresh np-Au sample (between indicated points) via selected area electron diffraction, indicating d = 0.234 nm, belonging to (1 1 1) plane of Au metal (PDF 99-0056) (Fam, Sheppard et al. 2019). 72

Figure 4.17: XRP images from thermal annealing of CeO_2/npAu under He environment at (a) 20 °C, (b) 600 °C, (c) 650 °C, (d) 660 °C, (e) 700 °C, and (f) 810 °C. The scalebar is 1 µm. 73

Figure 4.18: XRP images from thermal annealing of TiO_2/npAu under He environment at (a) 20 °C, (c) 600 °C, (d) 780 °C, and (f) its overview scan at 780 °C. Ti-signal XRF mapping (b) from the highlighted area in (a); (e) from the highlighted area in (d). The scalebar is 1 µm, except 5 µm in (f). 74

Figure 4.19: XRP images from thermal annealing of CeO_2/npAu under O_2/He environment at (a) 20 °C, (b) 550 °C, (c) 600 °C, (d) 800 °C, and (f) its overview scan at 800 °C. (e) Ce-signal XRF mapping from the highlighted area in (d). The scalebar is 1 µm, except 5 µm in (f). 75

Figure 4.20: XRP images from thermal annealing of TiO_2/npAu under O_2/He environment at (b) 20 °C, (d) 900 °C, and (e) 1300 °C. An overview scan at (a) 20 °C and (g) 800 °C. Ce-signal XRF mapping (c) from the highlighted area in (b); (f) from the highlighted area in (e). The scalebar is 1 µm, except 5 µm in (f). 76

Figure 4.21: FRC for the ptychograms of npAu under He (a) in Figure 4.12, CeO_2/npAu under He (b) in Figure 4.17 and O_2/He (c) in Figure 4.18, TiO_2/npAu under He (d) in Figure 4.19 and O_2/He (e) in Figure 4.20. 77

Figure 4.22: Tilting angle tests using micro/macroporous zeolite as a case study: (a) illustration of the 3G cell with corresponding SEM image of the zeolite crystal on a MEMS chip, and ptychograms of the specimen at tilting angles with respect to the incident beam: (b) 35°, (c) 15°, (d) 0°, (e) -15°, (f) -35°. Dark spots in phase maps indicate areas rich in Si/Al. Pt-glue is visible as the dark region in the upper left of each image (Fam, Sheppard et al. 2019)....................78

Figure 4.23: Single slice following tomographic reconstruction of the hierarchical zeolite sample from limited-angle data by: (a) an in-house deep learning method (under development at P06); (b) SART from the “scikit-image” Python package; (c) SIRT from the TomoJ plugin of FIJI software; (d) MLEM from the “TomoPy” Python toolbox (Fam, Sheppard et al. 2019). 79

Figure 4.24: Ptychograms of $CoMnO_2$-HS during thermal treatment under He atmosphere at (a) 20 °C, (b) 130 °C, (c) 200 °C, (d) 410 °C, (e) 500 °C, (f) 720 °C, and (g) 1000 °C. All scale bars are 1 µm....................80

Figure 4.25: Tomogram slices of $CoMnO_2$-HS before (a,d) and after thermal treatment at 410 °C (b,e) and 1000 °C (c,f) via tomographic reconstruction by TomoJ plugin of FIJI software, where the views were performed in the form of (a-c) axial section and (d-f) sagittal section. The red dashed lines indicate the sagittal slices of (a-b). All scale bars are 1 µm....................81

List of Tables

Table 1: Measurement of volume-rendered CeO_2/npAu from three techniques. (Fam, Sheppard et al. 2018) 32

Table 2: Calculated physical properties of CeO_2/npAu following tomographic label analysis. (Fam, Sheppard et al. 2018) 34

Table 3: Physical properties derived from rendering data volumes of PXCT in Figure 3.3, 3.6, and 3.8. 45

Table 4: Intrinsic material properties derived from simulation of 3D-rendered data volumes in Figure 3.9-11. 50

Table 5: Experimental parameters during XRP studies at P06 beamline of PETRA III (Fam, Sheppard et al. 2019) 61

Table 6: Quantification of EDX spectra in Figure 4.14 (Fam, Sheppard et al. 2019). 71

List of Abbreviations

1/2/3/4G	First/Second/Third/Fourth Generation
BMBF	Federal Ministry of Education and Research
DESY	German Electron Synchrotron
EDX	Energy X-ray Dispersive Spectroscopy
EELS	Electron Energy Loss Spectroscopy
EM	Electron Microscopy
ET	Electron Tomography
ETEM	Environmental Transmission Microscopy
FIB	Focused Ion Beam
FIB-SV	Focused Ion Beam Slice and View
flOMNI	Flexible Tomography Nanoimaging Endstation
FRC	Fourier Ring Correlation
FSC	Fourier Shell Correlation
FZP	Fresnel Zone Plate
GIS	Gas Injection System
IMVT	Institute for Micro Process Engineering
INT	Institute of Nanotechnology
ITCP	Institute for Chemical Technology and Polymer Chemistry
KIT	Karlsruhe Institute of Technology
KNMF	Karlsruhe Nano Micro Facility
LEM	Laboratory for Electron Microscopy
MEMS	Micro-Electromechanical Systems
MLEM	Maximum Likelihood Expectation Maximization
MS	Mass Spectrometry
PSI	Paul Scherrer Institute
PXCT	Ptychographic X-Ray Computed Tomography
S.A.	Surface Area
SAED	Selected Area Electron Diffraction
SART	Simultaneous Algebraic Reconstruction Technique
SEM	Scanning Electron Microscopy
SIRT	Simultaneous Iterative Reconstruction Technique
SLS	Swiss Light Source
STEM	Scanning Transmission Electron Microscopy
STXM	Scanning Transmission X-Ray Microscopy
TEM	Transmission Electron Microscopy
Vp	Pore volume
XRD	X-Ray DIffraction
XRF	X-Ray Fluorescence
XRM	X-Ray Microscopy
XRP	X-Ray Ptychography
Z	Atomic Number

Acknowledgment

I would like to thank the following persons during my research works:

- Prof. Jan-Dierk Grunwaldt, for providing the dissertation topic, guidance and discussion in experiments, preparing journal articles and dissertation, beamtime proposals writing and approval, travel allowance for conferences and RACIRI2018 summer school at Rügens Island.
- Dr. Thomas Sheppard, for guidance and discussion in experiments, preparing journal articles and dissertation, beamtime proposals writing and approval.
- Dr. Torsten Scherer, Dr. Sabine Schlabach, and Dr. Peter Marek, for training and authorizing a full access in using focused ion beam Strata 400S at the INT-KIT.
- Dr. Wang Di, Dr. Wang Wu, Ms. Xiaohui Huang, for training and a limited access in using transmission electron microscope Titan 80-300 at the INT-KIT.
- Prof. Christian Schroer, Dr. Andreas Schropp, Mr. Dennis Brükner, Mr. Maik Kahnt, Mr. Martin Seyrich, Mr. Felix Wittwer, Dr. Jan Garrevoet, Dr. Xiaogang Yang, Dr. Mikhail Lyubomirskiy, Dr. Johanness Hagemann, Ms. Christina Ossig, and Ms. Saba Alizadehfanaloo, for contribution in the beamtimes of X-ray ptychography and ptychographic X-ray computed tomography setup at the P06 beamline (DESY).
- Dr. Ana Diaz, Dr. Johannes Ihli, Dr. Michal Odstrcil, and Dr. Mirko Holler, for contribution in the beamtimes of ptychographic X-ray computed tomography at the cSAXS beamline (SLS-PSI).
- Mr. Dennis Scherhaufer and Mr. Heinz Lambach, for fabricating the *in situ* cells at the IMVT-KIT.
- Mr. Satishkumar Kulkarni and Dr. Thomas Keller, for a limited access in using focused ion beam SCIOS at the DESY Nanolab.
- Mr. Johannes Becher and Mr. Sebastian Weber, for contribution in the beamtimes at DESY and SLS.
- Dr. Sina Baier, for introducing the works at the beginning, a few months in 2016.
- Dr. Patrice Brenner, for focused ion beam slice and view measurement at CFN-KIT.
- Dr. Arne Wittstock, for providing nanoporous gold samples and obtaining the KNMF proposals approval.
- Prof. Wilhelm Schwieger, for providing zeolite samples.
- Prof. Claus Feldmann, for providing cobalt-manganese-oxide hollow spheres samples.
- AK Grunwaldt, for the working environment.
- KIT and German's Federal Ministry of Education and Research, "MicTomoCat" (05K16VK1), for financial support of the project.
- DESY, SLS, and KNMF, for the beamtime access.
- Internet and the person who found it. Without them, literature review and learning would be much more difficult and time-consuming.
- Capsaicin and the person who found it. Without them, PhD life would feel flat.
- Prof. Toyoko Imae, Dr. Shammi Akter Ferdousi, and Dr. Alba Estrella Díaz Álvarez, for their second-chance, support, and faith in me.
- Ms. Faiza Maryani, Mrs. Yuliana Tassia, Dr. Ghazal Tofighi, and other friends in Lubuklinggau, Jakarta, Bandung, Taipei, Hong Kong, Xi'an, Madrid, and Karlsruhe, for their support.
- My family in Indonesia for their continuous and unconditional support and love.

Karlsruhe, 20 December 2019

Yakub Fam

1 Introduction

One of the most important technology in this world is catalysis as chemicals are mostly derived from catalytic reactions (Chorkendorff and Niemantsverdriet 2003), which require catalysts to optimally work for economical purposes. The necessary ways to realize such a demand are by understanding how catalysts function and investigating why they deactivate. In the branch of heterogeneous catalysis, where the phase of the catalyst (generally solid) is not the same with that of the reactant (liquid/gas), researching the catalyst structure with high surface area and porosity as well as the dynamics are required to optimize the catalytic activity by analyzing the structure-activity relationships (Chorkendorff and Niemantsverdriet 2003, Somorjai and Li 2010). The techniques for that purpose are usually divided into: scattering methods, spectroscopy, and microscopy, which are greatly utile if they are performed across multiple timescales – from the diffusion of reactants to the deactivation of active sites – as well as multiple length scales – from the active sites in an atomic scale to the reactor in a meter scale (Niemantsverdriet 2007, Grunwaldt and Schroer 2010, Che and Védrine 2012).

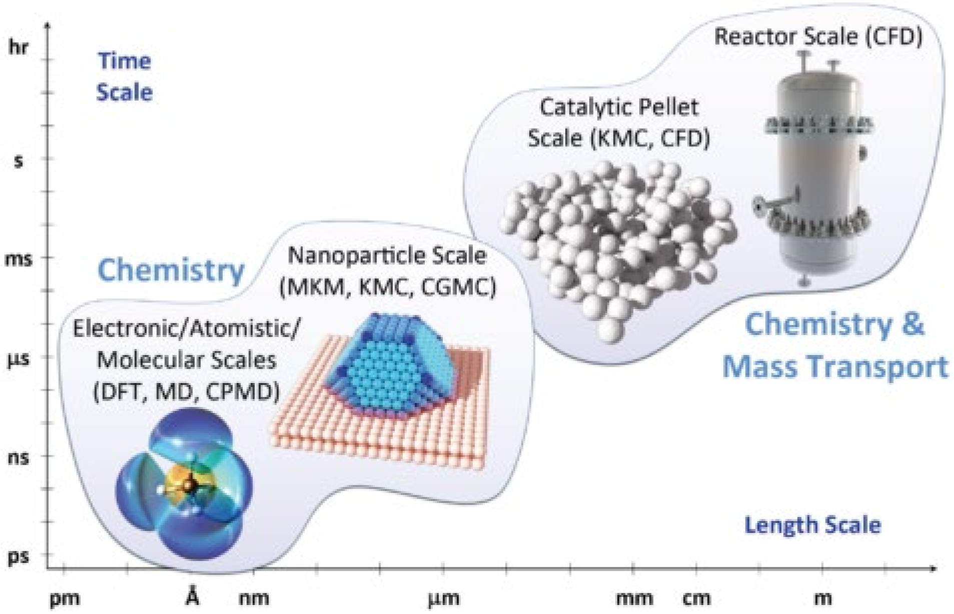

Figure 1.1: Illustration of multi-scalar feature of catalysts or functional materials from atomic to macro scale. Adapted with permission from Ref (SCM 2019).

Since solid catalysts are commonly used in heterogenous catalysis, the catalyst design to incorporate certain microstructures are necessary for the sake of optimization in their activities (Ng, Gani et al. 2006) although the original source of the activities is on the active sites in the atomic scales (Figure 1.1). The catalysts are usually the active materials filled on the support materials or carriers and produced with particular geometries (e.g. pellet) in a large amount as the industrial plants are in the meter ranges. In the macro scale (from mm to cm), the evaluation of different carrier shapes and reactor modelling are important in optimizing the heat and mass transfer as well as the catalytic activity (Deutschmann 2012). In the micro- (< mm) and meso (20-500 nm) scales, the catalyst porosity also takes into account in affecting the heat and mass transport phenomena (Vantomme, Léonard et al. 2007) and the modelling approach is a key step to comprehend and correlate it to the catalytic activity (Matera and Reuter 2012), where tuning catalysts with different pore sizes (Klumpp, Zeng et al. 2016) or hierarchical structures (Güttel 2015) would optimize the catalyst performance. In the nanoscale (sub-nm to 20 nm), the interaction of catalyst with fluid reactants is the focus here, along with the fact that catalyst morphology and size play roles in tuning the catalytic activity (Ketchie, Fang et al. 2007, Hansen, DeLaRiva et al. 2013). Last the most important process in catalysis happens in the atomic scale (< sub nm) (Chorkendorff and Niemantsverdriet 2003, Grunwaldt, Wagner et al. 2013), where the catalytic reactions occur on the catalyst active sites starting from the adsorption of the reactants to the desorption of the products.

Furthermore, the investigation of catalysts during operation, which is a particular condition to trigger the desired catalytic reaction, is also important in order to eventually evaluate their catalytic activities (Haw 2002, Weckhuysen 2004, Grunwaldt, Wagner et al. 2013). As many catalytic reactions often involve harsh working conditions, e.g. high pressures and temperatures, the singular implementation of the above techniques (scattering methods, spectroscopy, and microscopy) is therefore limited, bringing on the fact that there is not any single method able to fulfil the needs to characterize the catalysts, so the interchangeable uses between the techniques and the application of hierarchical approaches (Basile, Benito et al. 2010, Grunwaldt and Schroer 2010, Grunwaldt, Wagner et al. 2013, Kalirai, Boesenberg et al. 2015) are thus realized.

Electron- and X-ray-based methods, among other techniques, are notable and versatile in characterizations of catalysts, especially for the solid ones. Although electron is a preferred light source for probing catalysts in higher spatial resolutions due to its lower wavelength and easiness to focus by lenses, X-ray on the other hand is able to probe larger sizes of catalysts for more representation of the bulk materials due to its higher penetration depth. This makes both techniques actually complementary to each other and such combination is fruitful in probing the same sample to produce hierarchical length scale results (Fam, Sheppard et al. 2018, Li, Ihli et al. 2019). Furthermore, despite the lower spatial resolutions of X-ray, it has the flexibility to cover a wide range of working pressure, whereas electron generally works under vacuum condition. Further discussion in this matter can be found in Section 1.4. This reason indicates that X-ray offers more suitability and ease of use for studies under working condition, also known as *in situ* or *operando* studies.

The term “in situ”, a Latin word for “on site”, and “operando”, a Latin word for “working/operating”, have been unanimously established, particularly in the field of catalysis, with a specific meaning referring to a study of the catalyst under realistic reaction conditions, but “operando” possesses an additional significance, which includes a simultaneous online measurement of catalytic performance via mass spectrometry or gas chromatography (Topsøe 2003, Thomas and Hernandez-Garrido 2009, Grunwaldt, Wagner et al. 2013, Whiting, Meirer et al. 2017). The necessity to carry out *in situ*/*operando* studies stems from the facts that most catalysts typically operate under specific environmental conditions, where chemistry and structure of materials alter or become unstable so that intermediate states/agents exist and some have profound effects on the catalytic activities (Ertl, Knözinger et al. 2008, Somorjai and Li 2010). *In situ*/*operando* studies are hence able to help in revealing such information only present under those specific reaction conditions, which are useful to unravel the relationship between surface structure, materials composition, and catalytic activity (Grunwaldt, Kimmerle et al. 2009, Schroer and Grunwaldt 2009, Thomas and Hernandez-Garrido 2009, Weckhuysen 2009, Beale, Jacques et al. 2010, de Groot, de Smit et al. 2010, Grunwaldt and Schroer 2010, Stavitski and Weckhuysen 2010, Tao and Salmeron 2011, Andrews and Weckhuysen 2013, Grunwaldt, Wagner et al. 2013, Tao and Crozier 2016, Kalz, Kraehnert et al. 2017, Newton 2017).

Among the aforesaid three techniques, *in situ*/*operando* microscopy offers more advantages because of the capability to visualize the morphology of catalysts in the form of real images together with complementary spectroscopic and scattering results (Schroer and Grunwaldt 2009, de Groot, de Smit et al. 2010, Grunwaldt and Schroer 2010, Nelson Weker and Toney 2015, Tao and Crozier 2016, Weker, Huang et al. 2016). Therefore, a comprehensive set of results can be generated from microscopy, whereas the other two methods are not able to deliver what only microscopy can, which are real images both in two dimensions (2D) and/or even three dimensions (3D). In comparison between 2D and 3D microscopy, the 3D imaging techniques provide more information and derivable results than the 2D counterpart. Not only structural parameters can be obtained, but also the quantitative results useful in catalysis, e.g. surface area, porosity, and mass density, can also be extracted (da Silva, Mader et al. 2015, Cuesta, De la Torre et al. 2017, Ihli, Jacob et al. 2017, Zabihzadeh, Van Petegem et al. 2017, Fam, Sheppard et al. 2018) and even further utilized for simulation/modelling (Zabihzadeh, Cugnoni et al. 2017, Cuesta, De la Torre et al. 2019). Aside from that, the accurate depiction of the probed objects is also a big concern for the results of 2D imaging techniques since the only one perspective may give a wrong impression on the real objects as shown in Figure 1.2, but it does not happen to 3D imaging methods because many projections at different perspectives are collected to generate 3D volumes, of which the resemblance to the real objects only depends on the spatial resolution of the corresponding techniques. Further discussion in this matter can be found in Section 1.5.

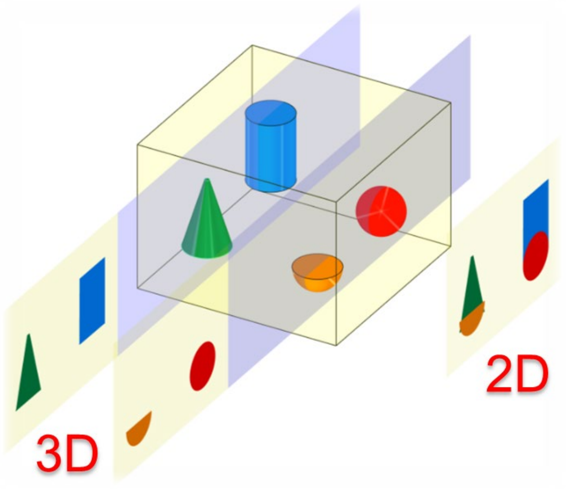

Figure 1.2: Principles and results between 2D and 3D imaging methods.

1.1 Electron imaging techniques

Electron imaging has been the most widespreadly used methods to characterize functional materials and catalysts in nano- and even atomic scales. There are various techniques under this category, i.e. scanning electron microscopy, transmission electron microscopy, reflection electron microscopy, scanning tunnelling microscopy. The following techniques were the focused subjects since they were used oftentimes either to prepare the samples for imaging experiments or to be the main imaging studies themselves. All electron imaging studies described in this dissertation were performed *ex situ* because of the complementary purpose to the highlighted X-ray imaging method.

1.1.1 Dual-beam focused ion beam and scanning electron microscopy (FIB-SEM)

Dual-beam focused ion beam and scanning electron microscopy (FIB-SEM) instrument includes an ion column, an electron column in a conventional SEM chamber, a gas injection system (GIS), a micromanipulator, a sample stage, and detectors. Both columns primarily consist of beam guns, apertures, detectors, and lenses with schematic details in Figure 1.3a-b. The beam guns comprise beam sources to emit the beams, suppressors and extractors to adjust the brightness, whereas the apertures and lenses play the role to focus the beams. The differences between both columns are the beam sources (liquid Ga for FIB and W crystal for SEM) and the type of lens (electrostatic for FIB and electromagnetic for SEM) (Hirsch, Howie et al. 1977, Goldstein, Newbury et al. 2003, Scientific 2019). For what it is worth, the dual beam configuration makes a typical geometry between FIB and SEM column as well as the sample holder within the chamber as shown in Figure 1.3c. While the SEM column stands vertically, the FIB column is positioned 52° relative to the SEM column, and the sample stage can be moved in the x, y, z directions with rotation up to 360° and tilting up to 60°. Moreover, the sample stage has an eucentric point, where both ion and electron beam intersect on the same area of the sample. This allows a cross-section imaging by tilting the sample to 52° from electron beam, with simultaneously perpendicular cutting of the sample using ion beam (Alton and Read 1989, Giannuzi and Stevie 2005). For the results, 2D images can be obtained from both columns, where the resulting secondary electrons are used for SEM images and secondary ions for FIB images. However, it should be noted that FIB image acquisition is quite damaging to the sample.

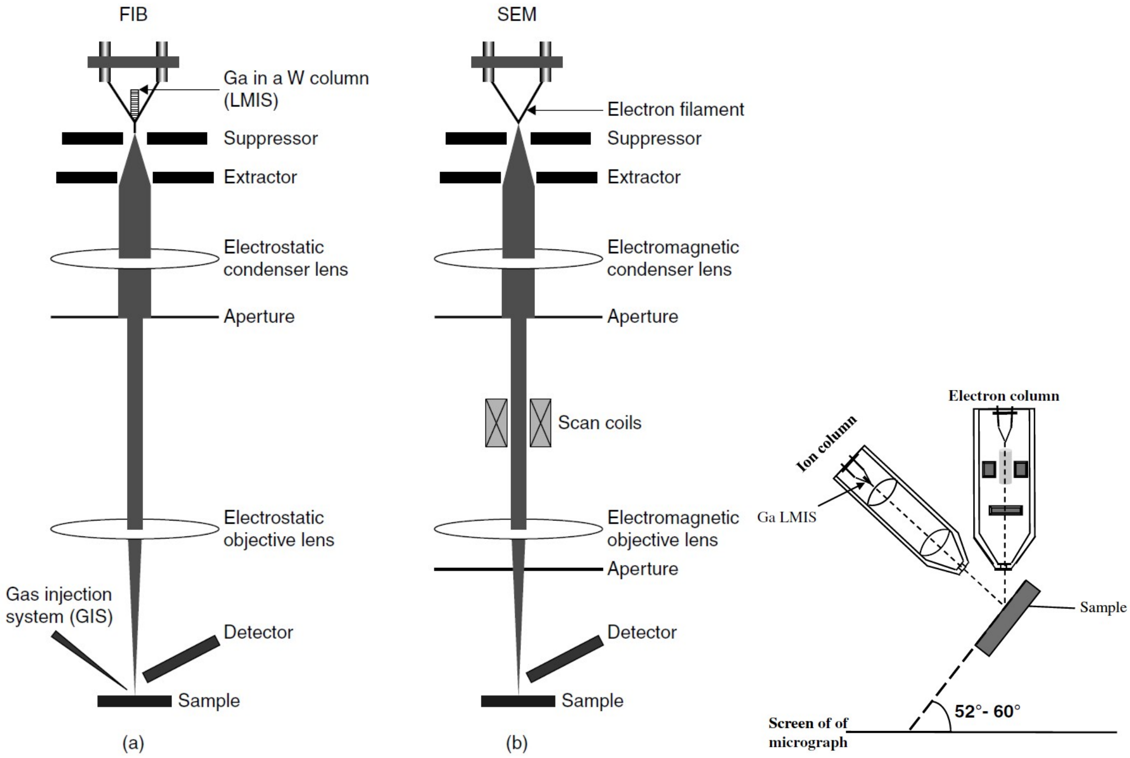

Figure 1.3: Illustration of beam paths and optical configuration in (a) FIB column and (b) SEM column; (c) geometric positions of FIB column, SEM column, and sample stage at 52° and eucentric point in FIB-SEM instrument. Adapted with permission from Ref (Meng-Burany 2010).

Aside from imaging, FIB-SEM can also be used to transfer and fix the sample into a particular sample holder for further characterizations, e.g. TEM for higher spatial resolution imaging. This step usually requires the micromanipulator as the “hand” and the GIS as the “glue” in the form of injecting needle (Figure 1.3a) using either Pt, W, or C as a deposition material. In case of Pt (used for the entire works in this dissertation), the deposition is produced via ion-assisted CVD of trimethyl-methylcyclopentadienyl-platinum ($C_9H_{16}Pt$) (Telari, Rogers et al. 2002, Winter and Mulders 2007) and is done at the eucentric point and usually tilted at 52°. After fixing the sample via GIS on the tip of micromanipulator and placing the sample into the desired holder, the micromanipulator can be separated from the sample by simply cutting a small part of the tip with the ion beam.

1.1.2 Focused ion beam slice and view (FIB-SV)

An extension to FIB-SEM technique is focused ion beam slice and view (FIB-SV), also known as FIB tomography or FIB serial section or 3D-FIB, to generate 3D images eventually. Basically, FIB-SV is an alternating process of imaging and sectioning, where the sample is placed at the eucentric height and tilted at 52°, electron beam is used for cross-section imaging on the x-y plane, and ion beam is used for a sequential cross-section cutting of thin (around 10 nm) layers of the sample. After each layer cutting and subsequent image acquisition, the imaging plane gradually moves in z-direction. Prior to this, a cubic sample with wide trenches (Figure 1.4) appropriate sizes to the field of view of SEM detector, has to be prepared using FIB milling under the same instrument. To protect the cube surface during FIB-SV, a Pt layer with thickness around 1 µm is then deposited on the top of the sample (y-direction) via GIS. FIB-SV usually takes a whole day or even longer depending on the number of acquired 2D images, but the modern instruments have already adopted an automated serial sectioning with integrated drift and dynamic focus correction (Holzer and Cantoni 2012, Cantoni and Holzer 2014), so ones can therefore leave it running in autopilot mode. Afterwards, the resulting 2D image stacks undergo data processing steps, including stack alignment and registration, correction of image defects, segmentation of individual objects, visualization of segmented objects, and quantitative analysis (particle/pore size distribution, surface area, triple phase boundary length, feature counting, etc) depending on the users.

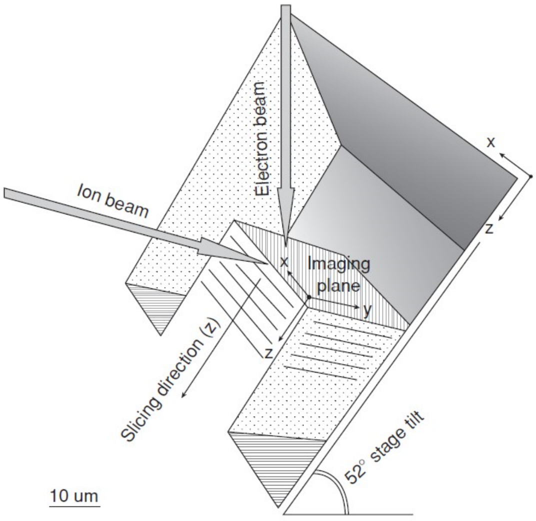

Figure 1.4: Illustration of the optimized sample geometry for FIB-SV using dual beam microscope. Adapted with permission from Ref (Holzer and Cantoni 2012).

1.1.3 Transmission electron microscopy (TEM)

Transmission electron microscopy (TEM) is different than FIB-SEM because it captures transmitted electrons passing through the sample, which makes this technique able to attain higher spatial resolutions more than any other imaging methods. For that reason, the instrument consists of more lenses than FIB-SEM, e.g. condenser, objective, intermediate, and projector lenses, to help in focusing the beam onto the sample as shown in Figure 1.5. Similar to an optical microscope, a direct image can be projected on the viewing screen or captured by a camera sensor. Such an image actually originates from either unscattered for bright-field images or scattered electrons for dark-field images depending on the interaction between electron and sample (Egerton 2005). A special diffraction mode can be made using a selected area aperture by changing the location of intermediate lens (Fultz and Howe 2012), so that a diffraction pattern can be observed on the viewing screen as shown in Figure 1.5-right. Due to the transmission nature and limited penetration depth of electron, TEM has a limitation on the sample thickness with a maximum of 100 nm. In addition, the beam can also be made highly focused to scan over the sample, which is usually called scanning TEM (STEM) mode. In this mode, the image is produced by raster-scanning the sample and capturing the transmitted electrons at each point, where the contrast greatly depends on the atomic number (Z) and the higher the Z, the brighter the appearance. This mode is therefore more utile for characterizing supported catalytic or functional materials (Fultz and Howe 2012). Energy Dispersive X-ray Spectroscopy (EDX) is another integrated technique to measure elemental/chemical composition and usually exists in the form of a detector. When an incoming beam interact with a sample, an inelastic scattering occurs on the atomic scale of the sample, where an inner shell electron is excited creating an electron hole. An outer shell electron with higher energy then fills the hole and then release X-ray as a compensation. Such X-ray energy, characteristic of the energy difference between two shells and of the atomic structure of the emitting element, is then measured by the detector.

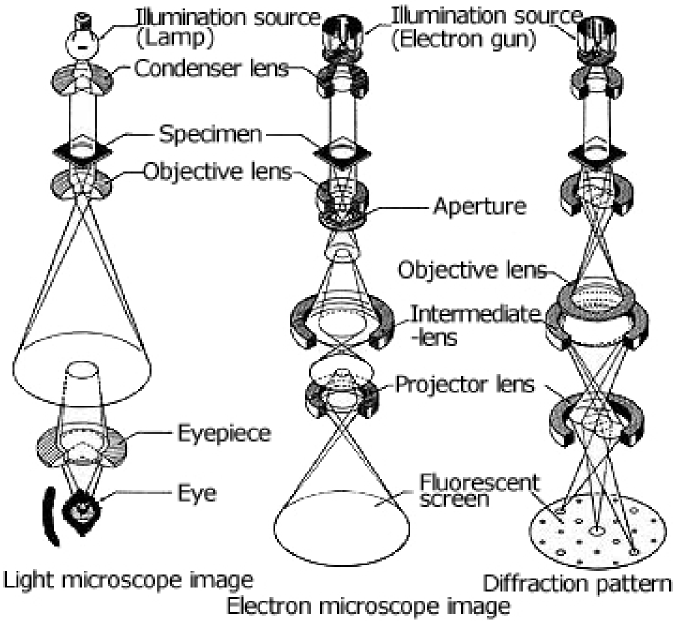

Figure 1.5: Illustration of beam paths and optical configurations between (left) optical microscope and TEM under (middle) imaging mode and (right) diffraction mode. Adapted with permission from Ref (JEOL 2019).

1.1.4 Electron tomography (ET)

An extended TEM method to generate 3D images is electron tomography (ET), also known as TEM tomography or 3D-TEM. The basic principle traces back to the work of Johann Radon (Radon 1986), where a suitable signal in the form of electron scattering from the variations of mass thickness in the sample is used to acquire 2D projections at different tilting angles (from one extreme of tilt to the other) around a particular tilt axis. The tilting process (Figure 1.6) should be made as large a range as possible and the amount of 2D projections should be maximized in order to attain the best spatial resolution (Radermacher 1988), but the resulting electron dose on the sample requires concern, especially for biological samples, so the dose-efficient and automated process has been developed (Ziese, Janssen et al. 2002). After obtaining a series of 2D projections, an alignment procedure is imperative, where each projection needs to be shifted onto a common tilt axis with a spatial and rotational shift as well as some corrections from scan and/or lens distortions. This step, usually carried out by the combined uses of fiducial markers, feature tracking, and sequential cross correlation, should be applied as accurate as possible since it affects the 3D reconstruction quality even with only small misalignments.

The next step is the reconstruction process, where a series of pre-aligned 2D projections are turned into a 3D volume. There are many available methods and already discussed in details in this report (Hayashida and Malac 2016) with each has its own pluses and minuses. However, the simultaneous iterative reconstruction technique (SIRT) was used in this work, where an iterative process (around 10-20 times) compares projections to the original projections and the resulting differences are compensated (Venkatakrishnan, Drummy et al. 2013). Although this method is useful to reconstruct even noisy images, it has a drawback to over-smooth features and introduce artefacts for the tomograms. Then, segmentation, visualization, and quantitative analysis are similar to FIB-SV, which depends on the probed sample and users.

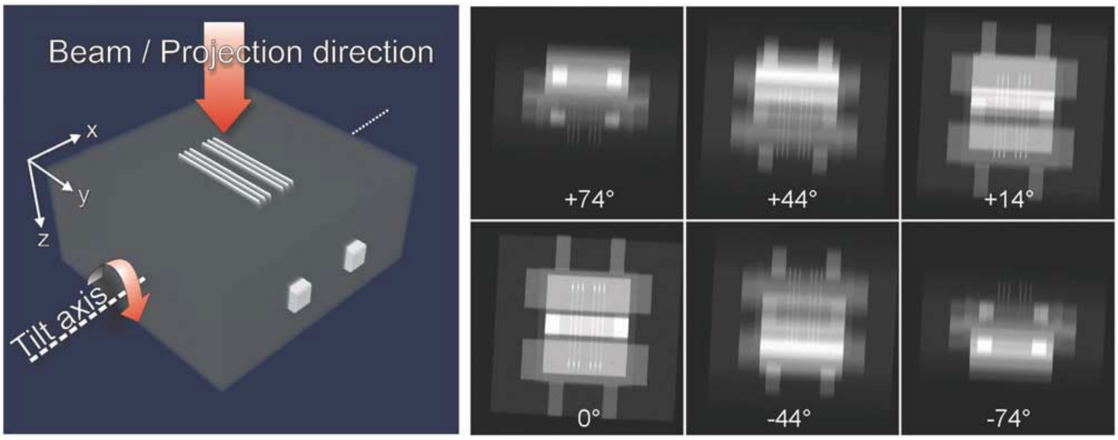

Figure 1.6: Image acquisition process in ET, where images are obtained by a tilt series at a single tilt axis to generate 2D image projections. Adapted with permission from Ref (Weyland and Midgley 2004).

1.2 X-ray imaging techniques

Although X-ray imaging is not as famous as X-ray spectroscopy in catalysis, X-ray imaging studies have been progressively growing in the past two decades (Schroer, Cloetens et al. 2004, Midgley, Ward et al.

2007, Grunwaldt and Schroer 2010, Grunwaldt, Wagner et al. 2013, Weker, Huang et al. 2016, Meirer and Weckhuysen 2018). Despite the lower spatial resolutions of X-ray imaging compared to electron imaging, X-ray imaging has the superiority in more flexible working condition and larger field of view. Although there are actually various types of X-ray imaging (Grunwaldt and Schroer 2010, Grunwaldt, Wagner et al. 2013, Weker, Huang et al. 2016), i.e. radiography, phase-contrast imaging, coherent diffraction imaging, tomography, the following techniques done at the synchrotron radiation facilities are the focused subjects in this dissertation.

1.2.1 X-ray ptychography (XRP)

X-ray ptychography (XRP) was first implemented successfully in the late of 2000s (Rodenburg, Hurst et al. 2007, Thibault, Dierolf et al. 2008), where it is a solution for scanning transmission X-ray microscopy concerning the limited spatial resolution from the fabrication issue of hard X-ray optics, and coherent diffraction imaging, having limitation to isolate objects. The word “ptychography” actually originates from a translated Greek word “to fold”, where the basic principle is to convolute a finite illumination function and a coherent diffraction pattern of an object in a Fourier space. If transformed into a real space, XRP employs a focused coherent X-ray beam to scan over a sample (Figure 1.7) in such a way that there is always an overlapped illumination between successive scans, providing an over-determination of information for the accumulatively scanned area. Since the scattering signal from the sample matters, the direct result captured by a detector is in the form of far-field diffraction pattern. An iterative reconstruction algorithm is then used to solve and retrieve the amplitude and phase of the object; as well as the complex illumination function. Either amplitude or phase information can then be used to calculate an electron density, useful to develop a real image, but the one derived from the phase is usually preferred for its better contrast and higher sensitivity to low atomic number materials. With regard to the specific reconstruction algorithm, there have been plenty already established (Pfeiffer 2018), but the elaborated maximum-likelihood optimization scheme (Thibault and Guizar-Sicairos 2012) was the one used in this work. This method mitigates the limitation of requiring the exact information of the illumination function (probe) by simultaneous solving of both probe and object transmission function. In terms of spatial resolution, XRP has been making a breakthrough that no other X-ray imaging techniques could, which is down to 10 nm for hard X-ray (Vila-Comamala, Diaz et al. 2011, Schropp, Hoppe et al. 2012). This is due to fact that XRP uses a highly coherent flux and it does not require objective lenses, allowing its spatial resolution independent on the X-ray beam spot size.

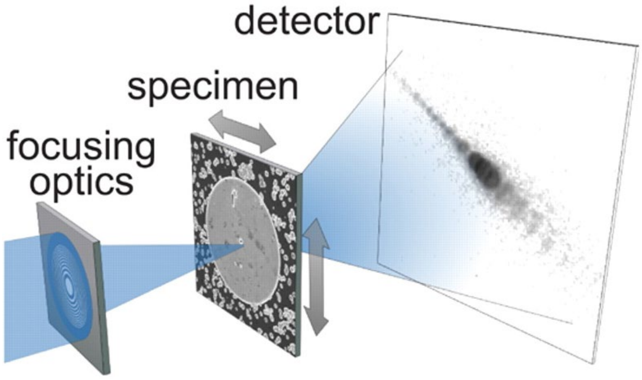

Figure 1.7: Illustration of the path of X-ray beam and experimental configuration of XRP. Adapted with permission from Ref (Thibault, Dierolf et al. 2008).

1.2.2 Ptychographic X-ray computed tomography (PXCT)

As the penetration depth of X-ray is its huge advantage, tomography is then an inherent necessity to integrate the capability of non-destructive 3D imaging into XRP, so ptychographic X-ray computed tomography (PXCT, also known as ptychographic CT or tomographic XRP) was later developed and successfully implemented for the first time in 2010 (Dierolf, Menzel et al. 2010). Therefore, PXCT is actually an extension of XRP, mixed with computed tomography, along with an advantageous capability in quantitative 3D mapping of refractive index at a similar resolution as in XRP. The working principle is basically the same with XRP, but it additionally involves a rotation such that 2D projections at different perspectives can be obtained as shown in Figure 1.8. The general data analysis procedures includes ptychographic reconstruction of phase and amplitude for each 2D projection at various angles, phase-unwrapping and/or phase-ramp removal, alignment and registration of projections at different angles from mechanical drifts, tomographic reconstruction of phase and amplitude (via filtered back projection or maximum likelihood expectation maximization in this work depending on the beamlines), and the similar steps as in FIB-SV or ET, i.e. segmentation, visualization, then quantitative analysis.

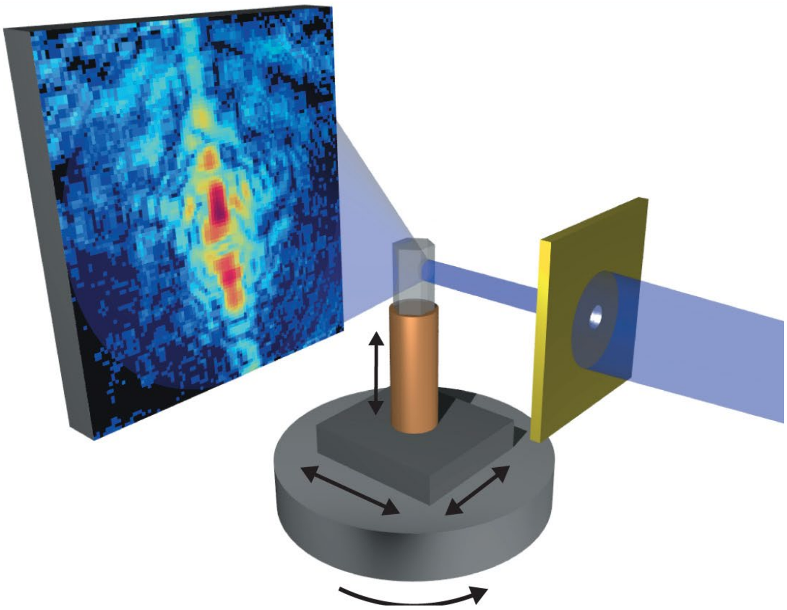

Figure 1.8: Illustration of the X-ray beam path and experimental configuration of PXCT. Adapted with permission from Ref (Dierolf, Menzel et al. 2010).

1.2.3 X-ray fluorescence microscopy (XRF)

Basically, X-ray fluorescence microscopy (XRF) uses a focused X-ray beam to scan across the sample in a raster pattern to produce spatially-resolved elemental/chemical map, based on the intensities of secondarily emitted (or fluorescence) X-rays from the photoelectric effect. Such fluorescence X-rays, unique for each element, are quantified by a detector, which can be positioned perpendicular to the incoming X-ray or in a backscatter geometry. In this work, XRF from a nanoprobe beamline at a synchrotron facility was conducted along with *in situ* XRP as a complementary measurement.

1.3 Complementary X-ray (XRM) & electron microscopy (EM)

As a single imaging tool is not able to generate information covering all the length scales, complementary techniques are thus required although each has its own disadvantages. While the macro-scale (>1µm) technique has been well-established under optical microscopy and the nano-scale (< 10 nm) has been exclusively covered by TEM, the meso-scale (10 nm – 1 µm) has been an overlapped area between various microscopic methods, dominated mostly by XRM (Grunwaldt and Schroer 2010, Grunwaldt, Wagner et al. 2013, Meirer and Weckhuysen 2018). The reasons behind such classification are due to the source characteristics and corresponding optics, where the wavelength of visible light inherently limits the spatial resolution in optical microscopy, the focusing optics is the bottleneck for X-ray despite its high penetration depth, and electron has a limitation in its penetration depth although it is easier to focus. Therefore, combining X-ray and electron microscopy with their compensating advantages is important in hierarchical imaging studies as both techniques are quantitative with various contrast signals under absorption, diffraction, fluorescence, and scattering mode (Thomas and Hernandez-Garrido 2009, Grunwaldt and Schroer 2010).

TEM has been famous to extract nano-scale structural information of nanoparticles either on the surface or at the interface, but the analysis is often hindered by problems in lens aberrations and irregular contrast due to varying sample thickness (Marks 1983, Marks and Smith 1983, Malm and O'Keefe 1997, Tsen, Crozier et al. 2003). It was then overcome by the development of aberration-corrected TEM, whose objective lens have been technically adjusted via hardware/software, bringing in clearer images with higher spatial resolutions (Kawasaki, Takai et al. 2001, Freitag, Kujawa et al. 2005, Gontard, Chang et al. 2007, Kirkland, Chang et al. 2008, Su, Jacob et al. 2008, Tanaka 2008). However, a direct acquisition of elemental analysis via an integrated spectroscopy detector on the surface of nanoparticles under high resolution mode is not possible so far, so an alternative simulation study has been adopted to back it up (Yoshida, Kuwauchi et al. 2012). A trick was developed under scanning TEM (STEM) mode to be able to perform such chemical analysis as well as the morphology observation with a sub-nm spatial resolution (Erni, Rossell et al. 2009, Krivanek, Chisholm et al. 2010). This way, a focused electron beam is scanned across the sample, producing a high-angle annular dark-field intensity for structural information based on the atomic number, and an electron-dispersive X-ray spectrum for mapping the corresponding elements. Despite having been often used for the purpose of higher-contrast imaging(Borisevich, Wang et al. 2007, Herzing, Kiely et al. 2008, Pyrz, Blom et al. 2008, Zhou, Ross-Medgaarden et al. 2009, Zhang, Trunschke et al. 2010), a complementary study of this method has also been carried out to confirm the particle size distribution of supported catalysts from extended X-ray absorption fine structure measurements (Zhang, Zhang et al. 2011).

XRM, on the other hand, has been famous in structural characterizations at the meso scale, which is as important as the nano scale in catalysis, with various established techniques. One common technique is scanning X-ray microscopy, utilizing a nanofocused beam to scan across the sample and an absorption signal to generate images and spectra for X-ray absorption spectroscopy (Schroer, Kuhlmann et al. 2003) along with other signals for additional measurements, such as fluorescence for XRF (Carmona, Cloetens et al. 2008) and scattering for small- (Schroer, Kuhlmann et al. 2006) or wide-angle X-ray scattering study (Bleuet, Welcomme et al. 2008). Spatial resolutions below 100 nm can be achieved using Kirkpatrick-Baez mirrors and refractive optics with spot sizes below 10 nm (Mimura, Handa et al. 2010, Yan, Rose et al. 2011), whereas X-ray mirrors are more suitable for the integration with X-ray absorption spectroscopy due to its achromaticity and focus independence of X-ray energy (Schroer, Kuhlmann et al. 2003). Nevertheless, the spatial resolutions of this technique are still expected to improve, particularly by the advent of fourth generation synchrotron facilities with higher brilliance, e.g. PETRA IV in Hamburg (Schroer, Agapov et al. 2018). Another XRM worth mentioning is coherent X-ray diifraction imaging, making use of the highly coherent part of the beam to produce far-field diffraction patterns and numerically reconstruct them into real images with the help of additional known object variables. This technique was then able to surpass a record of reaching spatial resolutions in single-digit nanometers (Schroer, Boye et al. 2008, Takahashi, Nishino et al. 2009) despite the model objects. A derivative out of this technique, combined with scanning X-ray microscopy, is XRP, where it adopts the similar principle of coherent diffraction imaging, except under scanning mode. Despite having been used to resolve functional materials (Schropp, Boye et al. 2011, Esmaeili, Fløystad et al. 2015, Zhu, Harder et al. 2015, Hémonnot, Reinhardt et al. 2016, Yan, Nazaretski et al. 2016, Van den Brande, Patil et al. 2017, Fam, Sheppard et al. 2019), this method is still new in the field of catalysis, so the prospect as a catalytic structural characterization, especially operando study, is promising. Besides, ptychography has also been applied in scanning electron microscopy to reach spatial resolutions of 2-5 nm (Humphry, Kraus et al. 2012), indicating the potential in breaking the records via XRP. XRP has also been combined with X-ray absorption spectroscopy to the determine the chemical state of selected elements with spatial resolutions of 20-100 nm and the structural results were also compared with SEM images for comparison (Hoppe, Reinhardt et al. 2013, Hirose, Ishiguro et al. 2018).

The above results come from 2D imaging studies, which exhibit only the projections of the real samples in 3D. For X-ray, the capability to obtain 3D volume of real samples has been common at macro-scales via X-ray computed tomography, even hospitals nowadays own the machine to localilze tumors inside human bodies, thanks to the high penetration depth of X-ray. In catalysis, this method has been applied to extract the valuable information regarding particle distribution, morphology, and pore structure of the catalysts, even at the meso-scale (Grunwaldt and Schroer 2010, Grunwaldt, Wagner et al. 2013, Weker, Huang et al. 2016, Meirer and Weckhuysen 2018). As the higher 3D spatial resolutions are the better, especially for the direct use in simulations (Zabihzadeh, Cugnoni et al. 2017, Delattre, Amin et al. 2018, Cuesta, De la Torre et al. 2019, Tan, Kok et al. 2019), a recent method to pursue that goal has been realized via PXCT reaching up to 14 nm (Holler, Guizar-Sicairos et al. 2017). A major challenge and drawback of PXCT is the measurement time, taking its toll from several hours to a day, which can negatively affect the sensitive probed samples. Decreasing the field of view, number of projections, and scanning step size are common to save the time at the expense of lowering down the spatial resolution. The prospect of PXCT in achieving higher spatial resolution and shorter measurement time is promising with the upcoming fourth generation synchrotron facilities. Furthermore, a modified PXCT, called as resonant phase imaging, has also been successfully conducted with selected materials to chemically localize different elements in 3D (Donnelly, Guizar-Sicairos et al. 2015, Ihli, Diaz et al. 2018).

For electron, although it has been overshadowed by X-ray in terms of 3D imaging, 3D imaging studies have also been carried out via ET (Miao, Ercius et al. 2016) or FIB-SV (Cantoni and Holzer 2014) with a special focus on ET owing to the spectacular 3D spatial resolutions at atomic-scale (Bar Sadan, Houben et al. 2008, Van Aert, Batenburg et al. 2011), e.g. resolving individual atoms of an icosahedral Au nanoparticle along with its 3D grains (Scott, Chen et al. 2012) or even resolving 3769 individual atoms of W needle tip with 19-pm resolution (Xu, Chen et al. 2015). Aside from the excellence in spatial resolutions, ET is also able to make use of spectroscopic signals for simultaneous elemental analysis using EDX detector (Yeoh, Rossouw et al. 2015, Slater, Janssen et al. 2016) or chemical state analysis using EELS detector (Yedra, Eljarrat et al. 2014, Torruella, Arenal et al. 2016), despite the worse resulting reconstruction compared to the transmission imaging results. Moreover, ET has also been utilized to observe material defects, e.g. dislocations, under dark-field mode so as to enhance the contrast (Barnard, Sharp et al. 2006, Barnard, Sharp et al.

2006, Tanaka, Higashida et al. 2008). One challenge and drawback in ET, compared to PXCT, is the typical missing wedge problem due to the inherent limitation of short penetration depth of electron, hindering it to perform full rotation of 180° for an optimized 3D reconstruction inducing the presence of elongation artifacts. However, methods to overcome such problem have been reported by either improving the reconstruction algorithms (Saghi, Holland et al. 2011, Goris, Van den Broek et al. 2012) or modifying the sample holder into a customized tip, to where the sample is deposited (Padgett, Hovden et al. 2017, Przybilla, Zubiri et al. 2018). Another challenge of ET is improvement in tilt series acquisition times, usually taking tens of minutes for one tomogram and making it impossible to observe dynamic changes in 3D. Recently, a semi-automatic Fast Step-by-Step ET was found to be applicable for *operando* ET, where the kinetics could sufficiently be slowed down via a fine pressure and temperature control (Roiban, Li et al. 2018, Koneti, Roiban et al. 2019). Although the total acquisition time of 2 min with total angles of 140° could be obtained, it is unfortunately still not ideal for the general *operando* ET with more rapid dynamic processes. Other possible solutions include the utilization of higher-brightness electron sources, improved specimen stages and detectors (Van Aert, Batenburg et al. 2011). Last, it would be optimum if ET is complemented by PXCT to hierarchically analyse materials at various length scales from pm to µm since one compensates the other's disadvantages in terms of "field of view vs spatial resolution".

1.4 *In situ* EM and XRM

As *in situ* studies are able to reveal the dynamic nature of materials under reaction conditions so as to optimize their activities/performance for their applications, the challenges involved also increase, especially for EM, where the mean free path of electrons are short in gases and liquids. So far, the widespread use of *in situ* TEM has been renowned, proven by many available publications (Ramachandramoorthy, Bernal et al. 2015, Song and Xie 2018, Fan, Zhang et al. 2019). The initial studies were carried out in a way, so-called "*quasi in situ*", that the samples were transferred back-and-forth from the reactor to TEM instrument with an intermediate sealed container at room temperature (Kooyman, Buglass et al. 2002). Although it brought new perspective, the results were debatable whether they represented the results done under complete in situ condition, because the atmosphere change inbetween the sample transfer possibly modified the morphology from its working state, e.g. catalysts are in an active phase only under their working conditions in the methane partial oxidation (Grunwaldt, Basini et al. 2001, Grunwaldt, Hannemann et al. 2006). So far, there are two possible ways of performing in situ TEM, one is by utilizing a dedicated *in situ* sample holder (Figure 1.9a-c), and the other is by integrating a special part into an existing TEM, turning it into an environmental TEM (ETEM) as shown in Figure 1.9d. Although complete *in situ* TEM for high-pressure gas and liquid studies are nowadays possible with the former method based on micro-electrical-mechanical systems technology (Creemer, Helveg et al. 2008, Yokosawa, Alan et al. 2012, Dembélé, Bahri et al. 2018, He, Wang et al. 2019), challenges in hardware modification are still difficult, particularly in sample geometry and acquisition of reliable EDX spectra. On the other hand, the latter method comes with a bigger internal volume cell, integrated directly in the TEM column and allow the utilization of general TEM sample holders (Hansen, Wagner et al. 2010, Wagner, Cavalca et al. 2012). However, this setup has a limitation in working pressures only up to several mbar, while the other method can reach a pressure up to 4.5 bar and accommodate even liquid samples with a particular holder (Figure 1.9a-c).

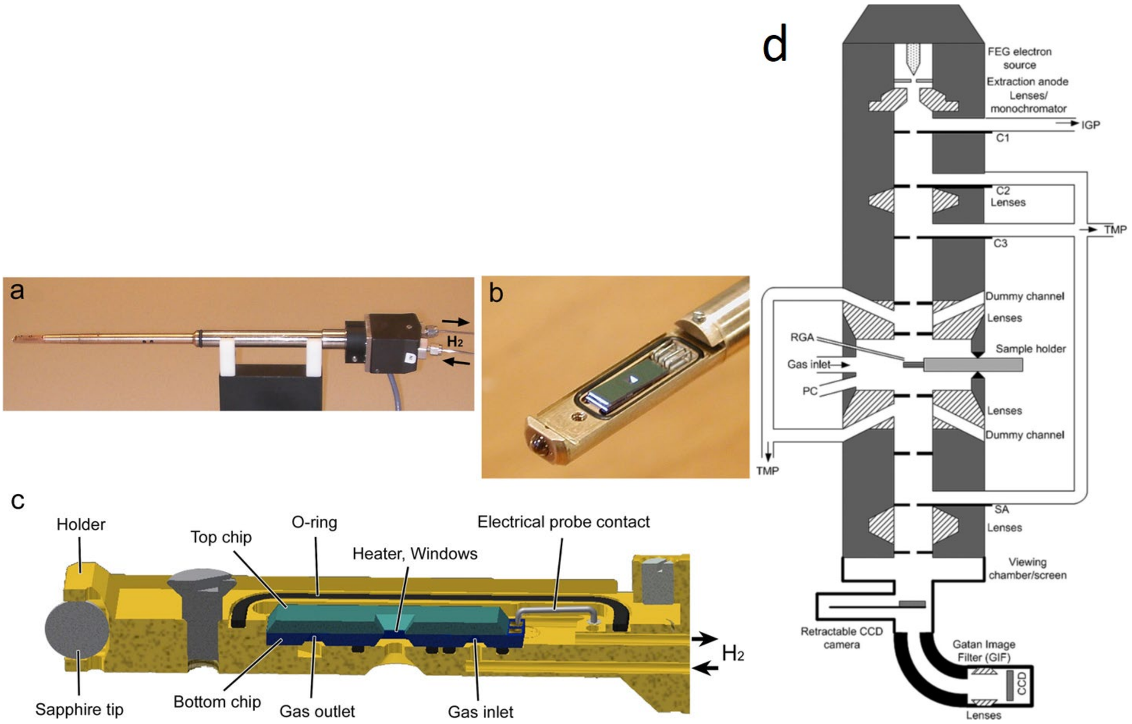

Figure 1.9: *In situ* TEM MEMS-based setup: a) Sample holder. (b) Nanoreactor inserted in the sample holder. The lid of the holder is removed for a better view. (c) Schematic diagram of the nanoreactor inserted in the sample holder (Yokosawa, Alan et al. 2012). ETEM setup: d) Schematic diagram of a differentially-pumped TEM column. Adapted with permission from Ref (Hansen, Wagner et al. 2010).

The first type of *in situ* TEM MEMS-based setup has been used in various applications depending on the sample holders. In one case, it has been implemented to visualize the growth dynamics of multi-walled carbon nanotubes from Fe-based catalyst in a gas mixture of H_2, C_2H_4, and He (Huang, Farra et al. 2019). Using a specific sample holder for *in situ* TEM gas and heating system under high resolution mode, they were able to unravel the influence of gas pressure and temperature on the growth of carbon nanotubes, so the active phase of the catalyst and the rich structural dynamics of the catalysts during the growth of carbon nanotubes were revealed in real-time observations. Another study made use of a particular sample holder for *in situ* TEM liquid system to continuously record the entire self-assembly process of a liquid membrane, made from soap-like nanodroplets submerged in water (Ianiro, Wu et al. 2019). Previously, the users had to initially freeze the membrane to be able to have TEM images, but a live-imaging is now possible thanks to the well-controlled liquid environment from this setup. Another application is by applying in electric field investigations using a unique sample holder for *in situ* TEM heating and biased system, where the presence of domain-like nanoregions was unexpectedly found in high-temperature flexoelectric nanomaterials by applying electric fields up to ±22 kV/mm at 800 °C and the structural dynamics under high-resolution mode were recorded (Molina-Luna, Wang et al. 2018). From those examples, this setup is promising for future applications in many untouched subjects, such as geology or oceanography.

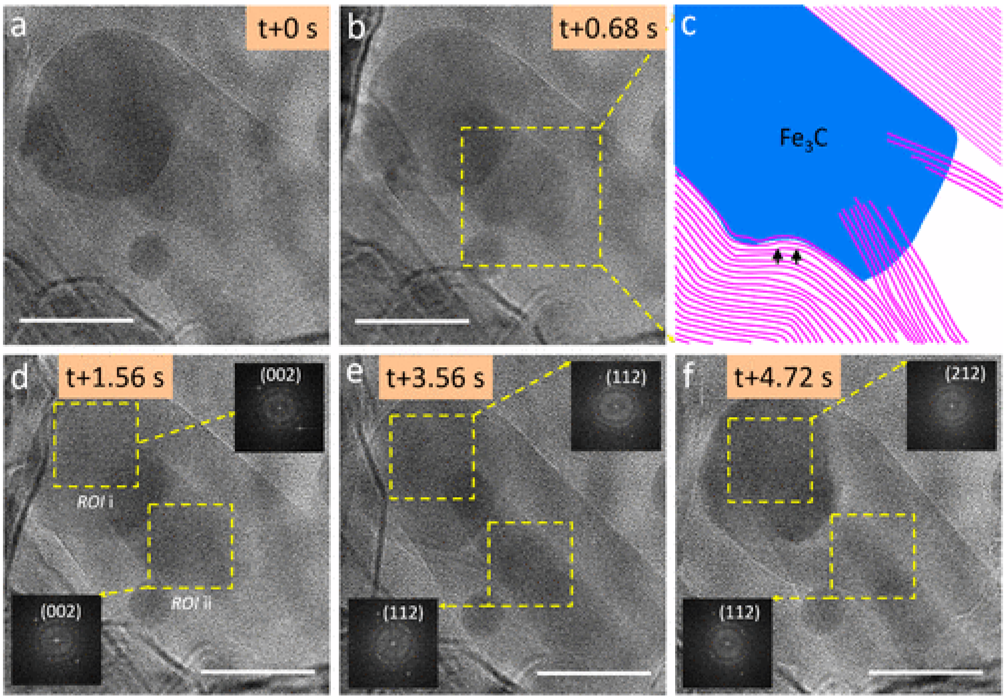

Figure 1.10: (a,b,d–f) *In situ* atomic-scale TEM observation of the catalyst splitting during the course of CNT growth; insets of (d–f) show FFTs from the indicated areas. (c) Schematic drawing of an elongated particle bonded with CNT layers. Scale bar is 20 nm. Adapted with permission from Ref (Huang, Farra et al. 2019).

The second type of ETEM setup, on the other hand, has been mostly exploited in catalysis or functional material science. One case is in studying Au nanoparticles on BN support for online sintering process at 130 Pa under H_2 gas at 400 °C (Hansen, Wagner et al. 2010). The study concluded that the sintering was based on two mechanisms: (i) particle migration over the support and coalescence when nearby to each other, (ii) Ostwald ripening due to diffusion of atoms or molecules triggering mass transport from smaller to bigger particles. Another study involved the combination of ETEM, X-ray photoelectron spectroscopy, and DFT calculations to investigate the structural dynamics of industrial $Cu/ZnO/Al_2O_3$ for methanol synthesis (Behrens, Studt et al. 2012). They were able to find out that the active site of the catalyst comprises Cu steps surrounded by Zn atoms with well-defined bulk defects and surface species. A nucleation and growth study of single-walled carbon nanotube was also carried out via ETEM under 8E-3 mbar at 615 °C (Hofmann, Sharma et al. 2007). The initial structure was a carbon cap with an apex shape sitting on top of Ni catalyst. The carbon was then lifed off from Ni, which was self-restructured. The carbon later made a cylindrical shape, constraining Ni particle until it reached to the bottom. Furthermore, an anode material for solid oxide fuel cells has also been studied under ETEM for “live” redox reaction (Jeangros, Faes et al. 2010). The authors initially oxidized the material during fuel cell operation and found out that oxidation occurred from the high fuel consumption or air leakage, which are detrimental to the morphology leading to a device failure. Afterwards, they reduced the material and began the *in situ* observation under 130 Pa of H_2 at temperatures up to 500 °C, so as to observe the pore formation. Later, the material was reoxidized under 320 Pa of H_2 at the same temperature treatment and found that the pores were refilled with polycrystalline oxidized material, so they concluded that the volume-change-induced stress resulted in the device failure during operation. An interesting and unique exploitation of ETEM was the implementation of *in situ* ultraviolet illumination with a customized holder (Cavalca, Laursen et al. 2012), which aimed to stimulate photocatalytic water oxidation. Although there was not any mass spectrometric data for the conversion of water vapor into oxygen, the authors managed to indirectly proved that the water oxidation process occurred with the reduction of Pt precursors into metallic Pt by ETEM without the electron beam and only *in situ* UV light. Years later, another study also combined ETEM with *in situ* UV light using TiO_2 particles immersed in water (Lu, Yin et al. 2018) as shown in Figure 1.11. Their discovery answered the very reason of why TiO_2 alone is not photoactive for hydrogen evolution reaction, which is due to the generation of hydrogenated TiO_2 surface shell as a proof that the photocatalytic reactions could not occur without additional co-catalysts.

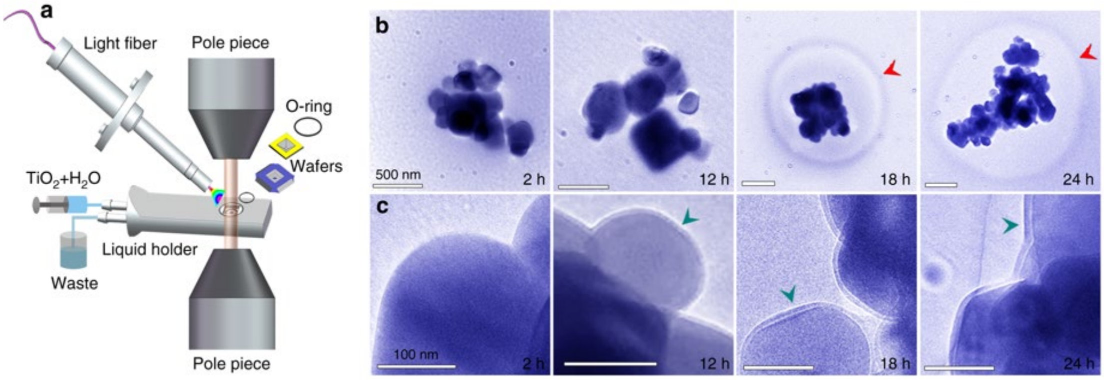

Figure 1.11: ETEM analyses of the growth of surface shell on TiO_2 particles and the formation of H_2 nanobubble after UV light illumination. (a) A liquid ETEM setup with an *in situ* illumination and a liquid sample injection containing water-immersed TiO_2 particles. (b) TEM images of TiO_2 particles during photocatalysis at different times. Red arrows indicate the gas bubbles surrounding TiO_2 particles. (c) Zoomed-in images in (b). Green arrows indicate the surface shells growing and covering TiO_2 particles with times. Adapted with permission from Ref (Lu, Yin et al. 2018).

Regardless of the setup, all *in situ* TEM experiments using gas and heating system always require optimizations for the specimen temperature, gas composition and pressure for every experiment, along with the microscope software parameters. Besides, the concern of reducing and heating effect as well as damage by electron beam, along with the interaction between the incoming electron beam, gas, and secondary electron emitted from the sample, should be taken into consideration and proper care. Moreover, the spatial resolution and image stability are also affected when both gas and heating system run to some extents, which should be due to the thermal drift and scattering effect from the interaction between electron and gas molecules (Hansen, Wagner et al. 2010, Yaguchi, Suzuki et al. 2011, Jinschek and Helveg 2012, Wagner, Cavalca et al. 2012). However, such problems can be mitigated by using the *in situ* XRM, especially with hard X-ray, which is stable and flexible in working pressures and temperatures. At the beginning, many *in situ* XRM experiments were dominated by soft X-ray due to its predevelopment of focusing optics. The first *in situ* study was performed using scanning transmission X-ray microscopy (STXM), combined with X-ray absorption spectroscopy, with a customized cell, whose design was adopted from the *in situ* TEM MEMS-based setup (Creemer, Helveg et al. 2008), so as to investigate a catalyst for Fischer-Tropsch synthesis (de Smit, Swart et al. 2008). The experiment took place at the STXM beamline 11-0.2. of the Advanced Light Source and a spatial resolution of 15 nm was obtained. Figure 1.12 exhibits the contour plots of Fe valence and its metal/carbide/oxide condition with the spatial variations of 35 nm. Moreover, the X-ray absorption spectra at Fe L_2 and L_3 edges verify that the generated Fe_xC_y originated from the α-Fe after reduction. Nevertheless, this study, along with other *in situ* STXM studies for zeolites (Aramburo, de Smit et al. 2012, Aramburo, Wirick et al. 2012) or battery matterials (Meirer, Cabana et al. 2011, Nelson, Misra et al. 2012), generally point out the importance of complementary XRM to TEM for monitoring materials at the meso-scale.

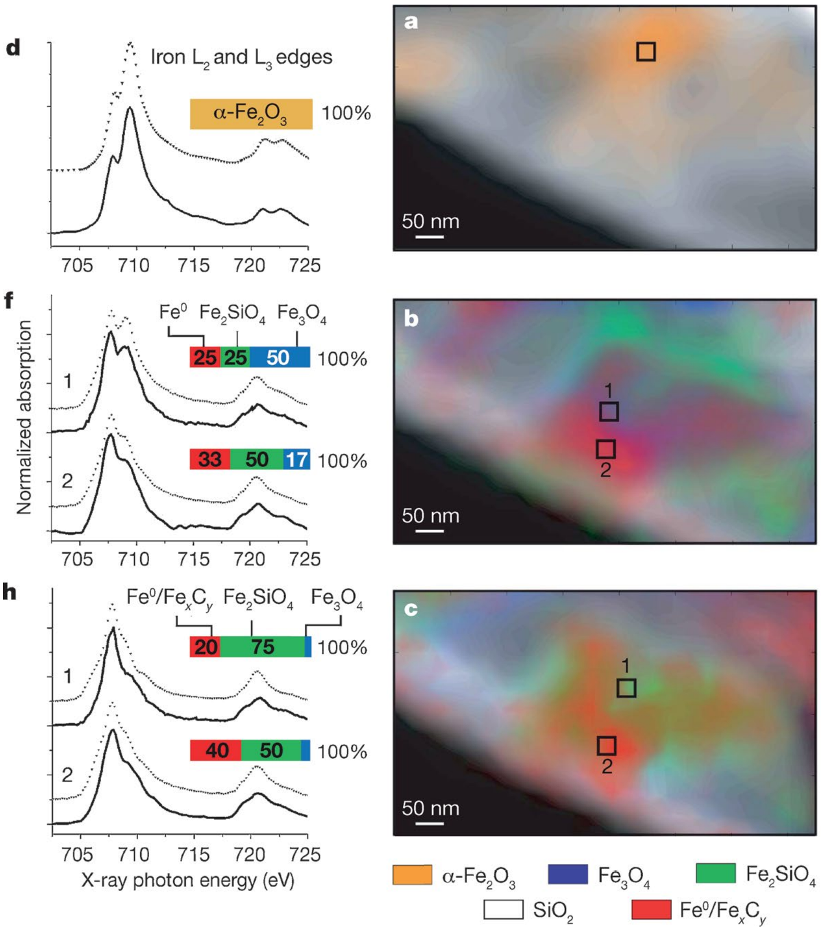

Figure 1.12: Scanning transmission X-ray microscopy contours of Fischer–Tropsch catalysts (a) at room temperature, (b) after reduction in H_2 at 350 °C, and (c) after CO hydrogenation at 250 °C. X-ray absorption near-edge spectroscopy spectra at (d, f, h) Fe L_2 and L_3 edges. Adapted with permission from Ref (de Smit, Swart et al. 2008).

The experiments using soft X-ray have unfortunately also brought some drawbacks, including a maximum penetration depth of 100 µm, limited amount of the probed material, and complicated cell design due to the required limited distance between the sample and aperture after the Fresnel zone plate. However, such problems can be overcome by using hard X-ray, mitigating the challenges in the development of *in situ* cells, although the spatial resolutions are still behind the soft X-ray due to the lacking development of focusing optics and insufficient brilliance of the source. Among *in situ* hard X-ray techniques, XRP has been the leading trend in terms of high-resolution imaging and is expected to be able to reduce the spatial resolution limit down to the sizes of catalytic nanoparticles. *In situ* XRP has been employed for the first time to resolve absorbents for CO_2 capture, using a customized bulk reactor with a heating system up to 620 °C at atmospheric pressure (Høydalsvik, Bø Fløystad et al. 2014). Although the spatial resolution of around 200 nm was achieved at cSAXS beamline of Swiss Light Source, another *in situ* experiment at the same beamline was carried out two years later to resolve porous metals under particular environments, resulting in a significantly higher resolution of 20 nm (Baier, Wittstock et al. 2016). The study utilized a dedicated *in situ* cell, adopted from the MEMS-based *in situ* TEM cell (Creemer, Helveg et al. 2008), with better technical improvement in terms of gas-tight condition and heating capability. Such impressive leap in the spatial resolution demonstrates the potential of (hard) XRP for *in situ* analyses if functional nano-materials and catalysts, particularly for monitoring the structural dynamics during reactions, e.g. particle migration, Ostwald ripening, fragmentation, or coalescence. Amongst other X-ray imaging methods, XRP is at the forefront of attaining the highest spatial resolutions at the expense of longer measurement time. Although the spatial resolution of this method has not yet approached the TEM capability, it is projected to be increasingly high along with faster measurement time, when the higher coherence fourth generation synchrotron radiation are available.

In the case of operando EM and XRM, Mass Spectrometry (MS) is used to identify a chemically unknown substance based on the mass from the gas products. The mechanism behind a mass spectrometer is as follow: prior to the actual mass analysis, a gaseous sample is initially ionized. The ions are then deflected in a mass analyser (time of flight or quadrupole) with an electrical field, based on the ratios of mass to charge (m/z). In a quadrupole MS (used in this work), those ions are previously accelerated and the electrodes, applied with a high frequency alternating current, are on the same potential. For mass separation, stable trajectories are obtained for various m/z ratios by adjusting the frequency. Afterwards, a Faraday or electron multiplier detector is used to measure the number of unblocked ions. In this work, an online MS was employed to confirm the gas-leaking proof of an *in situ* cell by monitoring the stability of a specific gas flow rate.

1.5 Sample preparation for electron and/or X-ray microscopy

Prior to electron or X-ray-based imaging experiments, the sample preparation step is crucial in order to obtain optimal imaging results. Depending on the sample condition, measurement mode and light source, there have been many established ways ranging from simple to complicated ones (Humphreys, Beanland et al. 2001). Generally, scanning electron microscopy is relatively easy since a bulk material can be directly measured after a simple mounting, cutting, and/or polishing procedure. The mounting step on a stub is mandatory to properly fix the sample on the stage and it can simply be done using tapes (e.g. conductive carbon tape) or clips. If sample is in a liquid or aqueous form, the process should include drying to evaporate the solvent before the measurement. For solid, a further cutting process by cutting saw (e.g. diamond saw for higher precision) is sometimes necessary when the size is too large or a cross-sectional view of the sample is needed. Furthermore, polishing is another optional procedure to carefully reveal the internal structure of a bulk material when cutting is impossible to apply and/or to remove the contamination layer out of the sample (Volkert and Minor 2007). It can be performed mechanically by a rotating disc covered with a soft abrasive paper/cloth and a running lubricant (e.g. water) until the surface is mirror-like. Electropolishing is also another alternative utilizing an external electrical current to run through the sample surface as the anode in an electrolytic cell, while chemical polishing is another option via immersion in or swabbing with some proper chemical solutions (Meng-Burany 2010).

On the other hand, TEM sample preparation is more challenging since it optimally requires a sample thickness of ≤100 nm owing to its transmission mode as well as the limited penetration depth of electron as the light source. Basically, the initial preparation steps involve the same steps as for SEM, but it requires an extended thinning procedure to achieve sub-micron thicknesses. However, if the sample is homogeneous and the measurement is not site-specific, a simple drop-casting process of dispersed solution containing samples (powder-solid or liquid or aqueous) is possible. The final thinning procedure for the purpose of electron transparency commonly involves an ion milling (Méndez-Vilas and Díaz 2010). The ion milling process (e.g. by Ar ions) exploits ions to gradually sputter the surface layers of the sample at specifically low angles aiming to minimize damage on the sample (Chew and Cullis 1987). A plasma, formed by an electrical discharge, contains the ions, which are accelerated by a pair of optically aligned grids becoming highly collimated beams. The beams are then focused on a tilted working plate, which contains the sample and rotates during milling, and a neutralizing filament is installed to prevent accumulated positive charges on the sample. The rotational direction is perpendicular to the plane of assembly so as to produce a uniform waste removal surrounding the area of interest. This operation is commonly utilized in a cross-sectional sample preparation as shown in Figure 1.13. It typically starts with mixing the powder sample with epoxy resin and hardener with a specific ratio. The mixture is then sandwiched between two silicon wafers and cured at certain temperatures for several hours. Next, the stack is polished using increasing-grit sandpapers until the thickness reaches 20 µm and a flat mirror-like surface can be observed via optical microscope. It is later subsequently glued with a resin on a grid as the sample holder and beam-milled by an ion polishing system at a certain angle until a hole-like area is formed with a thickness ≤100 nm.

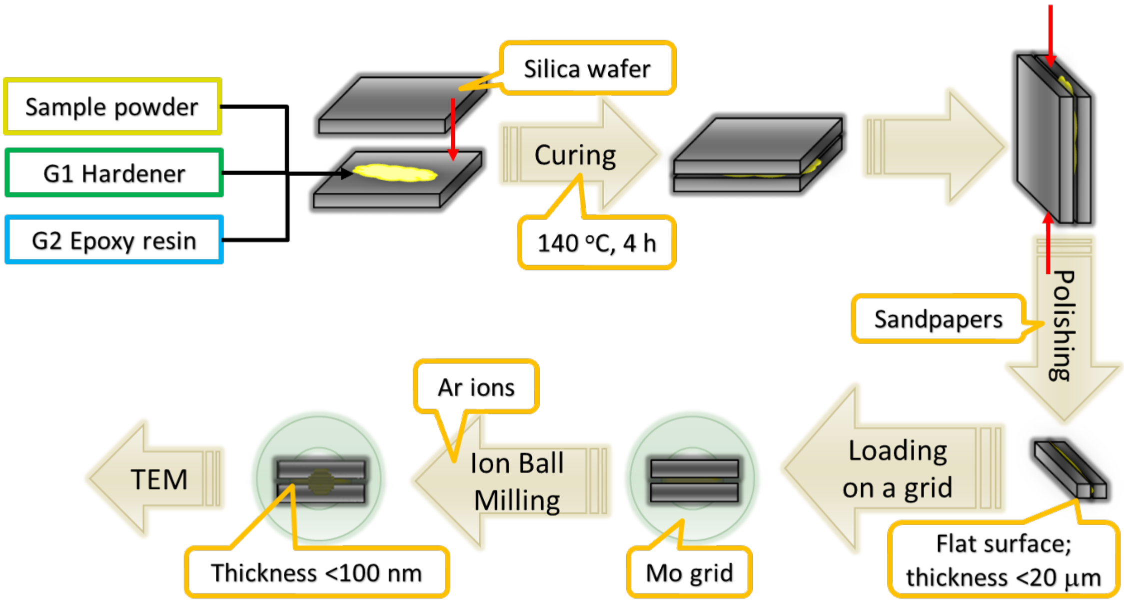

Figure 1.13: Scheme of sample preparation for cross section TEM observation.

While the aforesaid ion miller is actually a single-beam FIB, a more recent development of dual-beam FIB (later on regarded as FIB) has nowadays taken over (Mayer, Giannuzzi et al. 2007, Li 2012). The main advantages are the high precision (nm scales) in selecting the area of interest for milling, relatively faster milling, and independence of the nature of the probed material, covering metals, ceramics, composites, soft matters (polymers, biomaterials, or even frozed liquids). However, the concern of severe damage from ion implantation during milling still poses a threat until now although it is not as extensive as the previous ion milling/single-beam method. The initial method of FIB was similar to the ion miller, where it needed a mechanical polishing down to 50 µm and subsequently a cutting with FIB into an H-bar of the remaining material (Kirk, Williams et al. 1989). This technique was later fine-tuned using a tripod polisher during intial thinning, which reduces milling time significantly (Basile 1992). Another technique, so-called lift-out process (Yaguchi, Kamino et al. 1999, Giannuzzi; and Stevie 2005), was developed for more efficient procedure, where the initial need of mechanical polishing was not necessary. Another advantage is that the specimen can be shaped in more varying geometries with low-energy beams for further thinning and cutting (Giannuzzi, Geurts et al. 2005). Specifically, the portion of interest was firstly cut into a wedge shape or parallel-sided piece and then transferred onto a lift-out grid by the micromanipulator. The manipulation is carried out by attaching the manipulator probe to the sample via FIB deposition of a metal (e.g. Pt) layer. On the grid, the thinning process of the wedge occurred until it is electron-transparent as in the H-bar technique. This technique was later modified and popularized (Mayer, Giannuzzi et al. 2007), involving an extra step (between the transfer and milling) of rotating the grid containing the sample by 90° so that a plan-view can be obtained from a specific location as shown in Figure 1.14.

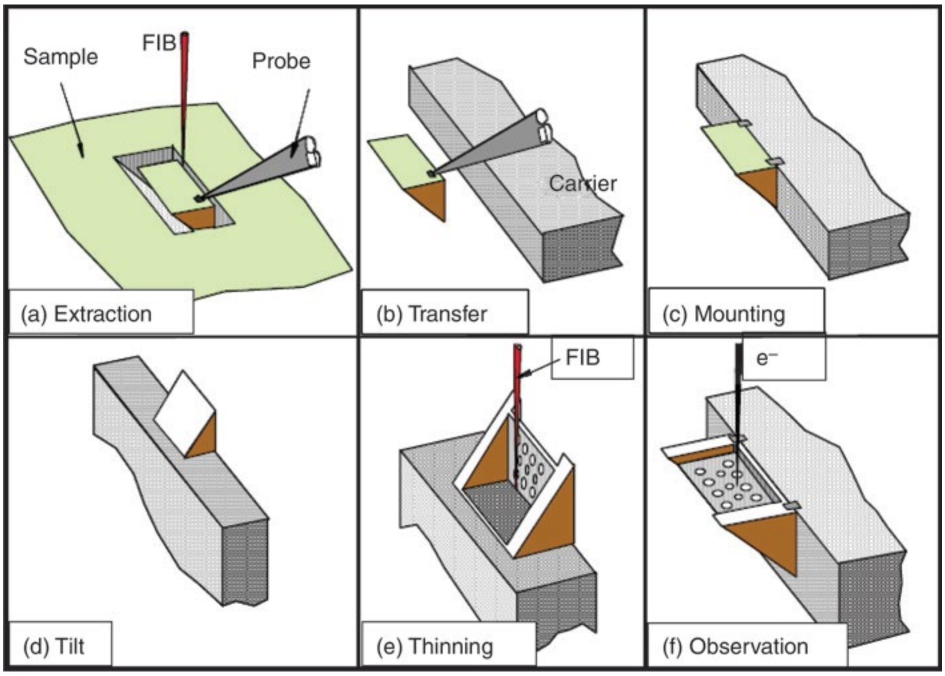

Figure 1.14: Method to prepare a plan-view specimen from a specific site based on the microsampling technique. Adapted with permission from Ref (Mayer, Giannuzzi et al. 2007).

As for X-ray microscopy, the difficulty of sample preparation lies between the SEM and TEM. Owing to the higher penetration depth of X-ray, even up to sub mm for hard X-ray, the requirement of sample thickness is more lenient. The common procedure so far, especially for tomography, has employed FIB (Dierolf, Menzel et al. 2010, Holler, Diaz et al. 2014, da Silva, Mader et al. 2015, Baier, Damsgaard et al. 2016, Baier, Wittstock et al. 2016, Baier, Damsgaard et al. 2017, Ihli, Jacob et al. 2017, Ihli, Diaz et al. 2018, Odstrcil, Holler et al. 2018, Fam, Sheppard et al. 2019), where the samples are deposited on customized sample holders depending the X-ray microscopy setup, particularly ones at the synchrotron facilities. The similar lift-out technique is usually adopted with the difference in the thinning procedure, which is not as rigorous as in the TEM since the sample is in the bigger scales (µm).

Due to involvement of ion beam as the source, a negative impact on the sample is unavoidable, inducing not only an erosion process via sputtering, but also a formation of damaged layers extending up to several tens of nm (Li 2012). Chemically, it can also alter the crystallinity of semiconductor materials into amorphous (Kamino, Yaguchi et al. 2004, Wang, Kato et al. 2005) or even change the phase of certain metals into intermetallic (Jr., Phaneuf et al. 2002, Spolenak, Sauter et al. 2005). To overcome those problems, the utilization of low-voltage (2-5 kV, Figure 1.15) ion beam must be applied and the exact values depend on the instrument and materials, meaning that trials-and-errors or research of previous works should be performed beforehand. Moreover, such a low-voltage procedure is also useful in removing damaged layers from the normal voltage (30 kV) during thinning process (Huang 2004, Kato 2004). However, the acceleration voltage is sometimes not the only variable to control the strength of ion beam as there are other parameters, such as beam current, beam dwell time, beam overlap, refresh time, which also complicate the problem. Another concern for using FIB is the chemical reaction between ion beam and the sample forming new phases. In the case of Ga ion beam, it can generate low-melting temperature phases, e.g. Cu_3Ga was detected at the base of Cu device after FIB cutting (Jr., Phaneuf et al. 2002). This therefore triggers the necessity to be extremely careful during FIB cutting to minimize any compromise on the sample prior to further characterizations.

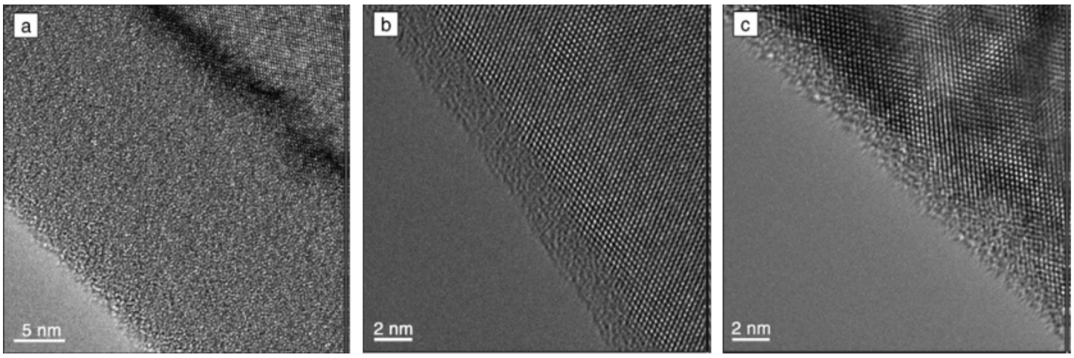

Figure 1.15: Thickness difference of amorphous layer of Si using FIB voltages of (a) 30 kV, (b) 5 kV, and (c) 2 kV, resulting in amorphous layers of (a) 22 nm, (b) 2.5 nm, and (c) 0.5-1.5 nm thickness, respectively. Adapted with permission from Ref (Mayer, Giannuzzi et al. 2007).

1.6 Motivation and aim of dissertation

As the tuning of catalysts for higher activities spans from the atomic to the meter scales, it is imperative to investigate heterogenous catalytic and other functional materials under various length scales. The fact, that there is no single technique able to cover all length scales, triggers the necessity to simultaneously conduct several complementary techniques to cover all the scales. One of the best means to study with respect to the length factor is microscopy, where not only the visuals but also the other physiochemically derivable features involving the use of other techniques, such as spectroscopy and scattering method. Although numerous microscopic investigations are usually carried out in 2D, the 3D imaging offers more advantages for its more accurate description of materials, more valuable information, and direct use for simulation/modelling. Moreover, the idea of “online/live” monitoring of catalyst morphology under reaction conditions is also mandatory because many intermediate or unstable structures are present during such transitional states.

The dissertation emphasizes the importance of *in situ* studies, 3D imaging techniques, as well as the complementary nature between X-ray and electron imaging in the field of heterogeneous catalysis. Ultimately, the work aims to develop a tool for enabling *in situ* 3D imaging studies of functional materials or catalysts via complementary X-ray and electron microscopy. The first chapter of the work focuses on the complementary *ex situ* techniques in 3D imaging using X-rays and electrons, along with the fact that 3D imaging is versatile as a qualitative and quantitative technique. Three different 3D imaging techniques, i.e. one from X-ray and the other two from electron, were introduced and compared in terms of their spatial resolutions, measurement time, fields of view, and working conditions. Eventually, it was found out that each technique has its own advantages and disadvantages, so each one of them is apparently complementary to the other. However, a particular focus is brought into highlight for complementary methods between electron tomography and ptychographic X-ray computed tomography, which are were used from this point onwards for other successive studies.

The second chapter further exhibits the versatility of 3D imaging for simulation/modelling, complementary X-ray and electron techniques, and bridges the gap between the previous and next chapter in this dissertation. Here, the investigation was carried out before and after thermal annealing process under several temperature points to foresee the benefits and necessity of implementing *in situ* studies for the next section. The results were further explored for modelling of pore network as the material owns a continuous porosity and for simulations to reveal the intrinsic physical properties, i.e. gas permeability and diffusivity, electrical and thermal conductivity as these are useful information for optimization of material performances in the applications of many catalytic oxidation/reduction, electrocatalysis, and photocatalysis. The complementary nature between electron tomography and ptychographic X-ray computed tomography proved to be useful here since multi length scale features (both on material and porosity) from sub-nm to µm scale could be synergistically unravelled.

Last, the third chapter explores the benefits and potential applications of *in situ* X-ray imaging both in 2D and 3D, starting from the development (configuration and fluid flow simulation) of the two *in situ* cells for specific purposes and sample requirements, to the applied case studies in the form of thermal annealing of several catalytic or functional materials. The cells have proved to be usable for complementary X-ray ptychography and transmission electron microscopy. Although there is not any electron tomography result under a gas flow yet (only in vacuum), the limited-angle ptychographic X-ray computed tomography results were presented to approve the capability to perform *in situ* 3D imaging, which is one of the dreams in X-ray imaging methods.

2 Multimodal *ex situ* 3D imaging studies of nanoporous gold[1]

2.1 Background

This chapter is the first step of the work to test the advantages and disadvantages of three different 3D imaging techniques, where each was done *ex situ*, using nanoporous gold (npAu) as the object of interest. The reason to choose npAu is due to its multiscale material from nm to mm scale, comprising pores and connecting ligaments around 10-50 nanometres depending on the preparation routes (Erlebacher, Aziz et al. 2001, Hodge, Biener et al. 2005, Zielasek, Jurgens et al. 2006, Wittstock, Zielasek et al. 2010). The pure npAu itself is already a working catalyst due to its high amount of accessible Au atoms on the surface, particularly at kink and step sites, which are versatile in catalysis and sensors (Wittstock, Biener et al. 2010, Wittstock and Bäumer 2014). In catalysis, the structural parameters, such as surface area, porosity, shape and mechanical stability, are extremely related to the catalytic activity since they are useful to identify and control synthesis parameters leading to the most active ones (Shi, Schaefer et al. 2014, Xu, Sui et al. 2017) as well as to design new catalysts for specifically targeted systems (de Winter, Meirer et al. 2016, Li, Luo et al. 2017). Therefore, microscopy or analytical structural imaging methods are imperative for that purpose, ideally with high spatial resolution, large field of views across multi length scales, and non-invasive nature for the source (Weckhuysen 2009, Grunwaldt, Wagner et al. 2013, Liu, Meirer et al. 2016).

The nanostructures of npAu have often been characterized using electron microscopy, i.e. SEM or TEM, to analyse its structural stability after thermal treatment or morphological alteration after metal oxide doping in 2D perspective (Wittstock, Biener et al. 2010, Tan, Davis et al. 2012, Wichmann, Wittstock et al. 2013, Bagge-Hansen, Wichmann et al. 2014, Shi, Schaefer et al. 2014, Wichmann, Bäumer et al. 2015). Moreover, XRP has also been used to investigate in 2D the effect of temperature, gas environment and the addition of metal oxide on the structure of npAu (Baier, Damsgaard et al. 2016, Baier, Wittstock et al. 2016, Fam, Sheppard et al. 2019). However, those 2D imaging methods are limited only in analysing the structure from a projection-based 2D perspective, where the intact structural features in the bulk material is mostly undisclosed, making the observation results less accurate.

Tomography-based 3D imaging methods are thus a great solution for the aforementioned problems and have been applied in characterisation of heterogeneous catalysts (Koster, Ziese et al. 2000, Midgley, Ward et al. 2007, Weckhuysen 2009, Dierolf, Menzel et al. 2010, Grunwaldt and Schroer 2010). Aside from visualizing both external and internal structure, tomographic techniques are also capable of extracting the surface area and porosity data, which are important in catalysis (Chen-Wiegart, Wang et al. 2012, da Silva, Mader et al. 2015, Mangipudi, Radisch et al. 2016, Neusser, Eppler et al. 2017). Several tomographic techniques have been demonstrated for studying npAu. ET was utilized to investigate the pore structure in sub-nm resolutions (Fujita, Qian et al. 2008), along with EDX to map distribution of Ag as the residual from

---

[1] The text and figures are adapted with permission from Ref: Fam, Y., T. L. Sheppard, A. Diaz, T. Scherer, M. Holler, W. Wang, D. Wang, P. Brenner, A. Wittstock and J.-D. Grunwaldt (2018). "Correlative Multiscale 3D Imaging of a Hierarchical Nanoporous Gold Catalyst by Electron, Ion and X-ray Nanotomography." ChemCatChem **10**(13): 2858-2867. Copyright © 2018 Published by Wiley.

dealloying process (Mahr, Kundu et al. 2017). A FIB-SV study was also carried out to capture projections of the exposed surfaces after each slicing of thin layers of npAu (Cantoni and Holzer 2014). Another report via Transmission X-ray microscopy could successfully map the pore structure at quite high spatial resolution with only using a fixed-energy laboratory source (Li, Luo et al. 2017). Nevertheless, there is not any study using PXCT for npAu, except the recent one from our group (Fam, Sheppard et al. 2018), as PXCT is an emerging synchrotron-based method, but it exploits the high spatial resolution of XRP for 3D imaging (Dierolf, Menzel et al. 2010, da Silva, Mader et al. 2015, Holler, Guizar-Sicairos et al. 2017).

In this work, three tomographic methods were performed via ET, FIB-SV, and PXCT using ceria-doped nanoporous gold (CeO_2/npAu) as the model. The comparison in terms of performance and resulting structural information are presented to conclude each of their advantages and limitations in the end. Particularly, PXCT is highlighted here as a developing 3D imaging technique with a potential benefit in catalysis.

2.2 Experimental

2.2.1 Sample preparation

CeO_2/npAu catalyst was chemically-prepared by dealloying process of Ag-Au composite, followed by wet impregnation with Ce-containing solution from a detailed method described in a previous publication (Shi, Schaefer et al. 2014). A piece of CeO_2/npAu was placed on an SEM stub, then cut and shaped using Ga^+ ion beam using a FIB Strata 400S (FEI, USA) to meet the sample requirements for ET and PXCT (Figure 2.1). The remaining sample on the stub was retained for FIB-SV.

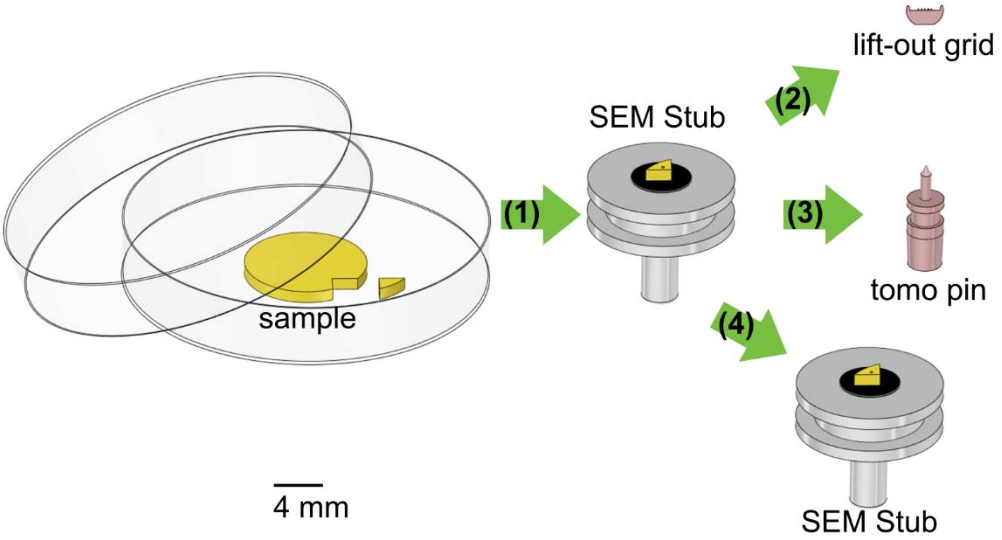

Figure 2.1: Overview of CeO_2/npAu sample preparation for ET, PXCT, and FIB-SV (Fam, Sheppard et al. 2018).

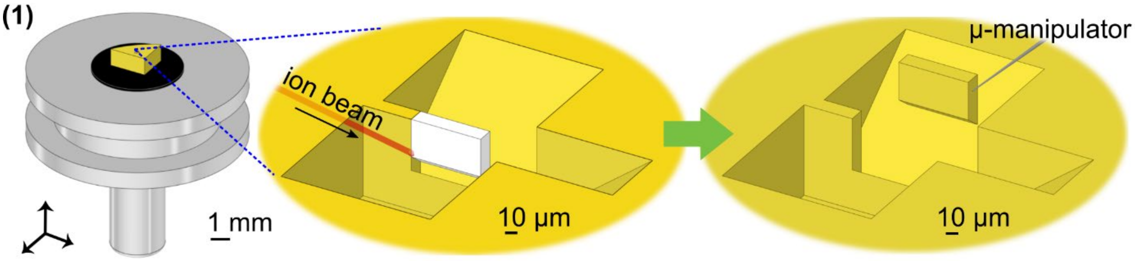

Figure 2.2: Monolithic CeO_2/npAu was mounted on a stub and cut by Ga^+ beam. A small piece of material was extracted by FIB manipulation (Fam, Sheppard et al. 2018).

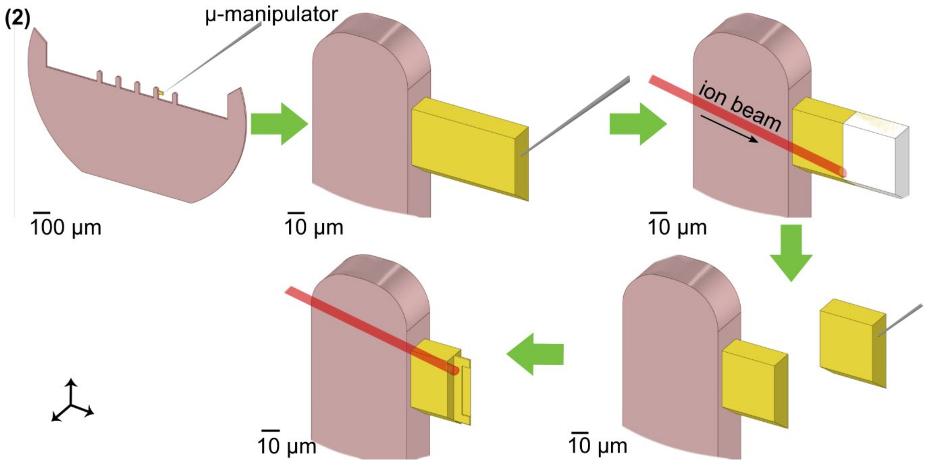

Figure 2.3: The CeO_2/npAu piece extracted from the stub was moved to a lift-out grid by FIB manipulation. This piece was then thinned down by Ga^+ beam to <300 nm thickness for ET measurement (Fam, Sheppard et al. 2018).

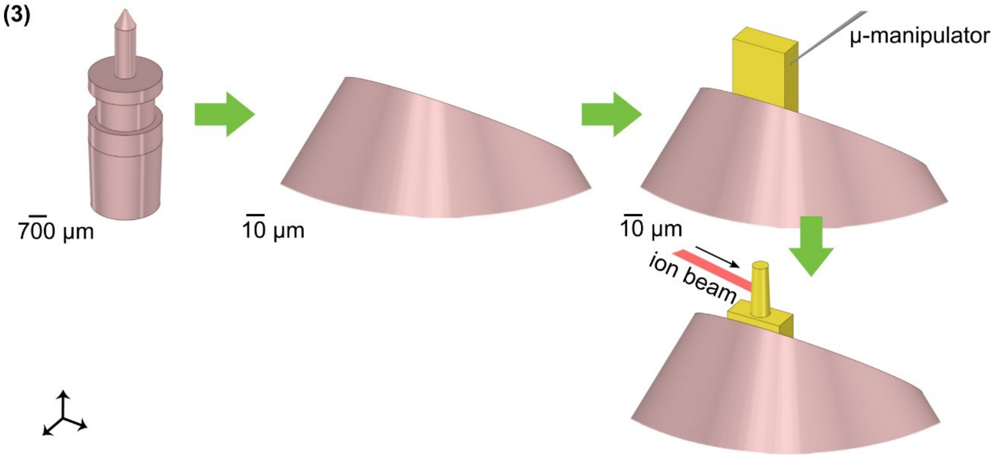

Figure 2.4: (Left) Customized Cu pin developed at cSAXS beamline (Swiss Light Source); (Middle-Right) a small piece of CeO_2/npAu from the lift-out grid was moved to the Cu pin by FIB manipulation, which was then cut into a cylindrical shape for PXCT measurement (Fam, Sheppard et al. 2018).

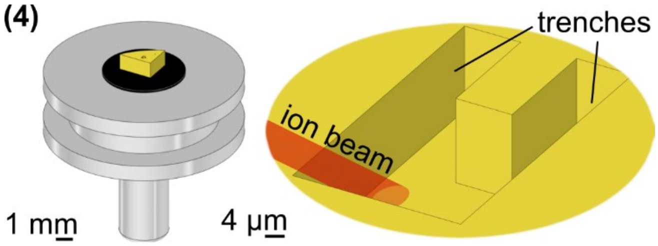

Figure 2.5: The remaining CeO_2/npAu on the stub (Figure 2.2) was cut into a rectangular prism by Ga^+ beam for FIB-SV measurement (Fam, Sheppard et al. 2018).

2.2.2 Three tomographic studies

PXCT measurement made use a cylindrical CeO_2/npAu sample (10 µm diameter and 30 µm height) as the sample, prepared using FIB milling and deposited on an OMNY pin (Holler, Raabe et al. 2017). PXCT measurements were performed at the coherent small angle X-ray scattering (cSAXS) beamline of the Swiss Light Source at the Paul Scherrer Institute (Villigen, Switzerland), using the typical flexible tomography nanoimaging endstation (flOMNI), which operates in air and at room temperature (Holler, Raabe et al. 2012, Holler, Diaz et al. 2014). A differential laser interferometry was used for high-accuracy positioning of the sample with respect to the illuminating optics (Holler and Raabe 2015). The coherent X-ray illumination onto the sample was determined using an Au-made Fresnel zone plate (FZP) of 120 µm diameter, a focal length of 50.54 mm, and X-ray photon energy of 8.7 keV, offering a flux of about 1.4 x 10^8 photons/s. The sample was placed 1 mm downstream from the focus, with illumination diameter on the sample of 3 µm. Coherent diffraction patterns were recorded using a Pilatus 2M detector with 172 µm pixel size positioned 7.399 m downstream from the sample (Kraft, Bergamaschi et al. 2009). A field of view of 14*8 μm^2 (h*v) was recorded per projection with an average distance between points of 0.8 µm following a Fermat spiral trajectory (Huang, Yan et al. 2014). The scan was repeated with angular positions ranging from 0 to 180° of the specimen with respect to the incoming X-ray beam for a total of 900 equal angular steps. Each measurement point had an acquisition time of 0.1 s with a total of 15 h for one tomogram, including dead time in between acquisitions during sample movements. Ptychographic reconstructions were directly done using difference map algorithm followed by maximum likelihood optimization as a refinement step (Thibault, Dierolf et al. 2009, Thibault and Guizar-Sicairos 2012). Each pair of scans was recorded at different angles and positions of the detector and were then combined in the same reconstruction, where two different images could be reconstructed under the same illumination, as introduced in previous work (Holler, Diaz et al. 2014). An area of 460*460 detector pixels was used in the ptychographic reconstructions to obtain reconstructed images with a pixel size of 13.32 nm. The phase contrast images were then further processed to correct zero- and first-order terms and were registered in the vertical and horizontal direction (Guizar-Sicairos, Diaz et al. 2011). The effective spatial resolution of the resulting images was estimated to be around 23 nm via Fourier shell correlation (FSC) of two sub-tomograms, where each of them was computed with half of the angular projections, using the half-bit threshold criterion (van Heel and Schatz 2005). The total estimated dose imparted on the specimen for data acquisition was about 8.28 x 10^8 Gy.

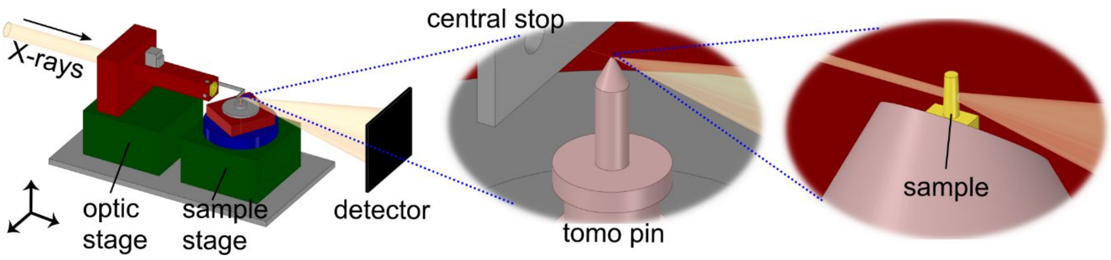

Figure 2.6: Illustration of PXCT setup at the cSAXS beamline, CH (Fam, Sheppard et al. 2018).

ET measurement made us a lamella of CeO_2/npAu (~300 nm thickness) as the sample, produced by FIB milling and attached onto a lift-out grid. ET measurement was performed using a Fischione tomography holder, on a Titan 80-300 (FEI) microscope operated at an acceleration voltage of 300 kV in STEM mode, at the Institute of Nanotechnology (INT) at Karlsruhe Institute of Technology (Karlsruhe, Germany). The tilt series of high-angle annular dark-field STEM images were collected with the Xplore3D software (FEI) over a tilt range of ±60°, with tilt increment of 2°. Alignment of the tilt series was completed in IMOD software using the cross-correlation function. The aligned tilt series were reconstructed using the Simultaneous Iterative Reconstruction Technique (SIRT) with the Inspect3D software (FEI) and the resultant reconstructed tomogram had a final voxel size of 1.3 nm.

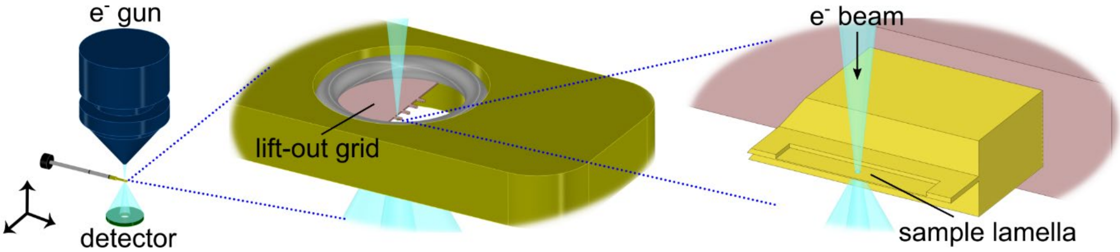

Figure 2.7: Illustration of ET setup at the INT, DE (Fam, Sheppard et al. 2018).

FIB-SV measurement made use a piece of CeO_2/npAu placed on a standard SEM sample holder stub. The measurement was performed at the Laboratory of Electron Microscopy (LEM) at Karlsruhe Institute of Technology (Karlsruhe, Germany), using an EsB 1540 dual-beam FIB-SEM (Zeiss, Germany) equipped with an external Raith Elphy Plus pattern generator. The sample was placed at a eucentric height, allowing the imaging plane to be scanned with the electron beam under an angle of 54° without changing sample position. A Ga^+ beam with 30 kV voltage and 0.5 to 10 nA current was used to expose a rectangular prism shaped sample with 8.47 µm width (x direction) and 10.80 µm height (y direction). Slice and view process was then carried out by sequential Ga^+ beam erosion of thin layers in z direction with around 15 nm slice thickness, slice width of 14.95 µm, and 50 pA current. In-lens secondary electron imaging was used to produce a surface map of each exposed slice. During image acquisition, the imaging plane moved stepwise in z direction from the sequential ion-milling, which eventually resulted in 950 images with a pixel size of 12.78 nm and an effective spatial resolution of around 15-45 nm.

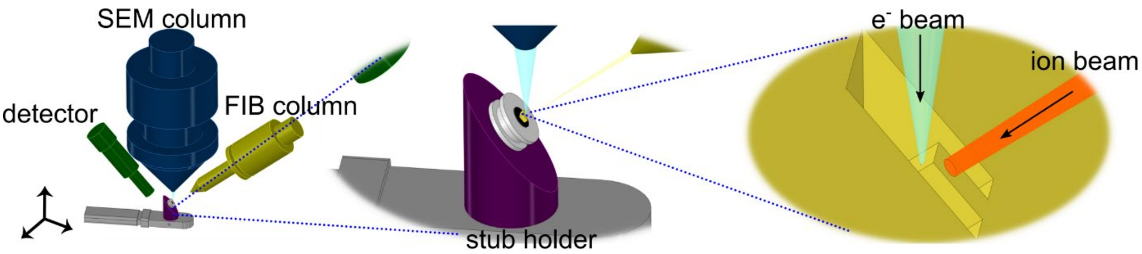

Figure 2.8: Illustration of FIB-SEM-CT setup at the LEM, DE (Fam, Sheppard et al. 2018).

2.2.3 Image processing and analysis

Reconstructed data was rendered using the software package Avizo 9.3 (FEI Company). Default settings were applied for each data treatment module unless otherwise stated.

PXCT: TIFF images of 551 slices of cylindrical CeO_2/np-Au were used as the image source in Avizo, which were combined into a single volume with isotropic voxel size of 13.3 nm. A 'Non-Local Means Filter' module was employed to remove data noise. The filtered file was segmented into three bodies: CeO_2/np-Au, pores, and the central void. Exterior voxels including surrounding air and 2D frame padding were discarded using a circular binary mask. 'Threshold' tool was firstly used to approximately define CeO_2/np-Au and pores. Next, 'Watershed' tool was used to automatically compute a suitable contrast gradient between the selected np-Au and pore histogram values with the help of generated gradient image. 'Brush' tool was employed to roughly assign the central void volume. The segmentation was interpolated every 50 slices, followed by 'Watershed' to finalize the results. Finally, 'Lasso' tool was used to distinguish between exterior and pore voxels. Pores and CeO_2/np-Au were then visualized individually in 3D via 'Volume Rendering' module. To obtain the values of volume (V) and surface area (S), 'Label Analysis' module with 3D interpretation was used. Further analysis to show np-Au ligament and pore size distribution was carried out using 'Separate Objects' module, followed by 'Label Analysis' module with customized measurement parameters to calculate equivalent diameter as the ligament or pore size.

ET: A single REC file containing lattice info of the CeO_2/np-Au lamella was used as the image source in Avizo. The isotropic voxel size was set to 1.3 nm. A 'Non-Local Means Filter' module was employed to remove data noise. The filtered file was segmented into two bodies: CeO_2/np-Au and pores. Exterior voxels were discarded. 'Threshold' tool was firstly used to approximately define CeO_2/np-Au and pores. Next, 'Blow', 'Brush' and 'Interpolate' tools were employed to manually distinguish each part. Each segmented body was then visualized in 3D via 'Volume Rendering' module. To obtain the values of volume (V) and surface area (S), 'Label Analysis' module with 3D interpretation was used. Further analysis to show np-Au ligament and pore size distribution was carried out using 'Separate Objects' module, followed by 'Label Analysis' module with customized measurement parameters to calculate equivalent diameter as the ligament or pore size.

FIB-SV: TIFF images of 750 slices of box-like CeO_2/np-Au were used as the image source in Avizo, which were combined into a single volume with isotropic voxel size of 12.9 nm. A 'Non-Local Means Filter' module was employed to remove data noise. The filtered image stack required alignment, so 'FIB Stack Wizard' module was employed. Least-squares method was adopted in this case and the produced slices were then cropped, so that the material body was visible in all slices. Shear angle was set to 36° so as to correct the viewing angle of 54° during measurement. The aligned image stack was segmented into two bodies:

CeO_2/np-Au and pores. Exterior voxels were discarded. ‘Threshold’ tool was firstly used to approximately define CeO_2/np-Au and pores. Next, ‘Watershed’ tool was used to automatically cover the missing areas with the help of generated gradient image. ‘Lasso’ tool was used to distinguish between exterior and pores on the first and last slices, whereas the rest of the slices were carried out by interpolation. Due to the shearing correction during alignment, the segmented volume was manipulated onto Cartesian axes using ‘Resample Transformed Image’ module. Each segmented body was then visualized in 3D via ‘Volume Rendering’ module. To obtain the values of volume (V) and surface area (S), ‘Label Analysis’ module with 3D interpretation was used. Further analysis to show np-Au ligament and pore size distribution was carried out using ‘Separate Objects’ module, followed by ‘Label Analysis’ module with customized measurement parameters to calculate equivalent diameter as the ligament or pore size.

‘Label Analysis’ module with 3D interpretation was used to obtain several values of ‘Volume3d’, representing the corresponding segmented volume (see Volume in Table 2) and ‘Area3d’ representing the corresponding segmented surface area (see Area in Table 2). Further analysis to show the size distributions of np-Au ligament and pore was carried out using the ‘Separate Objects’ module to cut the continuous volume structure into individual subunits. This was followed by ‘Label Analysis’ module with customized measurement parameters to calculate ‘Equivalent Diameter’ as the ligament or pore size of each subunit with the following formula:

$$Equivalent\ Diameter = \sqrt[3]{\frac{6 * \text{Volume}}{\pi}}$$

From the resulting pore size distribution values, further calculation of pore sphericity was also applied using the following formula, derived from Wadell et al:[2]

$$Equivalent\ Diameter = \frac{\pi^{\frac{1}{3}} * (6 * Volume)^{\frac{2}{3}}}{A}$$

Volume3d = volume of the object, A = surface area of the object. The above equation represents the ratio of the surface area of a sphere (with the same volume as the object of interest) to the surface area of the subunit being measured after object separation. A sphere has pore sphericity value of 1, objects deviating from this value as regarded as progressively less spherical. The average of such distributed values (see Average Pore Sphericity in Table 1) is versatile enough to generally show how spherical the segmented pore is for each technique. It should be noted that approximating pores to spheres is only one method of pore volume analysis. By applying this consistently for all three nanotomography techniques, any errors resulting from the measurement should be proportional for all three techniques.

2.3 Results and Discussion

Following sample preparation, each tomographic technique was carried out separately to analyse the CeO_2/npAu sample. The principle behind each method and its subsequent reconstruction procedure is that a series of 2D images of the probed sample are turned into 3D data volumes, where 2D data are projection images at various rotational angles for PXCT and ET, while only 2D scanning images after sequential ion beam cutting are obtained for FIB-SV. Figure 2.9 shows a representation of projection/scanning images from each technique, which can later be reconstructed and visualized as a 3D volume image. All the 2D images from three techniques clearly exhibit a sponge-like structure with distinguishable pore and ligament sizes (Wichmann, Wittstock et al. 2013, Shi, Schaefer et al. 2014, Baier, Wittstock et al. 2016, Mahr, Kundu et al. 2017). The presence of finely structured ligaments and some denser parts indicate a mild coarsening from the doping procedure of metal oxide (i.e. CeO_2 particles) over npAu, which involved a thermal treatment of 280 °C for the removal of organic residues. However, the thick layers on the exterior parts, particularly for FIB-SV (Figure 2.9b), should unavoidably be the damaged material from the Ga^+ milling during sample cutting by FIB. From one projection image of ET, an EDX analysis was performed to verify the presence of CeO_2 (Figure 2.9d) resulting in a Ce content of 4.2 %w or 5.2 %A, which is within the range as previously reported, 2-10 At.% (Shi, Schaefer et al. 2014).

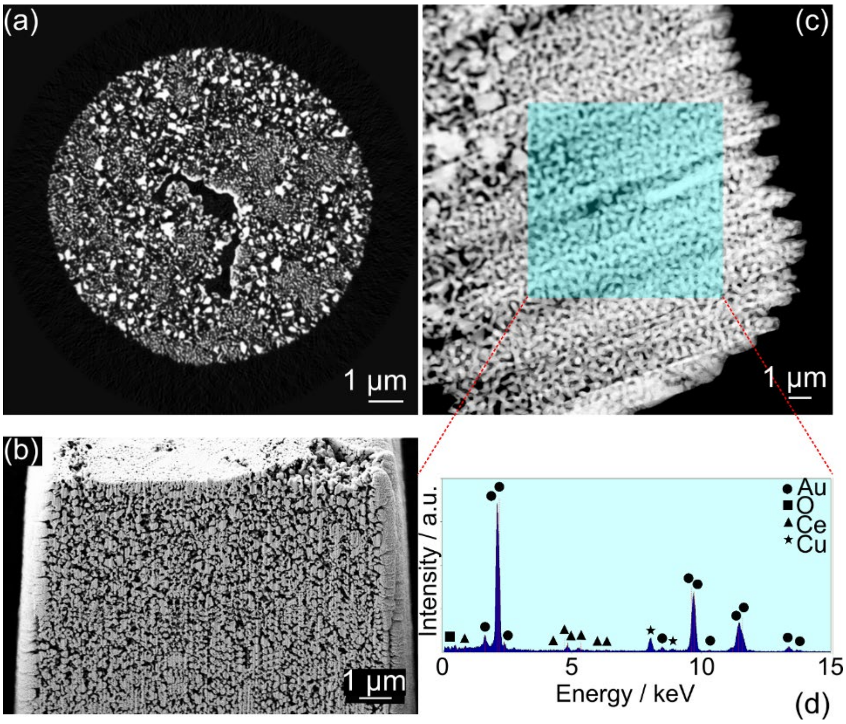

Figure 2.9: 2D perspective of CeO_2/npAu from: (a) PXCT - orthographic slice through the phase contrast tomogram following reconstruction; (b) FIB-SV - secondary electron image of a typical surface exposed during cutting; (c) STEM image of CeO_2/npAu and (d) corresponding EDX spectrum acquired from the shaded area. (Fam, Sheppard et al. 2018)

Those 2D data then underwent their own tomographic image reconstruction procedures (detailed in Experimental section) for the transformation into 3D volumes, which was made into a visual using Avizo software as shown in Figure 2.10. The rendered results clearly show more obvious sponge-like structure and porosity compared to the ones in Figure 2.9. In terms of field of view, PXCT and FIB-SV probed much greater volumes (two orders of magnitude more) than ET in Figure 2.10, which is an inevitable drawback from the limited high penetration of electron as the light source, especially at high tilting angles, where high attenuation occurs. Another noticeable feature is the crack visible in the middle volume from PXCT (Figure 2.10a-b), which is induced by a mechanical fracture during sample preparation by FIB. However, such a crack from PXCT and the thick layer from FIB-SV were not included as the pore and sample, respectively, so they were also excluded for further analysis and calculations.

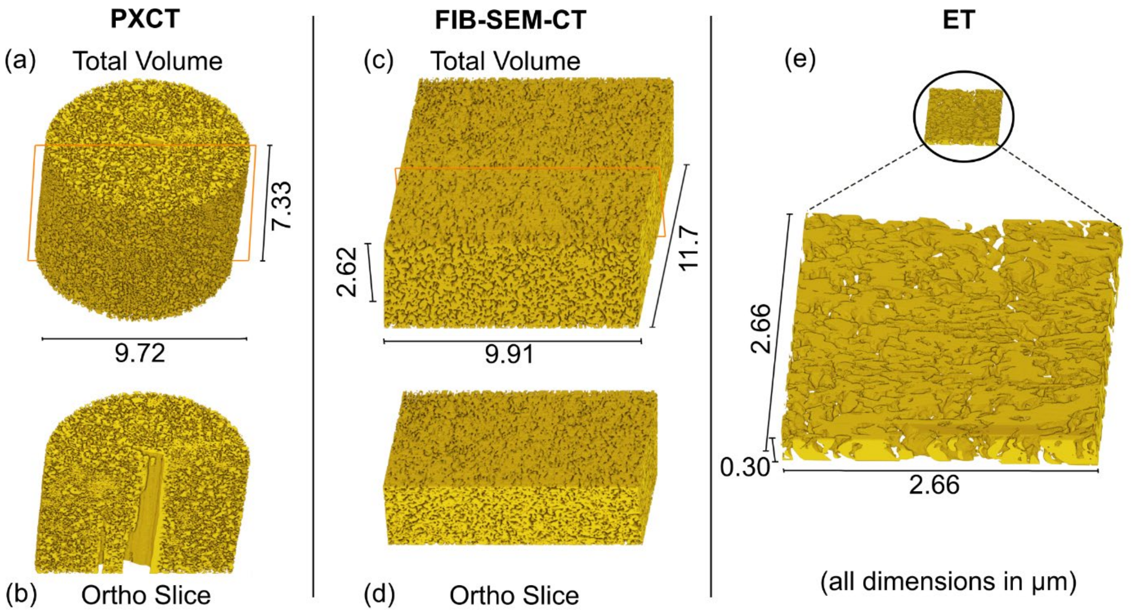

Figure 2.10: Volume rendering of (a) whole and (b) bisected CeO_2/npAu pillar via PXCT; (c) whole and (d) bisected CeO_2/npAu cuboid via FIB-SV; (e) CeO_2/npAu lamella to scale (above) and magnified (below) via ET. Ortho slice planes indicated by red lines. (Fam, Sheppard et al. 2018)

For quantitative analysis, the average diameter of the ligaments and pores were obtained, depending on the spatial resolutions of each technique. The averaging procedure was based on the accumulation of smaller units in different positions over the sample, then the size of ligaments and pores were estimated by fitting spheres or ovoids and calculating the corresponding diameters, listed in Table 1, together with other parameters and characteristics. Comparing between the three techniques, the varying values of ligament and pore size and sphericity can be attributed to sample preparation, statistical variance, and/or spatial resolution limit of the technique. In terms of pore size, the lowest average was extracted from ET (61 nm), comparable to our previous work of ~40 nm by TEM (Wittstock and Bäumer 2014), followed by FIB-SV and PXCT (195.9 and 288.6 nm, respectively). The ligament and pore size distribution are shown in Figure 2.11, where they are divided into two regions, contributing to the average values shown in Table 1. For ET, the pore and ligament size are distinguishably lower than the ones of PXCT and FIB-SV, which should be due to the much smaller probed volume. Since the ET sample is in the form of lamella with a thickness of around 300 nm, whereas PXCT and FIB-SV indicate the presence of larger pores between 100 and 600 nm, this shows that the lamella does not actually represent the bulk material despite the capability to detect much smaller pores due to the higher spatial resolution of ET. Besides, FIB-SV exhibits a higher proportion of ligaments and thus a lower average size of pores than the ones of PXCT, which can be induced by the ablation of material layers after each slicing process in FIB-SV, where sintering of the sample is inevitable along with the increasing usage of FIB cutting. Additionally, FIB-SV in this case also created ‘shine through’ artefacts (Mangipudi, Radisch et al. 2016), where subsurface material below the slice of scanned images cause oversampling of ligament and hence undersampling of pores, particularly during segmentation process. On the other hand, PXCT is apparently non-invasive and relatively less damaging than the other two methods.

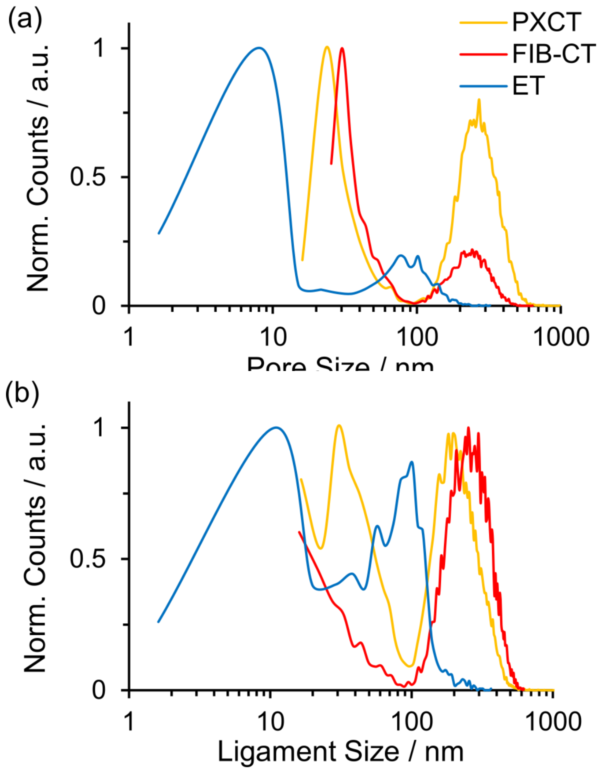

Figure 2.11: Normalised distribution profile of (a) pore size and (b) ligament size of CeO_2/npAu from three techniques. (Fam, Sheppard et al. 2018)

Table 1: Measurement of volume-rendered CeO_2/npAu from three techniques. (Fam, Sheppard et al. 2018)

Method	Approx. Spatial Resolution (nm)	Pixel Size (nm)	Probed Volume (µm^3)	Av. Ligament Size (nm)	Av. Pore Size (nm)	Av. Pore Sphericity
PXCT	23	13.3	9.72*9.72*7.33	211±23	288±23	0.51
FIB-SV	38.4	12.8	9.91*11.7*2.62	277±15	195±15	0.62
ET	3.9	1.3	2.66*2.66*0.30	75±2	61±2	0.81

As previously mentioned, the values of spatial resolution in fact effect the difference in the values of other measurement characteristics in Table 1 between three methods. The effect was apparent during image segmentation, which critically determines the measurement of physical properties in Table 1. In this case, two methods were used to determine the spatial resolution. For PXCT, a spatial resolution of 23 nm was calculated via Fourier shell correlation (van Heel and Schatz 2005). For ET and FIB-SV, estimation of their spatial resolutions were based on the pixel size and slice thickness (for FIB-SV only) by measuring the number of pixels used to resolve the interface between material and pores, where both techniques exhibit the amount of 3 pixels. Nevertheless, the difference in pixel size between them results in spatial resolution of 38.4 nm for FIB-SV and 3.9 nm for ET. The highest result from ET is expected since it has been famous to be able to attain atomic resolutions (Miao, Ercius et al. 2016), although this value of 3.9 nm can be considered quite low due to the large field of view from low magnification image capture in this case and perhaps also owing to the aberration and astigmatism effects. For FIB-SV, higher results could be obtained by reducing the field of view and slice thickness, but the effect of sample drift increases, which should be taken into consideration during the reconstruction (Munroe 2009). In this study, a beam energy of 30 kV, 50 pA was used to minimize the ion beam damage during FIB-SV so as to probe a comparable volume to that of PXCT with similar spatial resolutions.

The influence of spatial resolution is mostly predominant on the ligament/pore size distribution profiles in Figure 2.11. ET is obviously the unique among the three techniques with a visible skewness towards values under 15 nm for its highest spatial resolution, which is a huge advantage as such region are not detectable to both PXCT and FIB-SV. However, the regions with peaks around 100 nm for ET are less plausible because of the approaching size to the lamella thickness (300 nm), so they are not really representative. For those reasons, ET is in reality best in probing sample at the lower end of the multi length scales. For PXCT and FIB-SV, the peaks around 20 – 30 nm simply implies the lower spatial resolution than ET, but the presence of much larger pores close to 1 µm reflects their suitability for probing higher end of the multi length scales, which is an excellent quality for high reliability in capturing features possibly not visible in the size of lamella. Between PXCT and FIB-SV, the favour is in the former due to its non-invasive and non-destructive features since the latter naturally requires complete destruction of the sample.

Spatial resolution also plays a significant role in the segmentation process, which determines the values in Table 1. Since all three methods produce grayscale slice images for 3D visualization process, there are some grey areas in the images denoting partial volume effects, where the borders between pores and materials are not resolvable due to the limited spatial resolution of the techniques. Therefore, undersampling or oversampling is unavoidably mandatory to differentiate between materials and pores, particularly for FIB-SV in this case, where the problem of shine-through artefacts inevitably aggravate the oversampling of material and undersampling of pores. On the other hand, the same thing could also happen to PXCT in this work, where the initial manual thresholding or even automatic watershed segmentation process could lead to either undersampling or oversampling the material. This hence suggests the importance of spatial resolution in determining the resulting quality of imaging techniques, so both technique and sample should be considered based on the size range of the features of interest.

Moreover, a deeper study of the structural parameters are also of high importance in the field of catalysis (Shi, Schaefer et al. 2014, Mahr, Kundu et al. 2017). Here, porosity (%), pore volume (V_p / m^3g^{-1}) and effective surface area (S.A. / m^2g^{-1}) of CeO_2/npAu were derived for each technique as listed in Table 2. For catalyst samples, S.A. and V_p or pore diameter are usually measured via physisorption techniques (Tan, Davis et al. 2012). As the elemental composition of CeO_2/npAu was acquired via EDX-TEM technique and the sample volume was obtainable from each technique, the values of S.A. and V_p are accordingly able to derive. Aside from the bulk volume, several subvolumes (Figure 2.12) were also extracted and calculated in the same way for statistical purpose with the only exception for ET data because of its much smaller probed volume.

Table 2: Calculated physical properties of CeO$_2$/npAu following tomographic label analysis. (Fam, Sheppard et al. 2018)

Method	CeO$_2$/npAu				Pore			
	Sample	Volume (µm^3)	Area (µm^2)	S.A. (m^2/g)	Volume (µm^3)	Area (µm^2)	V$_p$ (m^3/g)	Porosity (%)
PXCT	Total	205.6	7498	2.06	304.0	7718	0.083	60
	Sub-V 1	0.050	2.94	3.30	0.079	3.25	0.089	61
	Sub-V 2	0.043	2.49	3.30	0.087	2.80	0.115	67
	Sub-V 3	0.047	1.98	2.41	0.083	2.22	0.101	64
	Sub-V 4	0.052	2.13	2.32	0.078	2.45	0.085	60
	Sub-V average	0.048	2.39	2.83	0.082	2.68	0.098	63
	Sub-V error*	±0.015	±0.02	-	±0.015	±0.02	-	-
FIB-SV	Total	190.4	5265	1.56	123.8	5425	0.037	39
	Sub-V 1	0.089	2.85	1.81	0.039	2.21	0.025	31
	Sub-V 2	0.083	2.99	2.03	0.045	2.47	0.031	35
	Sub-V 3	0.081	2.99	2.09	0.047	2.54	0.033	37
	Sub-V 4	0.090	3.55	2.22	0.038	3.07	0.024	30
	Sub-V average	0.086	3.10	2.04	0.042	2.57	0.028	33
	Sub-V error*	±0.015	±0.02	-	±0.015	±0.02	-	-
ET	Total	0.998	53.85	3.043	1.104	62.77	0.062	52.5

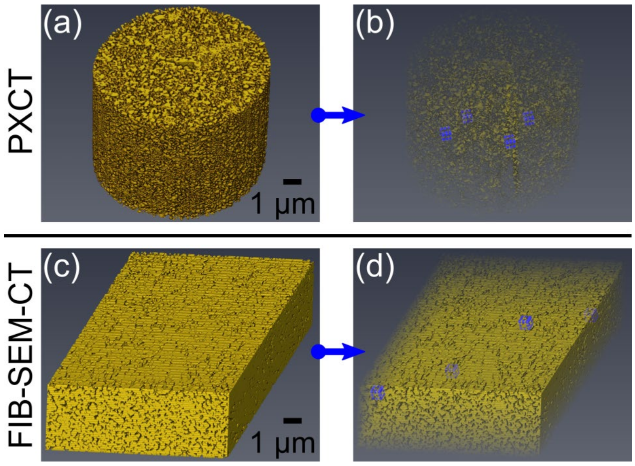

Figure 2.12: Subvolume extraction from: (a) PXCT data and (b) selection of four PXCT subvolumes; (c) FIB-SV data and (d) selection of four FIB-SV subvolumes. All subvolumes had dimensions of 0.5*0.5*0.5 µm^3 and are highlighted in blue, volumes (b) and (d) were rendered with transparency. (Fam, Sheppard et al. 2018)

Table 2 indicates the proportionality of the total volume of CeO$_2$/npAu and pores to the probed volume in Table 1, hinting that the voxel counting process is valid. As percentage porosity means the ratio of material to pore, PXCT and ET both possess the values close to the range reported before, e.g. 60 to 80 vol% (Hodge, Hayes et al. 2006, Wittstock, Wichmann et al. 2012). While the value from PXCT is expected since it is considered the most representative of the bulk material, it is not the case for the thin lamella from ET. On the other hand, the value from FIB-SV is significantly low, which emphasizes the aforementioned damaging effect of the ion beam during slicing process. With regards to effective surface area, the calculated S.A. from all three techniques are in the range of 1.6 to 3.3 m^2/g, whereas the minimum value reported for a pure npAu sample was 4 m^2/g (Wittstock, Wichmann et al. 2012, Shi, Schaefer et al. 2014). This can be explained by considering the inverse relationship between ligament size and surface area (Rösner, Parida et al. 2007). Since the observed porosity did not attain the reported 60%, ligament sizes were consequently larger and surface area was therefore lower. Furthermore, the influence of spatial resolution is also prevalent on the calculation of pore volume and surface area in this case. While ET emphasized on the micropores (<2 nm) and mesopores (2-50 nm), both PXCT and FIB-SV focused on the meso- and macroporosity (>50 nm), so there is not a single technique covering all scales. In general, the subvolume analysis is useful to point out the inhomogeneous trait of the sample, which could hint the existence of coarsened ligaments.

To sum up, this work verifies the versatility of tomographic methods to construe porosity in functional materials and how it is in line with the results from experimental methods. Not only visualizing the material and pore network in 3D space, but deriving quantitative values of important parameters (in catalysis) are also possible. Tomographic results can also be further used in modelling of porosity for catalytic materials for elucidating the mechanism behind adsorption, diffusion, or mass transport of the gas reactants into the catalysts. From those three methods in this case, electron-based imaging techniques offer higher spatial resolutions down to single-digit nm, while PXCT is currently limited in mesoscales. In terms of data processing workflows, FIB-SV and ET data can be processed using commercial and even free software, while PXCT data have to be processed specifically depending on the beamline, where the experiments are carried out, because it is still a developing method. However, PXCT has a strong advantage to measure extended sample in a non-invasive manner compared to ET and FIB-SV. Among techniques under X-ray microscopy, the spatial resolution of PXCT is uniquely high and is projected to ameliorate along with the improvement in optics, detectors, reconstruction algorithm, and higher-generation synchrotron light sources. This will positively affect the total acquisition time for PXCT measurements by cutting it down to orders of magnitude, which will also enable either much larger field of view or higher spatial resolutions with reduced measurement times in line with modern ET and FIB-SV (Holler, Guizar-Sicairos et al. 2017). Last, PXCT also provides more flexibility for applications of *in situ* modes or sequential post-mortem analysis after thermal annealing. In comparison with electron, development of instruments and tools for X-ray measurement is relatively easier due to its higher penetration nature of the source as well as higher range of environmental conditions.

2.4 Conclusions

Three complementary 3D-imaging techniques are demonstrated for analysing a multiscalar CeO_2/npAu, whose resulting data volumes were used to measure physical properties, e.g. surface area, volume fraction, pore structure and network topology, relevant to catalysis. Given the non-invasive sample preparation, more representation of the bulk sample, and mesoscale spatial resolution, PXCT is the potential tool for physical characterizations, including imaging along with quantifying the physical properties, of heterogeneous catalyst samples. Nevertheless, PXCT will not exactly replace electron microscopy, but it should be an excellent complementary technique. Moreover, the possibility to perform *in situ* PXCT would be of great interest and benefits.

3 *Quasi in situ* 3D imaging study of thermal annealing of npAu[1]

3.1 Background

This chapter bridges the gap between the *ex situ* nature of the previous section and the *in situ* nature of the upcoming chapter. The work in this chapter utilizes the *quasi in situ* method, where material was sequentially treated outside and then put back into the imaging setup. It used the same material base of npAu, which has attracted significant interest due to its interesting and unexpected catalytic properties (Zielasek, Jurgens et al. 2006, Xu, Su et al. 2007, Wittstock, Zielasek et al. 2010, Kosuda, Wittstock et al. 2012, Zugic, Karakalos et al. 2016). Nevertheless, coarsening process is unfortunately unavoidable in catalytic reactions with/without elevated temperatures, especially materials with porous structure, and consequently induces gradual reduction of catalytic activity (Biener, Biener et al. 2011, Wichmann, Wittstock et al. 2013, Fujita, Tokunaga et al. 2014). To improve thermal stability of npAu, metal oxide coatings have proved to be the most efficient way (Wittstock, Wichmann et al. 2012, Shi, Schaefer et al. 2014, Qadir, Quynh et al. 2015, Ewers, Crampton et al. 2017). Hence, coarsening process with particularly the temperature profile is worth a detailed investigation along with the affected physicochemical properties of the samples, which are of high importance for future development in more efficient catalytic applications of npAu materials.

Since catalytic activity is commonly related to pore size distribution and surface area, detailed studies of pore types and structures are therefore necessary (Buurmans, Ruiz-Martínez et al. 2011, Fam and Imae 2015, Meirer, Morris et al. 2015, Ihli, Jacob et al. 2017, Krumeich, Ihli et al. 2018). Microscopic or imaging techniques, typically using electron or X-ray, have been proved to be the most effective means to simultaneously visualize and quantitatively measure the pore network and other physical properties of the materials, even in three dimension via ET (Echigo, Monsegue et al. 2013, Liu, Nishitani et al. 2014, Niehle and Trampert 2015, Madejski, Lucas et al. 2018) or PXCT (Holler, Diaz et al. 2014, da Silva, Mader et al. 2015, Fam, Sheppard et al. 2018, Li, Ihli et al. 2019). The excellent benefit of 3D imaging techniques lies mostly on the capability to generate not only the 3D morphology, but also to be able to derive the physicochemical properties (da Silva, Mader et al. 2015, Ihli, Jacob et al. 2017, Fam, Sheppard et al. 2018), while 2D imaging methods usually require other additional techniques. Besides, chemical/elemental properties could also be obtained to unravel more information using integrated extensions of those tomographic techniques, e.g. EDX tomography (Slater, Macedo et al. 2014, Polavarapu, Zanaga et al. 2016, Huber, Haberfehlner et al. 2019, Wang, Slater et al. 2019), electron energy loss spectroscopy (EELS) tomography (Nicoletti, de la Peña et al. 2013, Yedra, Eljarrat et al. 2014, Torruella, Arenal et al. 2016), energy filtered transmission electron microscopy (Goris, Bals et al. 2011) or resonant ptychographic tomography (Ihli, Diaz et al. 2018).

---

[1] The text and figures are taken from a manuscript under preparation by Fam, Y., T. L: Sheppard, A. Diaz, M. Holler, J. Ihli, T. Scherer, W. Wang, D. Wang, C. Kubel, A. Wittstock, J.-D. Grunwaldt, "*3D view and tomography-based simulations of morphological changes from thermal annealing of nanoporous gold*".

In this case, npAu is in fact an excellent material consisting of hierarchical porosity and interconnected network of macro- (>50 nm), meso-(2-50 nm), and micropores (<2 nm) (Zielasek, Jurgens et al. 2006, Wittstock, Wichmann et al. 2012). Owing to its multimodal feature, 3D imaging technique is undoubtedly a perfect tool to comprehend its 3D structure along with the physicochemical properties. Although many investigations for this material have been carried out using ET (Chen-Wiegart, Wang et al. 2012, Mahr, Kundu et al. 2017, Fam, Sheppard et al. 2018, Madejski, Lucas et al. 2018), only a few utilized PXCT and it was only *ex situ* (Fam, Sheppard et al. 2018). In order to understand its coarsening behaviour, an *in situ* method under gas flow is thus required and only 2D imaging technique via *in situ* XRP has been able to realize it so far (Baier, Damsgaard et al. 2016, Baier, Wittstock et al. 2016, Fam, Sheppard et al. 2019), while *in situ* ET under gas flow is none so far. This hence leaves an intriguingly open case study in 3D using X-ray although the reactor development and data reconstruction are challenging (Fam, Sheppard et al. 2019). Besides, 3D imaging techniques are actually more informative than the 2D counterpart due to the capability of quantitatively revealing physical properties (e.g. surface area and porosity) (Ihli, Jacob et al. 2017, Fam, Sheppard et al. 2018, Larsson, Gursoy et al. 2019, Li, Ihli et al. 2019) or chemical properties (e.g. elemental distribution) (Ihli, Diaz et al. 2018) of materials as well as further utilizing the results for modelling/simulations (Zabihzadeh, Cugnoni et al. 2017, Madejski, Lucas et al. 2018, Cuesta, De la Torre et al. 2019).

Herein, the results from *quasi in situ* PXCT of thermal annealing of npAu materials under atmospheric air are presented, followed by simulations to model the air flow and pressure map through the pores of npAu, concentration profile of CO_2 (from air) diffused on the pores of npAu, temperature profile of npAu during simulated heat transfer process, and electrical voltage map during simulated potential bias in an electrolyte solution. Therefore, not only physical properties (surface area and porosity) of npAu materials can be extracted from the resulting 3D data volume, but also their intrinsic material properties, e.g. air permeability constant and molecular diffusivity coefficient of CO_2, electrical and thermal conductivity constant of npAu materials.

3.2 Experimental

3.2.1 Sample preparation

The pure-, CeO_2-, TiO_2-, and $CeTiO_x$-incorporated npAu samples were prepared via dealloying of an Ag-Au composite, followed by wet impregnation with metal-oxide(s) precursor solution(s) using the methods described in previous reports (Shi, Schaefer et al. 2014, Shi, Mahr et al. 2016, Shi, Mahr et al. 2017). A piece of the sample was placed on an SEM sample holder stub, then cut and shaped with a Ga^+ ion beam using FIB Strata 400S (FEI, USA) into a pillar with diameters of 4-6 µm and heights of 10-30 µm, which was then deposited on an flOMNI pin (Holler, Raabe et al. 2017). Another shape in the form of a lamella with a thickness of around 100 nm was prepared for ET measurements. The detailed procedures can be observed in our previous work (Fam, Sheppard et al. 2018).

3.2.2 *Quasi in situ* PXCT with sequential heating experiment

PXCT measurements were performed at the cSAXS beamline of the SLS at the PSI (Villigen, Switzerland) with the flOMNI setup (Holler, Raabe et al. 2012, Holler, Diaz et al. 2014), including a differential laser interferometry for sample positioning in high precision (Holler and Raabe 2015). An Au-made FZP with a diameter of 170/220 µm was employed to allow the coherent part of incoming X-ray beam with a photon energy of 6.2 keV and a flux of around 4.3-21.1 x 10^6 photons/frame. The sample was illuminated with a diameter of 3 µm and placed 51 mm downstream/in focus. A 5-meter light tube with in-vacuum Eiger 2M/1.5M detector was utilized to record the diffraction patterns located at 5.232 m downstream from the sample (Kraft, Bergamaschi et al. 2009). The field of views were varied between 8*5 and 14*12 µm^2 (h*v) per projection with an average scanning step size of 0.5-0.7 µm following a Fermat spiral trajectory (Huang, Yan et al. 2014). The scan for each sample was conducted with an angular step, varied from 1.03 to 2.22°, an angular range from 0 to 180° of the sample with respect to the incoming X-ray beam, and the scan was repeated with the resulting number of projections from 650 to 1400. The acquisition time of each scan point was 0.1/0.05 s, so that a total acquisition time, including the dead time during sample movements, for one complete tomogram varied between 3 and 12 h. The difference map algorithm refined by the maximum likelihood optimization were used to reconstruct ptychograms directly after acquisitions (Thibault, Dierolf et al. 2009, Thibault and Guizar-Sicairos 2012), where a pair of scans were recorded at different angles and positions of the detector and then combined under the same reconstruction and illumination, resulting in two different images (Holler, Diaz et al. 2014). Ptychographic reconstructions generated ptychograms with pixel sizes of 9.97-18.20 nm and the total doses for acquisition of one specimen were 9.9-116.2 x 10^6 Gy. The ptychograms then underwent corrections for zero- and first order terms and subsequent registration process along the vertical and horizontal directions (Guizar-Sicairos, Diaz et al. 2011). The tomographic reconstruction via filtered back projection was later implemented, generating tomograms with effective spatial resolutions between 12.5 and 24.5 nm via Fourier shell correlation (van Heel and Schatz 2005). Thermal treatment of the sample during PXCT measurement was carried out using an external portable furnace (Nabertherm, DE). The flOMNI pin containing the sample was transferred into the furnace and heated to desired temperature points. Afterwards, the pin was transferred back to the PXCT experiment setup.

3.2.3 Complementary ET measurement

ET measurements made use of a lamella of the pure npAu and CeO_2/npAu sample with an approximate thickness of 200 nm, produced and deposited on a lift-out grid by FIB technique. The lamella was the fresh sample extracted from the pillar before PXCT measurement. ET was conducted with the help of a Fischione tomography holder and a Titan 80-300 (FEI) microscope under an acceleration voltage of 300 kV in scanning transmission electron microscopy mode with a high-angle annular dark-field detector, at the INT at KIT (Karlsruhe, Germany). The tilt series were acquired with a range of ±60° and an increment of 2° using an Xplore3D software (ThermoFisher Scientific, USA). The alignment for tilt series was carried out using a cross-correlation function under an IMOD software (Regents, USA) and the tomographic reconstruction was then performed using a simultaneous iterative reconstruction technique under an Inspect3D software (ThermoFisher Scientific, USA), resulting in the tomogram's voxel sizes of 1.3 nm for pure npAu and 0.3 nm for CeO_2/npAu.

3.2.4 Data processing

Prior to 3D visualization, the segmentation process to distinguish between sample and air/background was carried out via Trainable Weka Segmentation 3D plugin in FIJI software. The resulting label images along with the original tomograms were then imported into an Avizo 9.7 software (ThermoFisher Scientific, USA) for volume rendering and further analysis. Default settings were applied for each data treatment module unless otherwise stated. 'Lasso' tool was used to distinguish between exterior and pores.

Pores and samples were then visualized individually in 3D via ‘Volume Rendering’ module. To obtain the values of volume (V) and surface area (S), ‘Label Analysis’ module with 3D interpretation was used. Further analysis to show pore size distribution was carried out using ‘Separate Objects’ module, followed by ‘Label Analysis’ module to calculate equivalent diameter as the ligament or pore size. Pore network models were generated using Generate Pore Network Model module from Avizo 9.7 XPoreNetworkModel Extension, where the algorithm models the actual pores with fitting spheres.

3.2.5 Numerical tomography-based simulations

Absolute permeability, molecular diffusivity, electrical and thermal conductivity simulation were done using Avizo 9.7 XLabSuite Extension software. The region of interest for simulations was determined to be a cube with 1x1x1 μm^3 from the middle of 3D-rendered volume for each sample. The parameter details, boundary conditions, and fundamental formulation used in the software are briefly elucidated as follows:

For absolute permeability simulation, Stokes equation (Eq.1) and Darcy’s law (Eq.2) along with Finite Volume method were used to compute the value of absolute permeability of the sample, “k” (μm^2), as well as to visualize the gas flow and pressure mapping profile on the pore.

$$\begin{cases} \vec{\nabla}.\vec{v} = 0 \\ \mu\nabla^2\vec{v} - \vec{\nabla}P = \vec{0} \end{cases} \quad (1)$$

Where $\vec{\nabla}.$ is divergence operator, $\vec{\nabla}$ is gradient operator, $\vec{v}$ is fluid velocity, μ is dynamic viscosity of gas, ∇^2 is Laplacian operator, and P is fluid pressure.

$$\frac{Q}{S} = -\frac{k}{\mu}\frac{\Delta P}{L} \quad (2)$$

Where Q is flow rate through pores (m^3/s), S is cross section area for fluid goes through (m^2), k is absolute permeability constant (m^2), μ is dynamic viscosity of fluid (Pa.s), ΔP is pressure difference applied around sample (Pa), L is length of sample in flow direction (m). Boundary conditions used in this simulation include no-slip condition at gas-solid interfaces, no flow on the system faces except the input and output, fluid can freely spread on the input face due to stabilization zone in the system where pressure is quasi static. The user inputs made in this case were the dynamic viscosity of 2E-05 Pa.s (air), input pressure of 1.1E+05 Pa, and output pressure of 1.0E+05 Pa. These pressure boundaries were determined on the account of the more-or-less atmospheric pressure in an external furnace or during PXCT measurement. Besides, modifying these values will not change the permeability, which is intrinsic to the porous medium, and only the outcome field will be rescaled.

For molecular diffusivity simulation, Fick’s law (Eq.3 and 4) along with Finite Volume method were used to compute the value of diffusion coefficient, “D” (m^2/s), as well as to visualize the gas diffusion profile on the pore.

$$\frac{\partial C}{\partial t} - D.\nabla^2 C = 0 \quad (3)$$

$$\vec{j} = -D.\vec{\nabla}C \quad (4)$$

Where C is concentration of solute in solvent (mol/m^3), ∇^2 is Laplacian operator, D is diffusion coefficient of solute in solvent (m^2/s), $\vec{j}$ is solute mass flux ($mol/m^2/s$). Boundary conditions used in this simulation include the presence of two reservoirs with same volume on each side of the sample, no diffusion on other faces of the system except the input and output, connection between reservoirs and samples along with diffusion starts at t_0, influence of gravity was neglected and only passive diffusion considered, no reaction occured at gas-solid interface. The user inputs made in this case were the bulk diffusion of 1.6E-05 m^2/s (CO_2 in air), input concentration of 91 mol/m^3, and output pressure of 50 mol/m^3. These values for input CO_2 concentration were determined to be the global CO_2 concentration in air of 4000 ppm and the output one was made arbitrarily since modifying them will not change the molecular diffusivity, which is intrinsic to the porous medium, and only the outcome concentration field will be rescaled.

For thermal conductivity simulation, Fourier's law (Eq. 5 and 6) along with Finite Volume method were utilized to compute the value of thermal conductivity constant, "λ" (W/m/K), as well as to visualize the temperature profile on the material.

$$\vec{\varphi} = -\lambda\vec{\nabla}\mathrm{T} \quad (5)$$

$$(\rho C_p)_\alpha \frac{\partial T_\alpha}{\partial t} - \lambda_\alpha \nabla^2 T_\alpha = 0 \quad (6)$$

Where ρ_α is density of a phase (kg/ m^3), C_{p_α} is specific heat of a phase (J/kg/K), λ_α is thermal conductivity of a phase (W/m/K), T_α is temperature of a phase (K), φ is heat flux (W/m^2), λ is thermal conductivity of material (W/m/K), $\vec{\nabla}T$ is temperature difference (K). Boundary conditions used in this simulation include constant heat flux between two opposite faces of the system, other faces are insulated, input and output fluxes are equal at equilibrium, temperature and normal component of heat flux are continuous at the interface between phases. The user inputs made in this case were the material thermal conductivity of 310 W/m/K (Au), pore thermal conductivity of 0.02587 W/m/K (O_2/He gas), input temperature of 773 K, and output temperature of 298 K. These temperature boundaries were determined arbitrarily and also due to the fact that modifying them will not change the thermal conductivity, which is intrinsic to the material, and only the outcome temperature field will be rescaled.

For electrical conductivity simulation, Ohm's law (Eq. 7 and 8) along with Finite Volume method were utilized to compute the value of electrical conductivity constant, "σ" (S/m), as well as to visualize the voltage profile on the pore.

$$j_{total} = \int_S -\sigma_{solution}\vec{\nabla}V \, . \, \overrightarrow{dS} \quad (7)$$

$$\frac{j_{total}}{S} = \sigma \frac{\Delta V}{L} \quad (8)$$

Where j_{total} is total electrical flux going through the input face (V m), $\sigma_{solution}$ is electrical conductivity of the free solution (S/m), v is electrical potential (V), S is area of the input face (m^2), ΔV is potential bias (V), L is length of material sample (m), σ is electrical conductivity of the material (S/m). Boundary conditions used in this simulation include direct current is considered, other faces are insulated, input and output fluxes are equal at equilibrium, skin effect and concentration variations are neglected. The user inputs made in this case were the solution electrical conductivity of 0.5 S/m (0.038 M KCl), input voltage of 1 V, and output voltage of 0.2 V. These electrical voltage boundaries were determined arbitrarily and the fact that modifying them will not change the thermal conductivity, which is intrinsic to the material, and only the outcome voltage field will be rescaled.

3.3 Results and Discussion

Prior to quantifying the stabilising effects of metal oxide incorporation, thermal annealing studies were firstly performed for pure npAu. The npAu sample (ca. 5 µm diameter, 5 µm height) was investigated via PXCT in ambient conditions (ca. 21 °C, ambient air) and the reconstruction results are shown in Figure 3.1. The reconstructed tomograms (with spatial resolutions of 19 nm in Figure 3.2) for the sample before and after heating at 450 °C are shown in Figure 3.1a,b, respectively. Notably, the thermal annealing effects were apparently not uniformly observed throughout the sample (Figure 3.1b,d), where several nm outside layer kept the original pore structure on the upper half of the volume, while virtually the entire lower half of the volume did not show significant annealing. This observation was made immediately on inspection of the annealed sample prior to PXCT measurement, and as a result the fields of view for the PXCT measurements between Figure 3.1a,c,e and Figure 3.1b,d,f were displaced vertically by ca. 5 µm (Figure 3.1g). This was done in order to emphasize the striking difference between the annealed and apparently stable areas in Figure 3.1d. As a result, the stabilized part of Figure 3.1b,d with smaller ligaments of npAu was previously illuminated by X-rays, whereas the annealed part was not previously illuminated by X-rays prior to heating. From Figure 3.1f, it can be observed that the maximum pore size for the annealed part could be three times bigger than the unannealed part in Figure 3.1e. Therefore, we hypothesized that the concurrence of X-ray illumination, atmospheric air, and the presence of high surface area Au sites triggered such a stabilization effect on npAu ligaments, so that the annealing process was hindered. A possible explanation can be due to the contamination by carbon and oxygen, which normally also occurs during X-ray photoelectron spectroscopy measurement (Li and Reeve 2005).

From this experiment onwards, newly-prepared samples were exposed to a continuous inert N_2 flow during PXCT measurements, so as to remove one of the variables led to such an unexpected stabilization process. Figure 3.3a,c,e show the structural difference between the whole npAu sample before and after heating at 550 °C and 750 °C, respectively, with the spatial resolutions ranging from 19 to 25 nm (Figure 3.4a-c). The partial stabilization effect observed previously during PXCT in ambient air was not present here, therefore the entire sample responded as expected to thermal annealing. As there were severely hardened parts on the exterior resulting from the FIB sample preparation, trimming to exclude them was necessary, resulting in subvolumes as in Figure 3.3b,d,f. This is necessary to verify the representation of the actual material pore structure, so the subsequent quantitative analysis generates an accurate information. From these figures, physical properties (surface area and pore volume) of npAu can be extracted as presented in Table 3, where a decrease in surface area and an increase in porosity/pore volume are noticeable at elevated temperature. Moreover, the pore size distribution before and after heating is significantly different as exhibited in Figure 3.3g, where the size range increases 6-fold from room temperature to 550 °C and 3-fold from 550 °C to 750 °C. Besides, the average pore size also increases from 63.0±12.6 at room temperature to 221.1±141.8 nm at 550 °C to 470.2±397.0 nm at 750 °C. This investigation supports the previously results, carried out *in situ* under controlled O_2/He atmosphere stating that the annealing started as low as 300 °C (Baier, Wittstock et al. 2016).

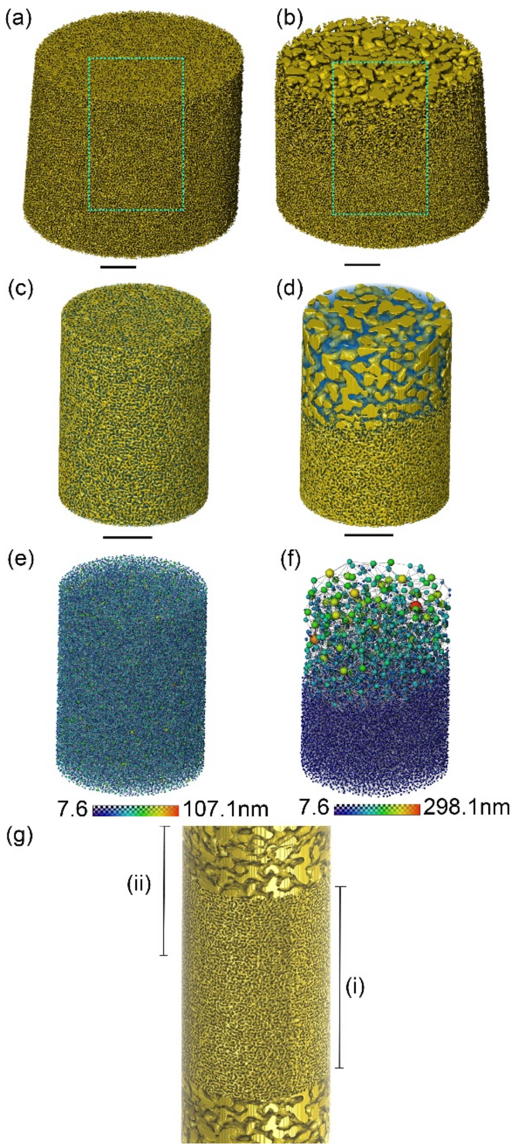

Figure 3.1: PXCT volume rendering of (a,b) full and (c,d) trimmed npAu sample with (e,f) pore network model before (a,c,e) and after (b,d,f) heating at 450 °C. The scalebars are 1 µm. (c,d) npAu is in yellow and pore in blue. (g) Illustration of field of view before (i) and after heating at 450 C (ii).

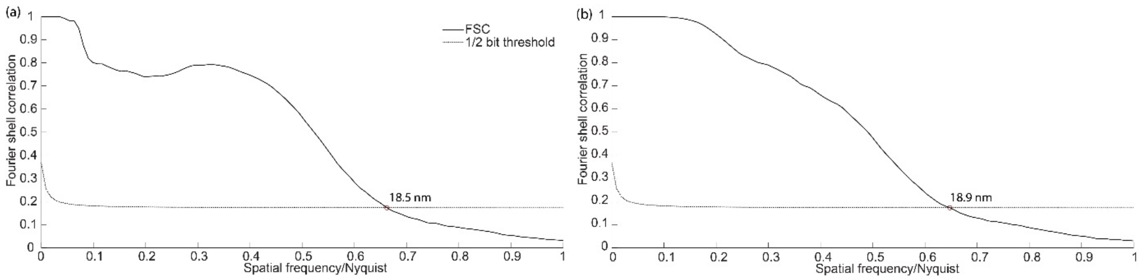

Figure 3.2: FSC for the tomograms of npAu samples before (a) and after heating at 450 °C (b) from Figure 3.1.

As a complementary measurement, ET was also carried out on a sample before heating and the result is displayed in Figure 3.5. A quantitative analysis from the volume rendering results in a surface area of 4.7 m^2/g, pore volume of 0.037 m^3/g, and porosity of 41.9%. Although the porosity is below the range reported (Wittstock, Wichmann et al. 2012), the surface area value is in agreement with the published reports (Wittstock, Wichmann et al. 2012, Shi, Schaefer et al. 2014). Besides, those values are a bit larger than the one from PXCT, but this is expected possibly due to the interference of FIB cutting. Nevertheless, the more important analysis from electron tomography is in the pore size distribution in Figure 3b, where micropores (<2 nm) could also be detected owing to its higher spatial resolution and an average pore size of 46.2±21.3 nm. This value is lower than the one from PXCT, but this is expected as PXCT is not able to detect any micropore (<2 nm) due to its limited spatial resolution.

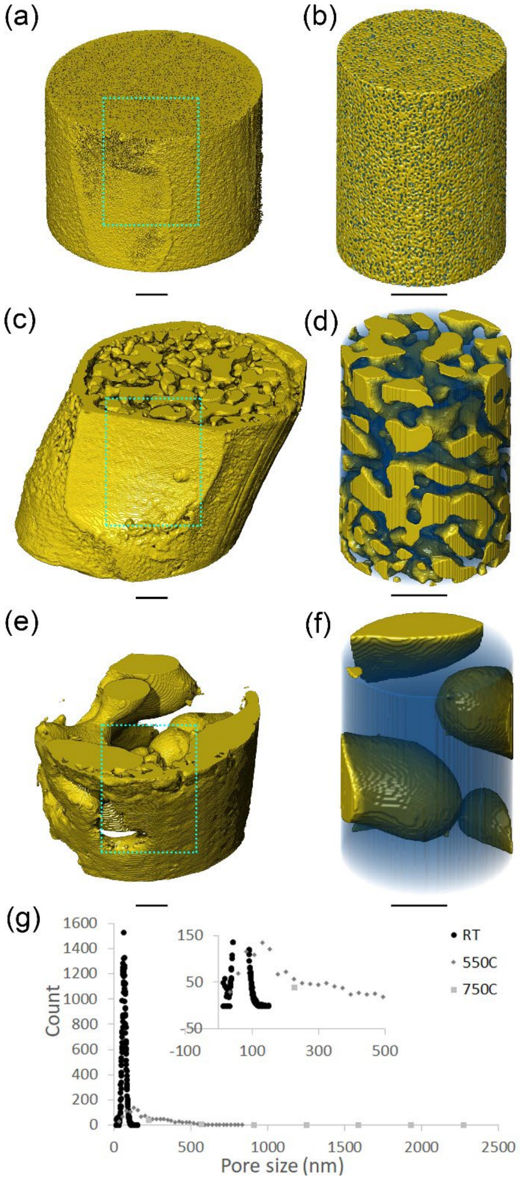

Figure 3.3: PXCT volume rendering of (a,d,g) full and (b,e,h) trimmed npAu sample with its (c,f,i) pore network model and (j) pore size distribution plot before (a-c) and after (d-f) heating at 550 °C and (g-i) 750 °C. The scalebars are 1 µm. (b,e,h) npAu is colored in yellow, whereas pore in blue.

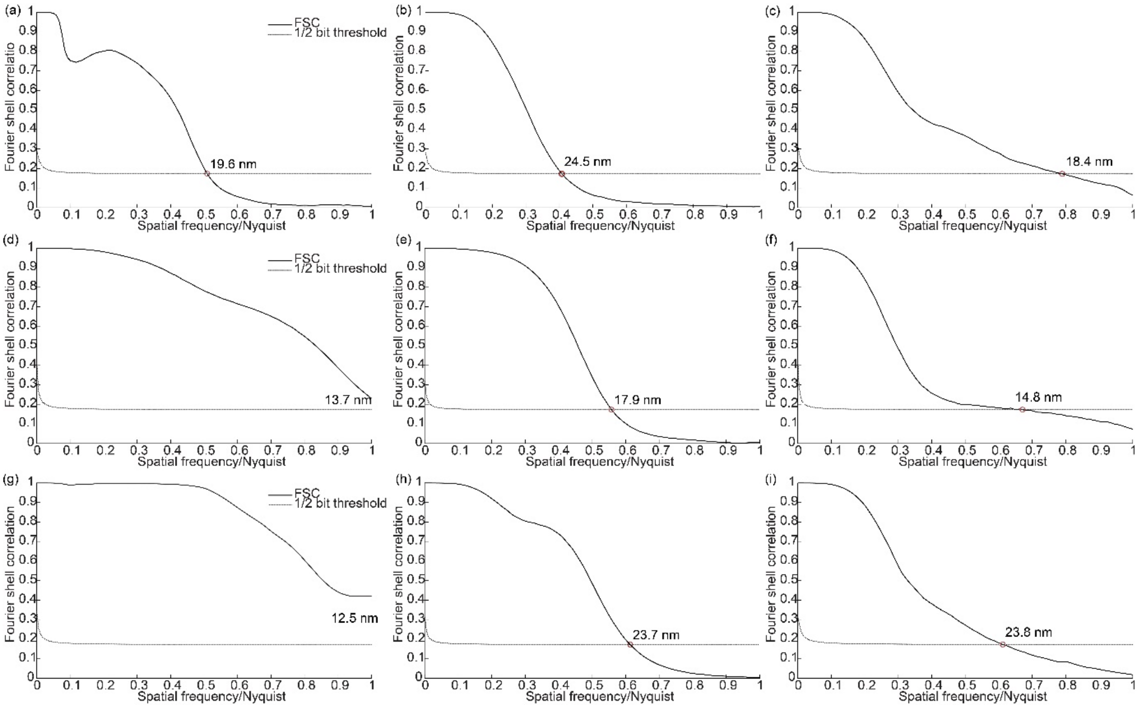

Figure 3.4: FSC for the tomograms of npAu before (a) and after heating at 550 °C (b) and 750 °C (c) in Figure 3.2; CeO_2/npAu before (d) and after heating at 550 °C (e) and 750 °C (f) in Figure 3.7; $CeTiO_x$/npAu before (g) and after heating at 550 °C (h) and 750 °C (i) in Figure 3.12.

Table 3: Physical properties derived from rendering data volumes of PXCT in Figure 3.3, 3.6, and 3.8.

Sample	T (°C)	S (m^2/g)	V_p (m^3/g)	Porosity
npAu	20	2.698	0.029	35.54%
	550	0.661	0.078	60.04%
	750	0.239	0.159	75.44%
CeO_2/ npAu	20	2.197	0.069	55.09%
	550	1.935	0.060	51.74%
	750	0.337	0.053	48.54%
$CeTiO_x$ /npAu	20	4.046	0.088	59.30%
	550	1.591	0.104	63.13%
	750	0.343	0.181	74.92%

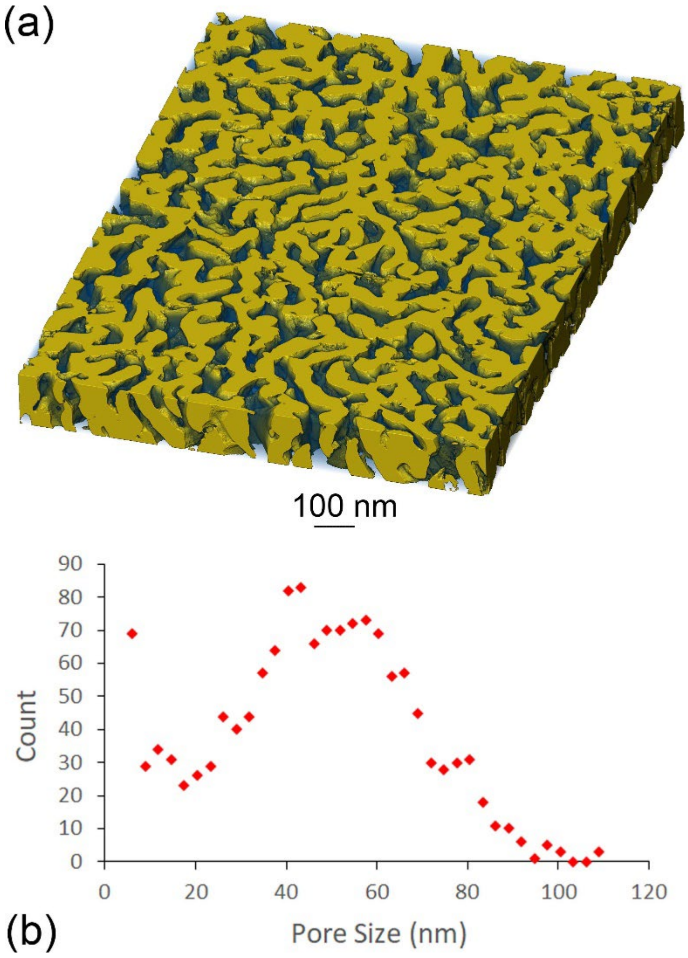

Figure 3.5: ET volume rendering (a) and (b) pore size distribution plot of npAu lamella (yellow = npAu and blue = pore) at room temperature.

Moving on to CeO_2/npAu sample, Figure 3.6a,c,e display the intact sample before and after heating at 550 °C and 750 °C, respectively. Trimming to exclude the hardened parts was also carried out, resulting in Figure 3.6b,d,f. After first heating to 550 °C, there was barely any coarsening occurred even after trimming to reveal the inside layer (Figure 3.6b,d), but a striking difference happened after second heating to 750 °C (Figure 3.6d,f), where large blobs are obviously noticeable. Quantitative analysis in Table 3 also corroborate it by showing a slight decrease in surface area after first heating, followed by a severe drop in one order of magnitude after second heating. This tendency is also strengthened by the pore distribution graph in Figure 3.6g, where the pore size shifts to lower values in mesopores (2-50 nm) after the first heating and a prominent change with more macropores, even in micrometer scales, then appeared after the second heating. Moreover, the average pore size shifts to a lower value from 149.0±59.5 nm at room temperature to 137.5±56.3 nm after first heating, then greatly elevates to 333.0±293.5 nm. The change after first heating at 550 °C is in contradiction to the pure sample, where the porosity became higher after reaching higher temperatures, but the propensity after second heating is similar. This therefore implies that there is an intriguing slowdown of coarsening around annealing temperature of 550 °C, which is corroborated by a previous report stating that the same sample could maintain the morphology up to 585 °C (Shi, Schaefer et al. 2014). Furthermore, the porosity before heating is comparable to the value reported previously (Fam, Sheppard et al. 2018).

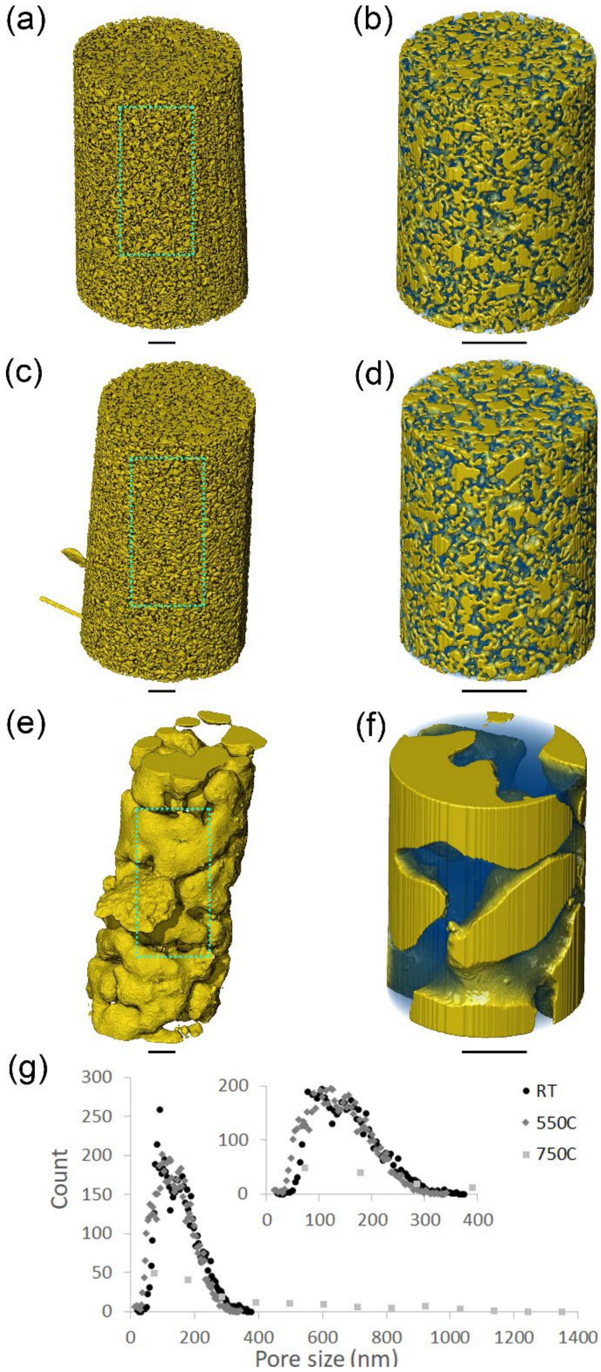

Figure 3.6: PXCT volume rendering of (a,c,e) full and (b,d,f) trimmed CeO_2/npAu sample with (g) pore distribution graph before (a,b) and after (c,d) heating at 550 °C and (e,f) 750 °C. The scalebars are 1 µm. (b,d,f) CeO_2/npAu is colored in yellow, whereas pore in blue.

ET was also carried out as a complementary measurement on a sample before heating and the result is displayed in Figure 3.7. The main purpose with this sample is to localize the distribution of CeO_2 nanoparticles over npAu as PXCT is not able to due to its limited spatial resolution. Figure 3.7a exhibits the a quite uniform distribution of non-spherical CeO_2 nanoparticles with noticeable agglomeration (Figure 3.7c) over the ligaments of npAu. It should be noted that the non-spherical 3D structure of CeO_2 via ET actually breaks the stereotype where circular nanoparticles observed under 2D imaging are usually deemed as spheres. Furthermore, a quantitative analysis from the volume rendering results in a volume fraction of 0.12 for CeO_2, which equals to 4.94 %w from this CeO_2/npAu sample and is in agreement with previously published reports (Shi, Schaefer et al. 2014, Fam, Sheppard et al. 2018). The particle size distribution plot in Figure 3.7d shows that the average particle size of CeO_2 nanoparticles is 3.37±1.56 nm where a minimum particles size of 1.50 nm and a maximum of 15.75 nm can be found.

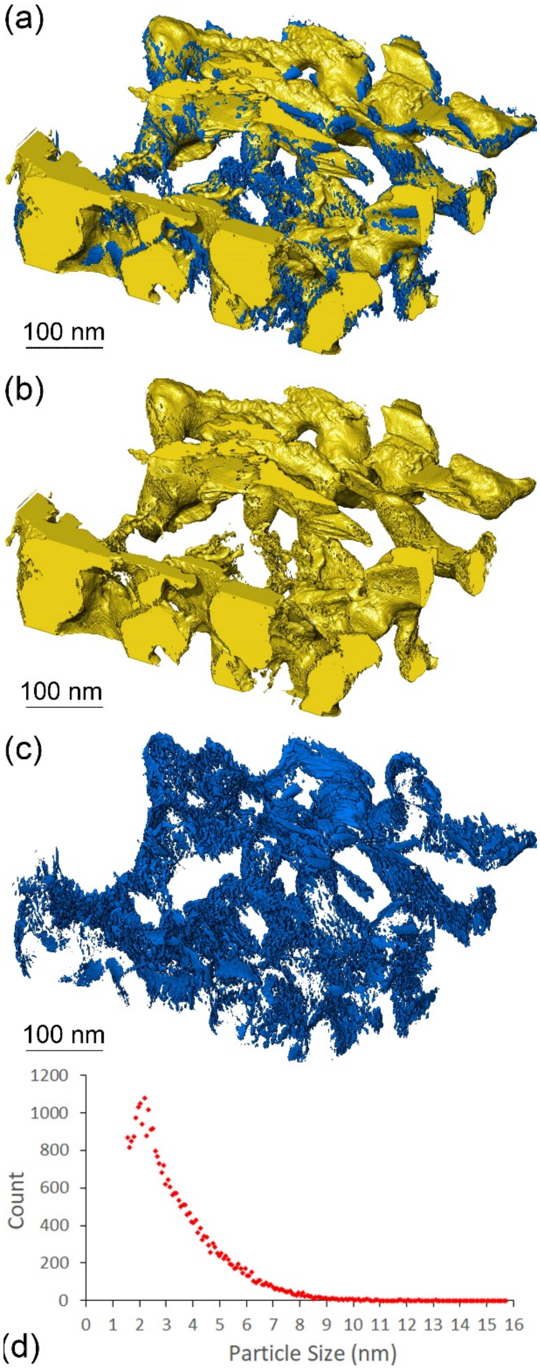

Figure 3.7: ET volume rendering of CeO_2/npAu lamella (a) at room temperature, only npAu (b), only CeO_2 particles (c) and the particle size distribution graph (d). Yellow-rendered object is npAu and blue-rendered object is CeO_2.

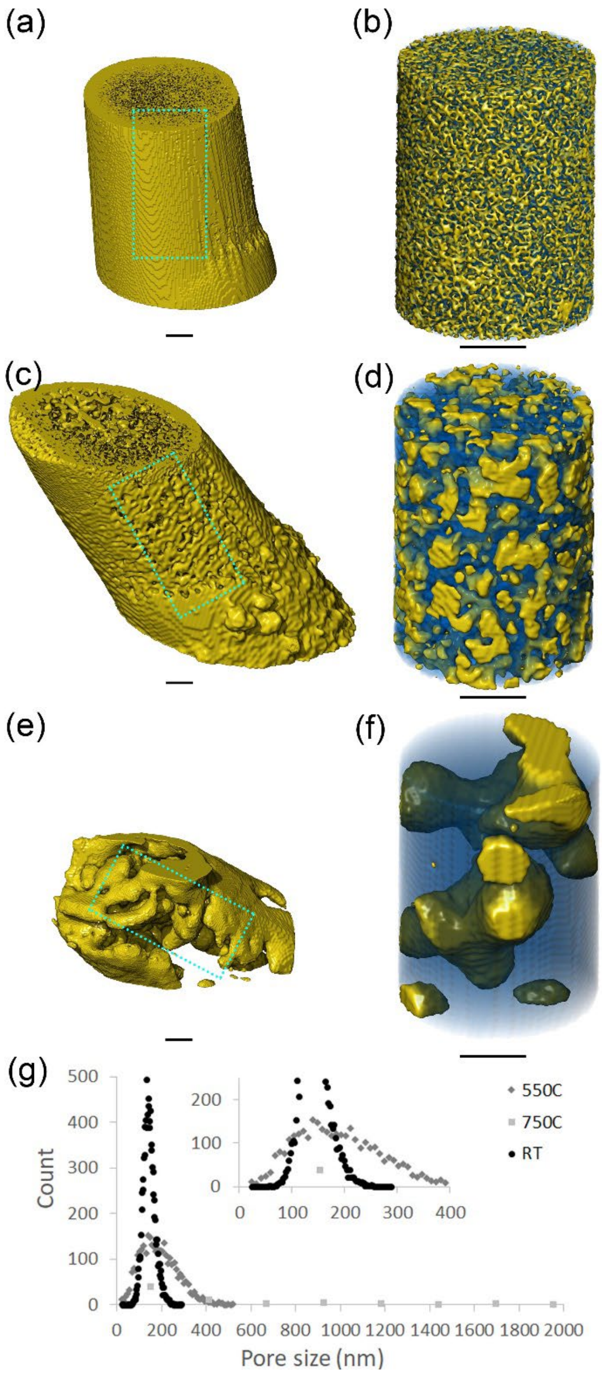

Figure 3.8: PXCT volume rendering of (a,d,g) full and (b,e,h) trimmed CeTiO$_x$/npAu sample with its (c,f,i) pore network model and (j) pore size distribution plot before (a-c) and after (d-f) heating at 550 °C and (g-i) 750 °C. The scalebar is 1 µm. (b,e,h) npAu is colored in yellow, whereas pore in blue.

Last for CeTiO$_x$/npAu sample, Figure 3.8a,c,e display the intact sample before and after heating at 550 °C and 750 °C, respectively. Trimming was again conducted to exclude the hardened layer, resulting in Figure 3.8b,d,f., where the structural change is striking after two heating steps, where the material became less dense or more pores could be observed after heating. A quantitative analysis in Table 3 corroborates such propensity by showing that the surface area decreased, but pore volume increased as the heating temperature elevated. This tendency is also strengthened by the pore distribution graph in Figure 3.8g, indicating that there was a shift to higher pore sizes between 200 and 400 nm after the first heating and then a huge shift up to 2 µm after the second heating. Furthermore, the average pore size shifts to higher values from 142.9±27.1 at room temperature to 188.5±82.2 after heating at 550 °C to 454.4 ±82.2 nm after heating at 750 °C. This sample is in accordance to the pure sample, where the porosity became smaller after reaching higher annealing temperatures. Compared to the existing report with the same sample (Shi, Mahr et al. 2017), a temperature of 450 °C under controlled CH_3OH/H_2O was claimed to barely alter the morphology. This could strengthen our results that the onset annealing temperature would be between 450 and 550 °C. Nevertheless, it should also be noted that the difference in the atmosphere would affect the onset of coarsening temperature (Shi, Mahr et al. 2017).

In comparison between the three samples, the volume rendering results basically exhibit the similar tendency, where the ligaments coarsened and pores expanded after sequential thermal treatments, except for CeO_2/npAu after the first heating, where the ligaments densified and pores shrank. In terms of surface area, the value decreases as the annealing temperature elevates for all samples. However, in terms of porosity, the value increases along with the annealing temperature, except for CeO_2/npAu sample exhibiting a decreasing trend after the first annealing, which could be due to some agglomeration of CeO_2 nanoparticles, confirmed by the higher-resolution ET measurement, over npAu generating random pore sizes. Besides, the results also conclude that 750 °C is an over-the-top temperature for structural degradation for npAu materials, whereas 550 °C is still a mild one, shown by the subtle difference in CeO_2/npAu.

Table 4: Intrinsic material properties derived from simulation of 3D-rendered data volumes in Figure 3.9-11.

Sample	T (°C)	k (µm²)	D (m²/s)	σ (S/m)	λ (W/m/K)
npAu	20	8.00E-06	1.75E-06	0.06	120.32
	550	3.51E-04	4.64E-06	0.15	75.84
	750	4.76E-04	1.10E-05	0.36	6.81
CeO_2/ npAu	20	9.60E-05	5.27E-06	0.17	30.32
	550	8.00E-05	4.91E-06	0.16	42.34
	750	7.92E-04	1.10E-05	0.36	5.02
$CeTiO_x$/ npAu	20	7.30E-05	5.65E-06	0.19	30.58
	550	2.60E-04	6.48E-06	0.21	0.22
	750	6.60E-04	8.00E-06	0.28	93.12

To further make use of the 3D data volume, simulations were carried out to map the gas flow and diffusivity through the pore, the thermal and electrical conductivity on material and the pore, as well as to compute the absolute permeability constant (k), molecular diffusivity coefficient (D), electrical conductivity constant (σ), and thermal conductivity coefficient (λ). As previously mentioned in the Experimental section that the region of interest is a cube with a size of 1x1x1 μm^3 extracted from PXCT sample, Figure

3.9a shows the model of pristine npAu before heating (opaque yellow is npAu and translucent blue is pore) for simulation. After heating at 550 °C and 750 °C, the ligaments of npAu coarsened and pores became obviously larger as shown in Figure 3.9i,q. It was then used for the absolute permeability simulation to generate the gas flow profile in Figure 3.9b and the pressure map throughout the pore in Figure 3.9c. The velocity map in Figure 3.9b depicts that air flow in a wave-like manner through the continuous pore of pristine npAu, whereas the pressure map in Figure 3.9c describes the presence of gradient in parallel with the gas flow direction. After heating, the gas velocity map in Figure 3.9j and 3.9r consequently show that air could flow faster, while the pressure map in Figure 3.9k and 3.9s exhibit less striking gradient due to such bigger pores. The electrical conductivity simulation was also performed in a situation, where potential biases of 0.2 and 1 V were applied on npAu immersed in KCl solution of 0.035 M and the voltage mapping result was exhibited in Figure 3.9d, where the presence of gradient indicates that the electrical current could pass through the material. After heating, the voltage profile in Figure 3.9l and 3.9t still exhibit the presence of gradient, which means the electrical current could flow through despite the difference depending on the pore structure. Since this simulation would also like to describe how CO_2 from air diffuse through the pore, a molecular diffusivity simulation of CO_2 gas was then included in this case. Figure 3.9e-f depicts the diffusion map of CO_2 in the pore of npAu, where CO_2 diffused gradually in a flow direction and the CO_2 concentration profile in a vertical direction is quite uniform. After heating, The CO_2 diffusion profile in Figure 3.9m-n and 3.9u-v describe faster diffusion occurred as the temperature elevated and the concentration profiles in a vertical direction become less uniform after more heating. The thermal conductivity simulation results in Figure 3.9g-h shows that the heat quickly dissipates and the gradient is quite uniform in a vertical direction. The thermal conductivity profile in Figure 3.9o-p and 3.9w-x also depict a relatively slower heat dissipation and more random gradient both in vertical and perpendicular direction. Quantitatively, the computation values in Table 4 indicate that air permeability increased, CO_2 diffusivity increased, electrical conductivity increased, and thermal conductivity coefficient decreased as the heating temperature elevates. Such tendency should be due to the generation of larger pores after heating

The same procedure was applied to investigate further temperature effect on the intrinsic material properties of CeO_2/npAu and $CeTiO_x$/npAu as shown in Figure 3.10 and 3.11. In the case of CeO_2/npAu, Figure 3.10b and 3.10j describe the velocity profiles of air, which are visually similar before and after heating at 550 °C, but it drastically turned to be less wavy after heating at 750 °C (Figure 3.10r). The pressure map in Figure 3.10c and 3.10k still exhibit a comparable gradient in parallel with the air flow direction despite the distinguishable pore shape, but figure 3.10s exhibits less striking gradient due to the expanded pores after heating at 750 °C. The electrical voltage mapping results in Figure 3.10d,l,t display a similar gradient, implying that the electrical current could pass through the material before and after heating at 550 °C and 750 °C. The diffusion map of CO_2 gas in the pore of CeO_2/npAu is shown in Figure 3.10e-f, 3.10m-n and 3.10u-v, where CO_2 diffused gradually before and after the first heating, and then faster in a flow direction after the second heating. The CO_2 concentration profile in a vertical direction before and after heating at 550 °C are quite uniform, and it became become less uniform heating at 750 °C. The thermal conductivity simulation results in Figure 3.10g-h, 3.10o-p, and 3.10w-x describe that the heat could dissipate, and it got better as the temperature increased. The gradient for both before and after heating at 550 °C are not uniform in a vertical direction, but it is relatively more uniform both in vertical and perpendicular direction after heating at 750 °C. Quantitatively, the computation values in Table 2 indicate that air permeability, CO_2 diffusivity, electrical conductivity slightly decreased and then greatly increased as the temperature heats up, whereas thermal conductivity initially increased and then significantly dropped. This behaviour should be influenced by the pore shrinkage after the first heating, followed by the sudden pore broadening after the second heating.

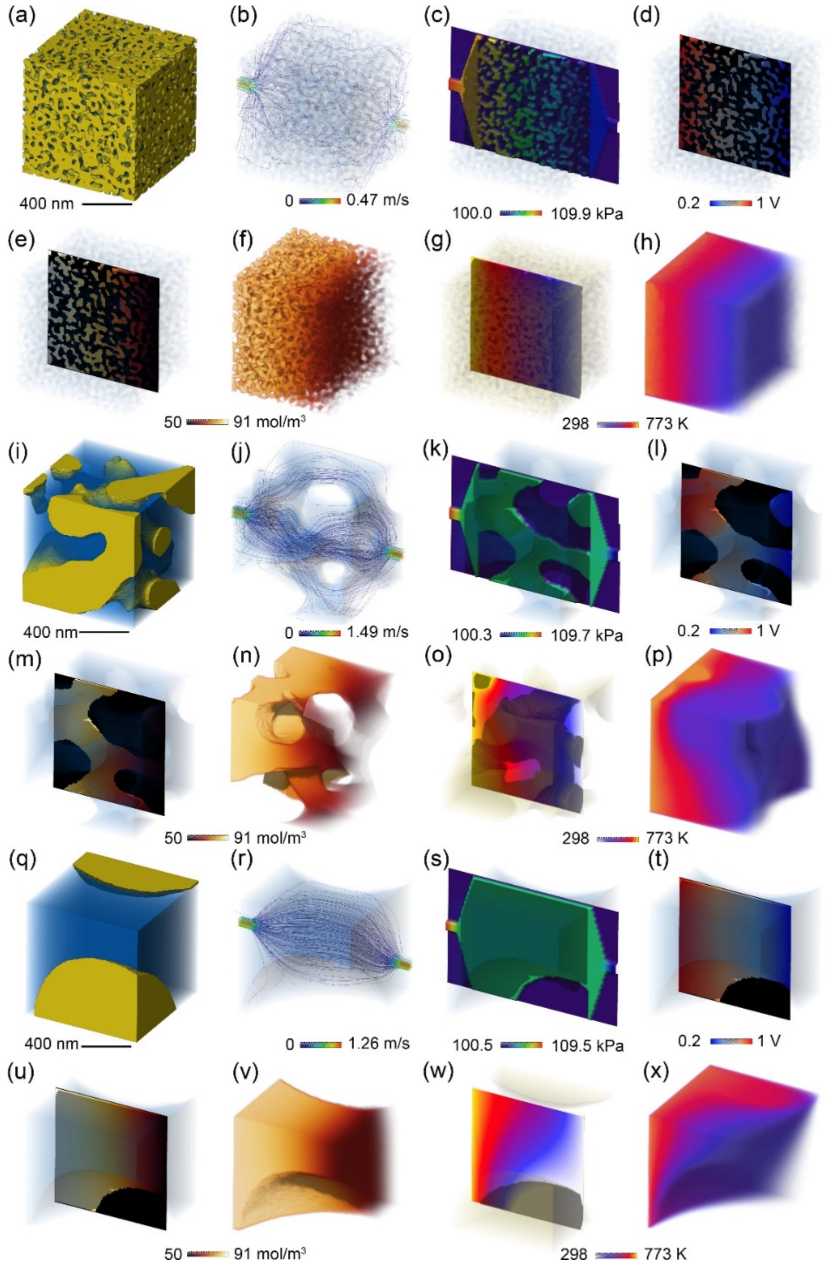

Figure 3.9: PXCT volume rendering of a block pure npAu (a, i, q), cropped from the sample in Figure 3.3b/d/f, before (a-h) and after heating at 550 °C (i-p) and 750 °C (q-x). Fluid flow profile (b,j,r), pressure mapping (c,k,s), voltage mapping (d,l,t), CO_2 concentration profile (e,m,u), and temperature mapping (g,o,w) in a slice form and whole volume (f,n,v,h,p,x) from absolute permeability (b,j,r,c,k,s), electrical conductivity (d,l,t), molecular diffusivity (e,m,u,f,n,v), and thermal conductivity (g,o,w,h,p,x) simulation through the pore (blue in a,i,q).

For $CeTiO_x$/npAu, Figure 3.11b describes the velocity profile of air, which was quite wave-like structure, throughout the pore, while the pressure map in Figure 3.11c exhibits a gradient with uniform values in the vertical direction. After heating at 550 °C and 750 °C, the gas velocity map in Figure 3.11j,r consequently show that air could flow faster and the pressure map in Figure 3.11k,s exhibit less striking gradient due to such bigger pores. The electrical voltage mapping result in Figure 3.11d displays also displays gradient, implying that the electrical current could pass through the material. After heating at

550 °C and 750 °C, the voltage profile in Figure 3.11l,t still exhibit the presence of gradient, which means the electrical current could flow through despite the difference depending on the pore structure. The diffusion map of CO_2 gas in the pore of $CeTiO_x$/npAu is shown in Figure 3.11e-f, where CO_2 diffused gradually in a flow direction and the CO_2 concentration profile in a vertical direction is quite uniform. After heating at 550 °C and 750 °C, the CO_2 diffusion profile in Figure 3.11m-n and 3.11u-v describe faster diffusion occurred as the temperature elevated and the concentration profiles in a vertical direction become less uniform after more heating. The thermal conductivity simulation results in Figure 3.11g-h describe that the heat could dissipate well even though the gradient is not uniform in a vertical direction. After heating at 550 °C and 750 °C, the thermal conductivity profile in Figure 3.11o-p and 3.11w-x depict a relatively slower heat dissipation and more random gradient both in vertical and air flow direction after the first heating, whereas it then shows a quicker heat dissipation and more uniform gradient after the second heating. Quantitatively, the computation values in Table 4 indicate that air permeability, the CO_2 diffusivity, the electrical conductivity increased as the temperature increased, while the thermal conductivity firstly decreased and then made a jump. Such tendency should be due to the larger pore after heating, similar to the what the pure sample endured.

Further into the simulation results, the values of air permeability, CO_2 diffusivity coefficient, and electrical conductivity for npAu and $CeTiO_x$/npAu samples increased along with the elevated annealing temperatures. However, CeO_2/npAu sample again exhibited a unique trend, where those values slightly decreased after the first heating, but then increased after the second heating. Since those simulations were conducted on the pores, such a unique tendency should be due to the unexpected porosity shrinkage of CeO_2/npAu, which could be due to the agglomeration of CeO_2 nanoparticles as previously explained. On the other hand, thermal conductivity for each sample has its own disposition before and after thermal treatment. The values went down for npAu as the temperatures went up, while it firstly inclined and then jumped down for CeO_2/npAu, whereas it initially fell down and later rose up for $CeTiO_x$/npAu. Aside from the fact that thermal conductivity simulation was performed on both the material and pores, such random behaviours (especially for the doped samples) can also partly be induced by the addition of metal oxides. Nevertheless, the strong dependency of npAu porosity on the values of electrical and thermal conductivity has been reported, where larger pores induce higher electrical conductivity but less thermal conductivity (Mishra, Bansal et al. 2008, Xia, Wang et al. 2010). The pure npAu sample in this case corroborates such tendency and even with the addition of temperature variable, where the electrical conductivity increases and thermal conductivity decreases as the temperature elevates. Last for the simulation package itself, i.e. Avizo Xlab Extenstion Suite, it is a voxel-based simulation method utilizing voxels as the volume elements, which is an advantage over having to generate a new meshed volume as in the mesh-based simulation methods, e.g. computational fluid dynamics. Although the software package is relatively new, the computational outcomes are comparable to other methods (Cooper, Kishimoto et al. 2013) and several studies have been carried out in the field of electrochemistry (Cooper, Kishimoto et al. 2013, Delattre, Amin et al. 2018, Tan, Kok et al. 2019).

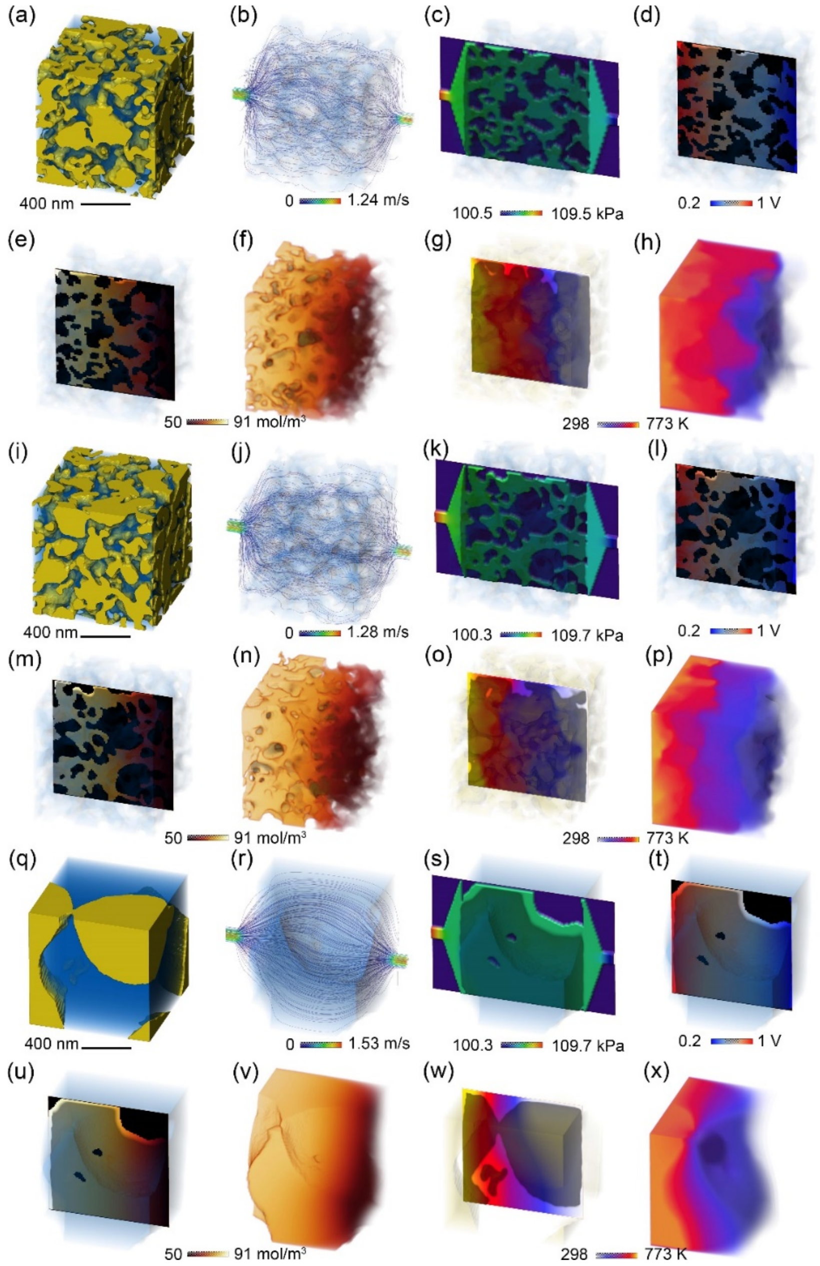

Figure 3.10: PXCT volume rendering of a block CeO_2/npAu (a, i, q), cropped from the sample in Figure 3.6b/d/f, before (a-h) and after heating at 550 °C (i-p) and 750 °C (q-x). Fluid flow profile (b,j,r), pressure mapping (c,k,s), voltage mapping (d,l,t), CO_2 concentration profile (e,m,u), and temperature mapping (g,o,w) in a slice form and whole volume (f,n,v,h,p,x) from absolute permeability (b,j,r,c,k,s), electrical conductivity (d,l,t), molecular diffusivity (e,m,u,f,n,v), and thermal conductivity (g,o,w,h,p,x) simulation through the pore (blue in a,i,q).

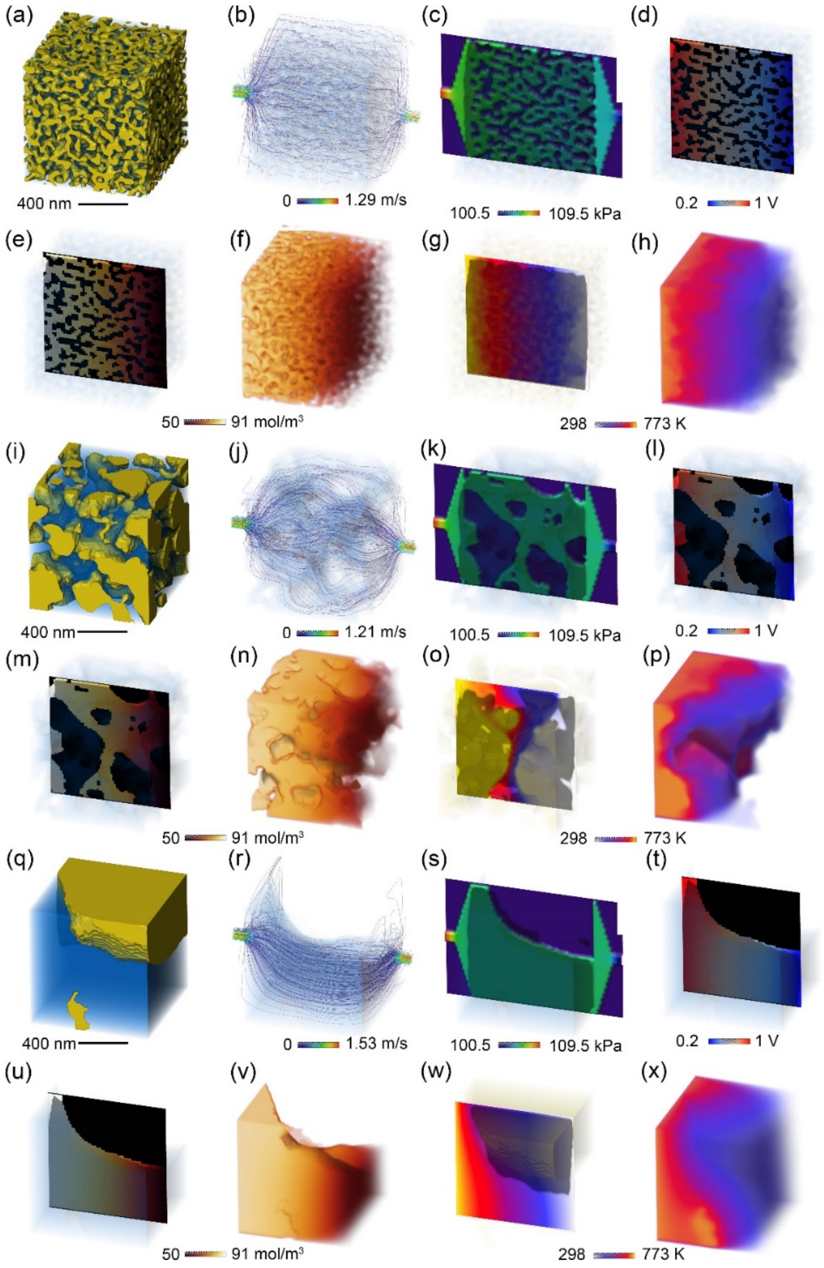

Figure 3.11: PXCT volume rendering of a block $CeTiO_x$/npAu (a, i, q), cropped from the sample in Figure 3.8b/d/f, before (a-h) and after heating at 550 °C (i-p) and 750 °C (q-x). Fluid flow profile (b,j,r), pressure mapping (c,k,s), voltage mapping (d,l,t), CO_2 concentration profile (e,m,u), and temperature mapping (g,o,w) in a slice form and whole volume (f,n,v,h,p,x) from absolute permeability (b,j,r,c,k,s), electrical conductivity (d,l,t), molecular diffusivity (e,m,u,f,n,v), and thermal conductivity (g,o,w,h,p,x) simulation through the pore (blue in a,i,q).

3.4 Conclusions

PXCT measurements were conducted to not only visualize the 3D morphology of npAu materials after thermal annealing in an external furnace, but also to calculate their surface areas and analyse the porosity. The sequential thermal treatment generally results in the pore expansion and ligament coarsening, which consequently induce the reduction of surface area and increase of pore volume. ET measurement is proved to be a useful complementary technique to probe smaller pores, particularly micropores, and dopant nanoparticles beyond the capability of PXCT. Another versatility of performing PXCT is the direct utilization of the results for simulations. In this case, simulations regarding absolute permeability of air, molecular diffusivity of CO_2 from air, electrical and thermal conductivity of npAu materials were carried out to reveal their intrinsic physical properties before and after thermal treatment, which were previously impossible with only the direct quantification from the 3D volume data. In the future, a full *in situ* PXCT experiment, followed by simulations, will be extremely useful for similar or more advanced experiments, such as catalysis, gas storage and sensing, or electrochemical reactions. A proper leak-proof reactor is therefore needed to avoid contamination, such as the aforementioned one, where strange stabilization process occurred. The study would essentially allow a precise determination of the onset of annealing temperature while being able to visualize the morphology in 3D, directly quantify the structural parameters, and subsequently use for simulation to reveal the intrinsic properties.

4 *In situ* 2D/3D imaging studies of functional materials[1,2]

4.1 Background

This chapter eventually focuses on the aim of the dissertation in developing the tool for *in situ* imaging of functional materials. The idea stems from the needs to unravel the role of catalysts while improving their performance and stability, which are critical in heterogeneous catalytic studies and usually achieved by deriving their structure-activity relationships. Since catalytic reactions commonly occur under particular working conditions, the structures of catalysts also evolve either in macro, micro-, nano-, or even atomic scale, which are sometimes not present under atmospheric environment. Terms, e.g. *in situ* and *operando* (under working conditions, with simultaneous acquisition of catalytic activity for the latter) were then specifically derived for such purposes (Grunwaldt and Clausen 2002, Weckhuysen 2002, Topsøe 2003, Bañares 2005). One of the best methods to probe the structure dynamics of catalysts is using spatially-resolved imaging techniques, e.g. X-ray or electron microscopy or both (Beale, Jacques et al. 2010, Frenkel and Van Bokhoven 2014) when a comprehension of the catalyst structure is needed at different length scales (Weckhuysen 2009, Beale, Jacques et al. 2010, Grunwaldt, Wagner et al. 2013). While electron and soft X-ray microscopy offer superior spatial resolutions (de Smit, Swart et al. 2008, Thomas and Hernandez-Garrido 2009), hard X-ray microscopy is more suitable technique for *in situ* studies on catalysts with bigger-sized samples (up to mm) under higher working atmospheres (>1 bar) (Grunwaldt and Schroer 2010, Buurmans and Weckhuysen 2012). Meanwhile, focusing optics for hard X-ray are progressively developed, so that the spatial resolutions have become comparable to the ones from soft X-ray (Yan, Conley et al. 2014, Huang, Conley et al. 2015, Cesar da Silva, Pacureanu et al. 2017, Schroer, Seyrich et al. 2017, Seiboth, Schropp et al. 2017). So far, the main hard X-ray imaging technique able to make a momentous discovery in terms of spatial resolution is XRP (Vila-Comamala, Diaz et al. 2011, Schropp, Hoppe et al. 2012). Although it has often been applied *ex situ* in various purposes (Thibault, Dierolf et al. 2008, Hoppe, Reinhardt et al. 2013, Piazza, Weinhausen et al. 2014, Zhu, Harder et al. 2015, Wise, Weker et al. 2016, Sala, Kuppili et al. 2018), its *in situ* mode under controlled temperatures and gas environments has not been explored enough, except a couple of pioneering works (Høydalsvik, Bø Fløystad et al. 2014, Van Riessen, Rickard et al. 2017) and some from our group (Baier, Damsgaard et al. 2016, Baier, Wittstock et al. 2016, Baier, Damsgaard et al. 2017, Fam, Sheppard et al. 2019).

The first *in situ* XRP study was conducted on lithium zirconate for CO_2 capture application, resulting in a spatial resolution of 200 nm (Høydalsvik, Bø Fløystad et al. 2014), even though a non-fully closed gas-filled compartment was employed. Another group simultaneously exploited *in situ* XRP and X-ray fluorescence

---

[1] The text and figures are partly adapted with permission from Ref: Fam, Y., T. L. Sheppard, J. Becher, D. Scherhaufer, H. Lambach, S. Kulkarni, T. F. Keller, A. Wittstock, F. Wittwer, M. Seyrich, D. Brueckner, M. Kahnt, A. Schropp, A. Stierle, C. G. Schroer and J.-D. Grunwaldt (2019). "A versatile nanoreactor for complementary in situ X-ray and electron microscopy studies in catalysis and materials science." J. Synchrotron Radiat., **26**: 1769-1781. Copyright © 2019 Published by IUCr.

[2] The text and figures are partly taken from a manuscript under preparation by Fam, Y., T. L. Sheppard, J. Becher, T. Scherer, P. Marek, A. Diaz, J. Ihli, M. Odstrcil, M. Holler, S. Kulkarni, T. Keller, A. Wittstock, F. Wittwer, M. Seyrich, D. Brueckner, M. Kahnt, A. Schropp, A. Stierle. C. G. Schroer, J.-D. Grunwaldt., "*Thermal stability study and simulation of nanoporous golds under particular atmosphere via X-ray microscopy* ".

(XRF) nanospectroscopy to monitor morphological changes and elemental distribution during thermal curing of geopolymers on sub-micrometer length scale despite unavailable description of the reactor (Van Riessen, Rickard et al. 2017). On the other hand, a design and application of closed *in situ* XRP cell were reported in our previous works, studying the morphological changes of colloidal Au nanoparticles and npAu materials during thermal treatment under inert and oxidizing atmospheres with spatial resolutions down to 20 nm (Baier, Damsgaard et al. 2016, Baier, Wittstock et al. 2016). The cell was also later utilized to investigate the stability of $CuO/ZnO/Al_2O_3$-ZSM-5 core-shell material under reducing and oxidizing conditions, resulting in the spatial resolution of 30 nm (Baier, Damsgaard et al. 2017). This cell (Baier, Damsgaard et al. 2016) also interestingly offers a feature to be able to do complementary electron microscopy on the same areas, but it also possesses some limitations, including a relatively high mass, large internal volume, indirect control of heating via infrared thermography, and incapability to do simultaneous XRF or product analysis for *operando* studies. Thus, upgrade and optimization of the cell in terms of dimension, mechanical stability, and heating control are imperative.

In addition, an extended implementation for XRP to generate 3D volume data based on tomographic process, i.e. PXCT, has also been capturing interest in the past decade (Dierolf, Menzel et al. 2010, da Silva, Mader et al. 2015, Ihli, Jacob et al. 2017, Fam, Sheppard et al. 2018, Ihli, Diaz et al. 2018, Li, Ihli et al. 2019) because more information can be revealed than the 2D images from XRP. For example, PXCT is able to measure and map the pore networks (da Silva, Mader et al. 2015, Fam, Sheppard et al. 2018, Li, Ihli et al. 2019) as well as to localize elemental distributions within catalyst support (Ihli, Jacob et al. 2017, Ihli, Diaz et al. 2018). However, there has not been any *in situ* PXCT works (as of this writing) mainly due to the fact that the experimental requirement is more complicated than for XRP. Here, two improved *in situ* cells are presented for complementary XRP and XRF measurements using synchrotron radiation. The setup enables high resolution 2D imaging for one (2G) cell and 3D imaging for the other (3G cell) with limited rotational angles under controlled temperature up to 1573 K and gas environments up to 1 bar. Related sample models for the feasibility studies were the colloidal Au nanoparticles (AuNP) and npAu for *in situ* XRP using 2G cell, while zeolite (ZSM5) particle was used to test the rotational angles of 3G cell and cobalt-manganese-oxides hollow sphere ($CoMnO_2$-HS) was utilized for *in situ* limited-angle PXCT using 3G cell.

4.2 Experimental

4.2.1 Sample preparation and mounting

Four sample types have been used for both cells: colloidal Au nanoparticles (AuNP), nanoporous Au (npAu), zeolite (ZSM5) particle, and cobalt-manganese-oxides hollow sphere ($CoMnO_2$-HS) particle. AuNP was purchased from (Sigma-Aldrich Chemie GmbH (Taufkirchen, DE) and used as received; np-Au (pure-, CeO_2-, and TiO_2-incorporated) samples were prepared by dealloying of an Ag-Au alloy in nitric acid (65 wt%), followed by wet impregnation with metal-oxide precursor solutions using the methods as previously published (Shi, Schaefer et al. 2014, Shi, Mahr et al. 2016, Shi, Mahr et al. 2017, Lackmann, Bäumer et al. 2018); ZSM5 particles were synthesized by a templating method using silica and alumina precursors, followed by steam assisted crystallization to form macropores within the crystals, as described in previous works (Machoke, Beltrán et al. 2015, Schwieger, Machoke et al. 2016); $CoMnO_2$-HS particles were synthesized by a hard template and microemulsion method using cobalt and manganese precursors, as previously reported (Gröger, Kind et al. 2010).

Regarding sample mounting onto the MEMS chips, AuNP was deposited just by drop-casting 0.1 ml of the colloidal solution directly on the back of the MEMS chip; ZSM5 and CoMnO$_2$-HS particles were deposited using a micro-manipulator of FIB on the hole of the MEMS chip and glued by Pt gas injection system. For npAu, a complex and long procedure was involved and performed using dual beam FIB-SEM microscope (SCIOS, FEI, US) at DESY NanoLab (Stierle, Keller et al. 2016) as shown in Figure 4.1-4. The original sample was a solid pellet, a piece of which was deposited on a SEM stub and then on a lift-out grid, which acted as an intermediate stage to the final sample holder, i.e. MEMS chip (Figure 4.1). For details in each stage after mounting the stub, the piece was cut again and shaped into a smaller block / trapezoidal prism (Figure 4.2). The block was then transferred onto the lift-out grid, where a smaller wedge shape was eventually obtained (Figure 4.3). Last, the final transfer onto the MEMS-chip was made on the spiral center area of the chip and glued with Pt on the corner to stabilize the position (Figure 4.4), which result in Figure 4.5.

Complementary TEM, energy dispersive X-ray spectroscopy (EDX), and selected area electron diffraction (SAED) measurements were performed using a Wildfire sample holder (DENSsolutions, Delft, NL), on a Titan 80-300 (FEI) microscope operated at an acceleration voltage of 300 kV in STEM and TEM mode, at the Institute of Nanotechnology (KIT, DE).

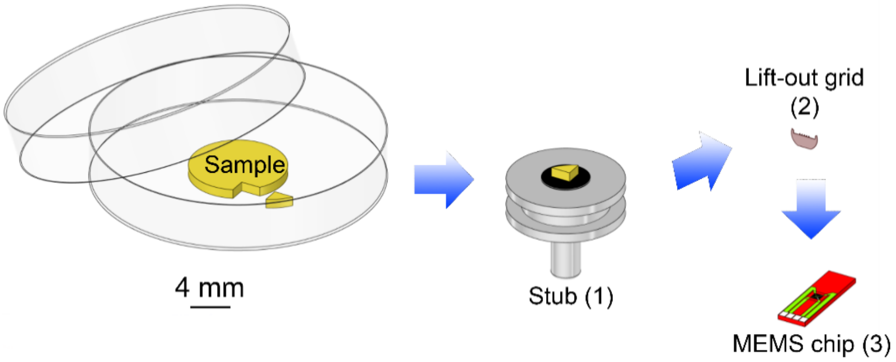

Figure 4.1: Overview of npAu sample preparation on the MEMS chip via FIB (Fam, Sheppard et al. 2019).

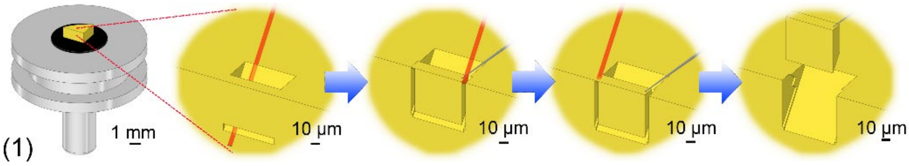

Figure 4.2: Initial npAu extraction on a SEM stub to make a block for several samples (Fam, Sheppard et al. 2019).

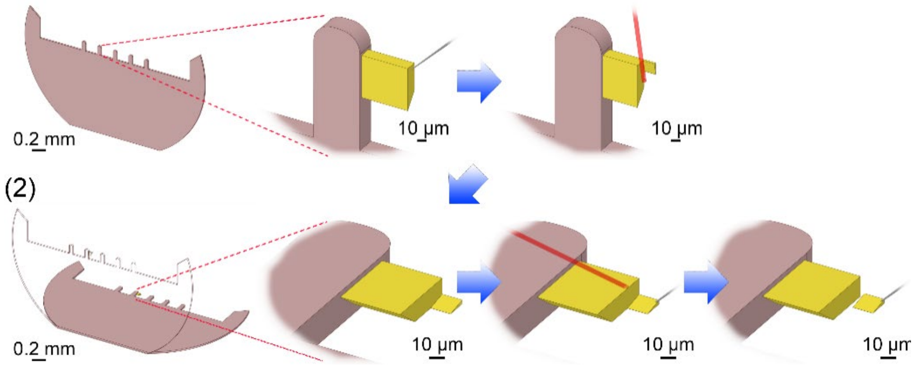

Figure 4.3: Final cut after transfer to intermediate lift-out grid and thinning of block into a wedge (Fam, Sheppard et al. 2019).

Figure 4.4: Transfer and deposition of the wedge on the MEMS chip (Fam, Sheppard et al. 2019).

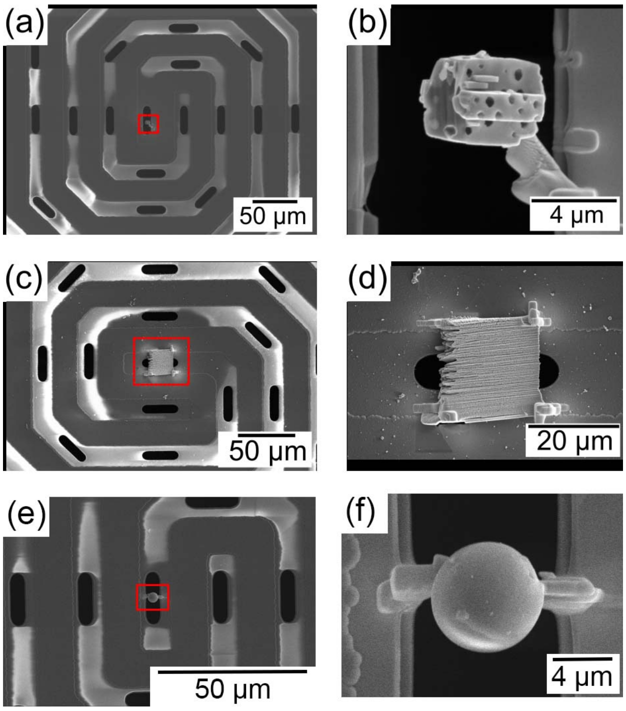

Figure 4.5: SEM images obtained during FIB preparation on Wildfire chips at DESY NanoLab: (a) ZSM5 crystal and (b) zoom in of the highlighted area; (c) npAu wedge and (d) zoom in of the highlighted area; (e) CoMnO$_2$-HS crystal and (f) zoom in of the highlighted area (Fam, Sheppard et al. 2019).

4.2.2 *In situ* XRP and PXCT studies

All experiments were performed at the nanofocus endstation of beamline P06 at the PETRA III synchrotron radiation source (Hamburg, DE) using the measurement parameters shown in Table 1. The resulting scattering signals were captured using an EIGER X 4M detector (DECTRIS Ltd, Switzerland) with 75 x 75 µm^2 pixel size and 2070 x 2167 pixels. For other equipment details in Figure 4.6, pure He and O_2/He gas with a specific inlet flow of 1 ml/min adjusted by a mass flow controller were used to maintain a controlled atmosphere during *in situ* annealing treatment. The temperature was controlled and monitored using customized Labview software. Specific temperature conditions applied during imaging are indicated next to the relevant figures in the Case Studies section. The outlet flow from the cell was analyzed online using a Thermostar quadrupole mass spectrometer (Pfeiffer Vacuum GmbH, Aßlar, DE) to confirm the desired atmospheric composition was present during *in situ* experiments. In this case, He and residual O_2 (m/z = 4, 32) were monitored for the inert and oxidizing atmosphere.

Table 5: Experimental parameters during XRP studies at P06 beamline of PETRA III (Fam, Sheppard et al. 2019).

Sample Type	AuNP	npAu	Zeolite	$CoMnO_2$-HS
Energy (keV)	15.0	9.0	9.0	9.0
Sample to detector distance (mm)	4160	2310	3470	3470
Sample focus distance (mm)	in focus	in focus	0.6	0.4
Field of view (µm^2)	2.5 x 2.5	5 x 5; 20 x 20	4 x 4	6 x 6
Exposure time (ms)	50	10; 5	500	500
Scantime per image (min)	4-5	3-5	5-6	5-6
Beam size on the sample (nm)	60	60	2000^b	2000^b
Scan step size (nm)	40	100	333	500
Scan type	Grid jitter	Continuous	Grid jitter	Grid jitter
Optics	NFL^c	FZP^a	FZP^a	FZP^a

^{a}Fresnel zone plates, ^{b}out of focus, ^{c}Nano-focusing lenses

For measurement of ZSM5 and $CoMnO_2$-HS samples by limited angle PXCT, the sample on a Wildfire chip was placed within the 3G cell and aligned to the center of rotation with respect to the beam. 2D ptychographic projections were recorded across an angular range of approximately ±35°. The sample was scanned in a raster grid manner with each scan point randomly offset in both scanning directions by up to 50% of the step size, known as grid jitter mode.

During measurement of the AuNP and some npAu samples, XRF signal was collected with a single channel Vortex silicon drift detector at 50 nm intervals with a collection time of 50 ms/pixel. The detector was placed on a moveable table and was located at an angle approximately 72° to the incident beam. It should be noted that the cell body blocks positioning of the detector ideally perpendicular to the incident beam. An XRF scan in high flux mode was recorded by scanning the sample over a field of view of 5x5 and 15×15 μm^2 with a step size of 50 nm. At each scanning position an XRF spectrum was collected for an exposure time of 2 s. The XRF spectra were fitted by AXIL software for the analysis of line intensities of the elements.

4.2.3 Gas flow simulation of 2G/3G cells

In ANSYS AIM (Student Version, ANSYS, Inc.), Fluid Flow template module was used to simulate the gas flow in the 2G and 3G cell (Figure 4.7). Specific parameters were kept as default unless specifically mentioned. The geometry was generated by the integrated Space Claim Direct Modeler and “Define mesh manually” was chosen. In Fluid-specific options, “Swirling flow” was ticked to enable any significant rotating or twisting movement of the gas. The simulation focus was set as “Steady-state fluid flow”. Number of fluid regions was selected to be “1”, i.e. Air as the Material Sample, and “Compressible flow (ideal gas)” was ticked as an additional flow physics. For the meshing process settings, the resolution was set to 4, “Fluid flow or fluid-solid heat transfer” was selected for Engineering intent, and the refinement mechanism of “Curvature and proximity” was used. In Mesh controls, the element shape was set to “Automatic”, where it meshed sweepable bodies with hexahedrons and provided a tetrahedral mesh on bodies that were not sweepable. The number of generated nodes was 46556 for 2G cell and 95272 for 3G cell, respectively.

For the Physics parameters, the whole SDCM-generated volume was specified as the location of Physics Regions. “Laminar” flow model was selected as the Flow Model since a Reynolds number (Re) of 9 was estimated according to: $Re = \frac{\rho * v * D_H}{\mu}$, where ρ is the mass density of air (1.1839 kg m^{-3} at T = 298 K), v is the mean velocity of air (0.236 m s^{-1} in this case from a volumetric flow of 1 ml min^{-1}), D_H is the hydraulic diameter of the inlet/outlet channel (0.3 mm), and μ is the dynamic viscosity of air (18.6 µPa s). The Inlet/Outlet Boundary was located on either one cross-section face of the long cylindrical channels with “Mixed” subsonic-supersonic regime and Gauge static pressure of 0 Pa. Additional parameter settings were for the inlet with gas Velocity magnitude of 0.236 m s^{-1} and Temperature of 298 K. The rest of the faces on the SDCM-generated volume was determined as the Wall Boundary. The Solver Options was left as default, where the solution would converge with Residual Tolerance of 1E-05 and Maximum iteration number of 1000; Solution advancement exponent was kept 0 under Calculation Control; and “Least squares cell-based” Gradient method was used for Discretization Control with “Second-order upwind” Advection and “Automatic” Pressure scheme. As the results, the convergence criteria were met after 45 iterations with residual tolerances up to 9.69E-06 for 2G cell, and 773 iterations with residual tolerances up to 2.15E-07 for 3G cell. The fluid flow profiles of the 2G and 3G cell are displayed in Figure 4.8.

4.2.4 Data processing

The algorithm used for ptychographic reconstruction was based on the (e)PIE algorithm (Maiden and Rodenburg 2009). Cropping the diffraction patterns to 256×256 pixels led to a pixel size of 8.2 nm (for np-Au), and 8.5 nm (for zeolite) in the reconstructed images. To estimate the spatial resolution, a Fourier ring correlation (FRC) analysis (van Heel and Schatz 2005) was performed. Correlation was always performed on 2D projections (ring correlation), as opposed to 3D volumes (shell correlation). As a common procedure, two individual successive scans of an identical sample area were reconstructed and compared. First the images were cropped to exclude the edges of the field of view, phase wedges were removed and the images were aligned on a sub-pixel level using the “scipy” Python package (Guizar-Sicairos, Thurman et al. 2008). Before correlating the phase reconstruction, a Kaiser-Bessel window function with a size equal to 1 was applied to the images, in order to reduce artifacts caused by erroneous high frequencies resulting from the edges of the limited field of view of the reconstructions. The ptychographic reconstructions were done automatically using the computers at P06 beamline.

Tomographic reconstruction of the ptychographic projection series for the ZSM5 and CoMnO$_2$-HS samples were performed as follows. The reconstructed phase projections were first cropped to only include the sample area present within the window of the MEMS chip. Secondly phase wedges and offsets were removed from the projections, using the regions right next to the sample as the zero-reference point. The third step was to align all projections to each other in the vertical direction (along the rotation axis) by correlating the derivative of their vertical profiles (Guizar-Sicairos, Diaz et al. 2011). Step four was the horizontal alignment (in the tomographic plane) by aligning the horizontal center of mass of all projections. This placed the rotation axis into the center of mass of the particle. The obtained sinogram was reconstructed using multiple tomography algorithms for ZSM5 sample, including: (i) simultaneous iterative reconstruction technique (SIRT) from the “TomoJ” package (Messaoudii, Boudier et al. 2007), as implemented in FIJI software (Schindelin, Arganda-Carreras et al. 2012), (ii) simultaneous algebraic reconstruction technique (SART) (Andersen and Kak 1984), as part of the Python package “scikit-image” (van der Walt, Schönberger et al. 2014), (iii) maximum-likelihood expectation maximization (MLEM) algorithm using in-house code based on the literature (Bruyant 2002), (iv) an in-house deep learning code in development at beamline P06 of PETRA III for analysis of limited angle tomography data (in preparation).

4.3 Cell Design and Simulation

Both cells were particularly built for the hard X-ray nanoprobe endstation at P06 beamline, PETRA III synchrotron radiation source (Hamburg, DE) with the following purposes: (i) 2G cell for high-resolution *in situ* XRP in 2D, with complementary XRF and/or large angle X-ray diffraction; (ii) 3G cell for limited-angle *in situ* PXCT in 3D as well as XRP in 2D. Such interchangeable condition therefore makes them easily replaceable by each other into the same setup in Figure 4.6. The other equipment for *in situ* setup includes: (i) a ‘Digiheater’ temperature controller box (DENSsolutions, Delft, NL), printed electrical contacts to interface with the MEMS chip and software for accurate control of heating parameters, (ii) mass flow controllers (Bronkhorst High-Tech B.V., Ruurlo, NL) for accurate control of gas environment, (iii) a mass spectrometer (Thermostar, Pfeiffer Vacuum GmbH, Aßlar, DE) connected to the reactor outlet for gas analysis. The cell stands on the beamline stage with a goniometer for rotation alignment and lateral piezomotors for nanopositioning. A ‘Wildfire’ MEMS chip (DENSsolutions, Delft, NL), enclosed within the cell, contains the sample, which is deposited on a spiral-shaped area in the middle. Depending on the sample state (colloidal or solid) and so the type of MEMS chip, the sample area may or may not include a silicon nitride (Si$_3$N$_4$) membrane. The sample area also contains a spiral layer of tungsten for heating purpose with an operational temperature range up to 1300 °C with through-hole chips or 1100 °C with Si$_3$N$_4$ membranes. As the MEMS chips are originally developed for *in situ* TEM, both cells provide an additional feature for a complementary *ex situ* TEM before and after *in situ* XRP or PXCT, by merely replacing the chips into a Wildfire TEM holder (DENSsolutions, Delft, NL).

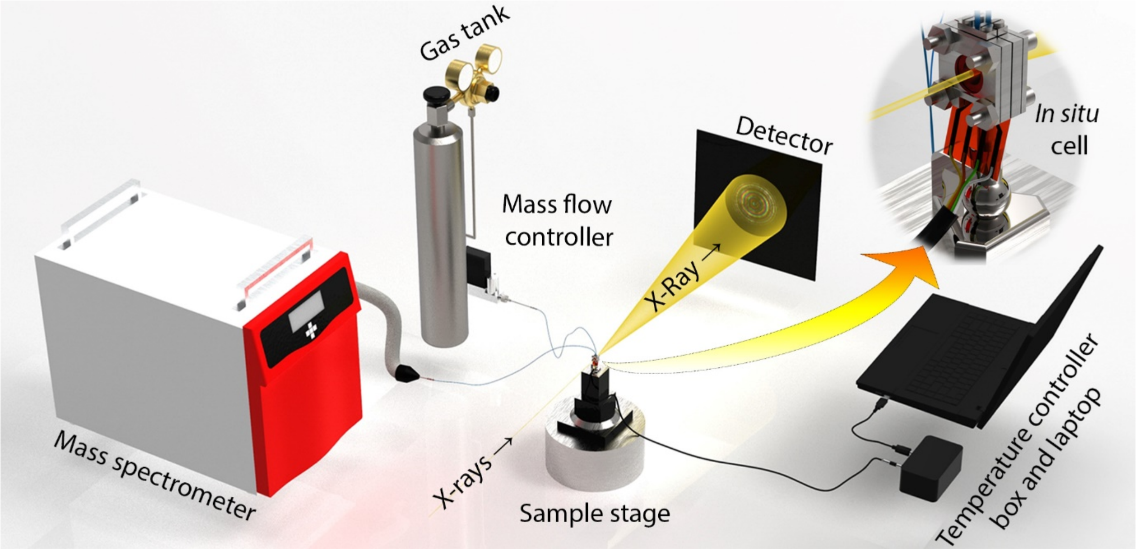

Figure 4.6: Illustration of the *in situ* setup for 2D and 3D ptychography at the P06 nanoprobe endstation of PETRA III.

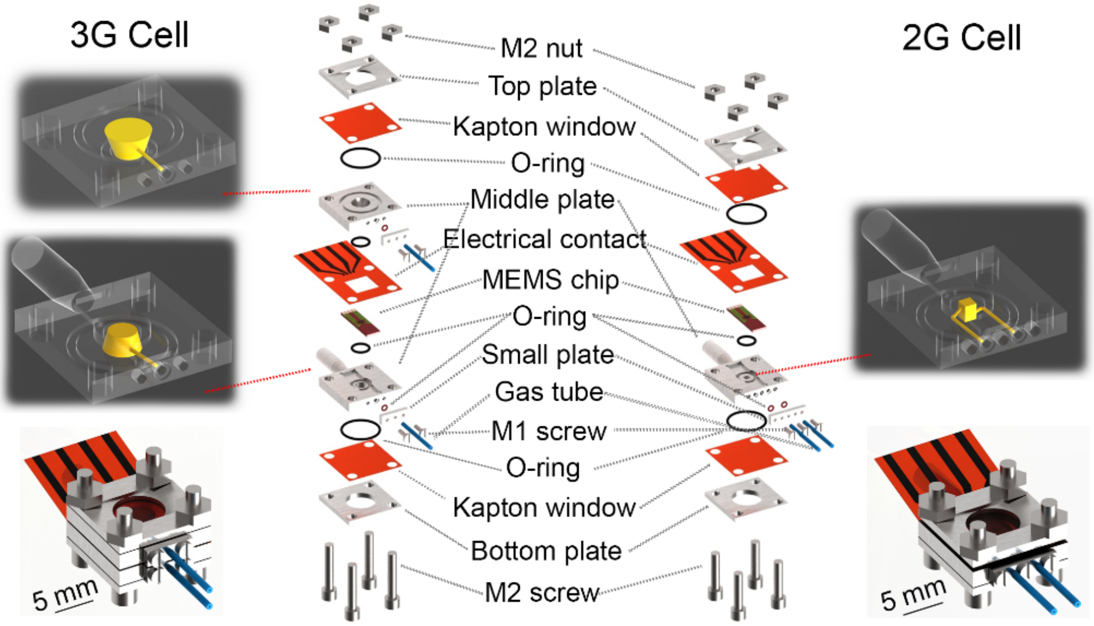

Figure 4.7: Illustration of disassembled 2G (right) and 3G (left) cell with their internal gas-flow volumes (highlighted above). The fully assembled setups are shown below (Fam, Sheppard et al. 2019).

Figure 4.7 describes in detail the configurations of both cells; whose top and bottom plates are the sealing bodies for the middle plate(s) with the help of O-rings and Kapton films. Small plates on the side of the middle plates, containing the MEMS chip, aim to seal the inlet/outlet tubes. The other similarities between both cells include: (i) the electrical contact, which is a printed circuit (Au and galvanic layers on Kapton film as the base) and has to be placed on top of the MEMS chip, where the alignment of contact pads between them is essential, so an electrical current can flow from the temperature controller box as the power supply to the MEMS chip, where the electrical current is converted into heat based on the Joule-heating principle; (ii) the O-ring below the MEMS chip for sealing purpose of the cell.

Aside from similarity, some differences are noticeable in how and when either 2G or 3G cell should be used. The 2G cell has only one middle plate, where Si_3N_4 membrane MEMS chips have to be used to contain the sample deposited on the back. The presence of membrane on the chips makes 2G cell particularly suitable for colloidal samples, size-selected clusters or unsupported specimens requiring stable supports. Figure 4.8-left shows that the internal volume of 2G cell is 2.6 µL and the gas flows in a U-shaped manner within the single middle plate. Meanwhile for 3G cell, two middle plates are present, where each one contains either the inlet or outlet channel for the gas flow. Due to this configuration, through-hole MEMS chips have to be utilized to contain the sample deposited on either one of the through holes, making 3G cell specifically eligible for solid samples only and a complicated sample preparation procedure via FIB technique is then required. Figure 4.8-right indicates that the internal volume of 3G cell is 24.5 µL and the gas flows from the one internal body of the middle plate, then through the holes of the MEMS chip, and finally to the outlet port of internal body of the other middle plate. Another distinguishable usage between both cells is about the cell mounting, where 2G cell is only positioned perpendicular to the incoming beam and 3G cell is allowed to have a range of rotational angles of ±35° around the rotation center with respect to the beam (or ±65° for the naked MEMS chip). Nevertheless, those differences actually serve as a flexibility indicator of the setup at the hard X-ray nanoprobe endstation of beamline P06 for diverse sample requirements from the prospective users.

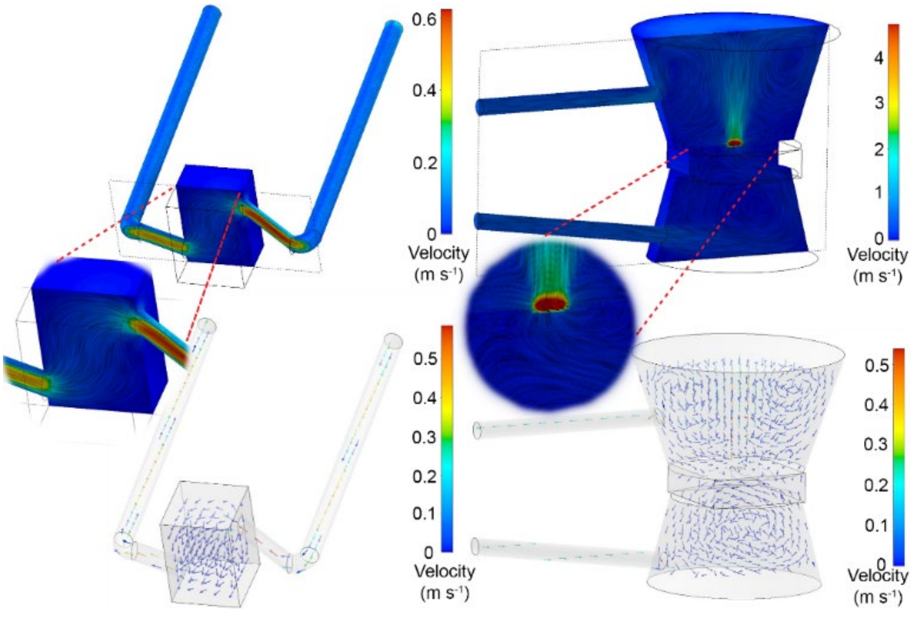

Figure 4.8: Internal gas-flow volume and simulation of 2G cell (left) and 3G cell (right) (Fam, Sheppard et al. 2019).

Regarding the requirement of sample dimensions, the maximum area can reach up to 0.5 x 0.5 mm^2, equivalent to the heating zone, but the maximum thickness should not be more than 1 mm since it takes some time to attain a uniform heating of the sample in the z-axis. Nevertheless, thermal conductivity of the probed material is undoubtedly the main parameter determining the uniform heating of the sample. With respect to the available sample preparation methods, there are several methods can be considered, such as the conventional abrasion, grinding, or sieving, followed by polishing process since many samples, especially technical catalysts, possess dimensions up to mm scale. In addition, the micromanipulation techniques using FIB, He-ion microscope, or Ar ion milling are sometimes mandatory to accurately turn the sample into a specific shape and then to correctly deposit the sample on the heating zone of the MEMS chips. Despite the similarity to TEM sample preparation procedure, it should be noted that the time and effort are still significantly less as the required sample dimensions greatly exceeds the ones of TEM owing to the higher penetration depth of hard X-rays.

In comparison to the first generation *in situ* XRP (1G) cell developed by our group (Baier, Damsgaard et al. 2016), the following improvements were made for 2G and 3G cells:

- Wider ranges for compatible sample types, i.e. colloidal particles, bulk and single solid particles.
- Lower ratio of internal cell volume to external body volume, necessitating longer contact time between reactant gases and samples potentially enabling to detect gaseous products during imaging measurements using mass spectrometry for *operando* studies;
- Lower mass of the cell bodies, increasing stability and resistance to vibrations, which is crucial in nano-precision of positioning motors;
- Capability to simultaneously conduct complementary XRF or large-angle X-ray diffraction (XRD) or both. As XRP does not ensure that its elemental speciation via resonant imaging around an elemental absorption edge (Hoppe, Reinhardt et al. 2013) always works on any material, complementary elemental analysis from XRP and/or even crystallinity analysis from XRD are definitely useful;
- Capability to carry out 3D imaging studies despite the limitation in rotational angles;
- Direct and precise temperature control and feedback system (Figure 4.9) even under different gas atmospheres thanks to the 4-point resistivity measurement and well-calibrated specific resistivity in this type of MEMS chips as they have also been applied for the *in situ* Wildfire TEM heating holder (Gocyla, Kuehl et al. 2018, Ren, Tang et al. 2018).

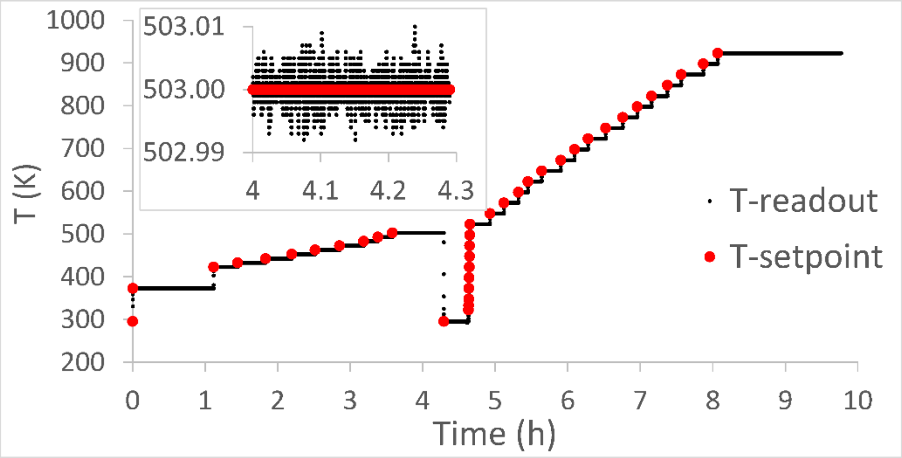

Figure 4.9: Plot of temperature readout vs time via the integrated temperature control system, recorded during thermal annealing study of npAu sample. The valley between the fourth and fifth hour of the measurement resulted from pausing the experiment due to loss of beam (Fam, Sheppard et al. 2019).

4.4 Case Studies

4.4.1 *In situ* sintering of Au colloids – early cell prototypes using 2G cell

This study probed AuNP with a particle size of 50 nm using early prototype of 2G cell in order to verify the workability of the cell for simultaneous *in situ* XRP and XRF. At this time, the investigation was carried out with the same setup configuration in Figure 4.6, but without the temperature controller box and laptop, which were replaced by a variable voltage power supply and an IR thermographic camera as previously used (Baier, Damsgaard et al. 2016). The top-row images in Figure 4.10 indicate that AuNP could be clearly observed with dark intensity implies the presence of AuNP, which also means that the resulting spatial resolution should at least be 50 nm. Such a prediction was then confirmed by FRC method calculating the spatial resolution to be 45 nm as shown in Figure 4.11. Moreover, the localization of AuNP can be more precisely conducted using XRF as shown in the bottom-row images of Figure 4.10, where higher fluorescence signals means higher concentration of AuNP. In terms of dispersibility, this sample exhibited a non-uniform distribution between larger particles possibly from agglomeration and the smaller ones around the upper middle area in Figure 4.10a-b.

During thermal treatment, AuNP experienced a gradual sintering phenomenon, where individual small particles recombined into larger clusters starting at 423 K along with the consequent disappearance of other smaller particles in the nearby region to the other bigger clusters. This kind of behaviour is expected as the particles were unsupported and the organic surfactant used to stabilize the particles from aggregation, started to decompose as the temperature elevated. At 773 K, a strange occurrence could be seen, where a sudden disappearance of AuNP happened in a great amount. This could be induced by the instability of unsupported AuNP deposited on the Si_3N_4 membrane of the MEMS chip and the dislocation of AuNP occurred after accumulated heating at 773 K. However, this occurrence could also be caused by the unstable heating control system via power supply and IR thermographic camera since the wires connected to the power supply were directly soldered to the electrical contact, so there was a possibility that significant temperature spikes took place during the measurement, which also happened in our previous work using 1G cell (Baier, Damsgaard et al. 2016). Thus, it is of high importance to employ a robust and reliable temperature control system, which was established for the setup shown in Figure 4.6 and 4.7.

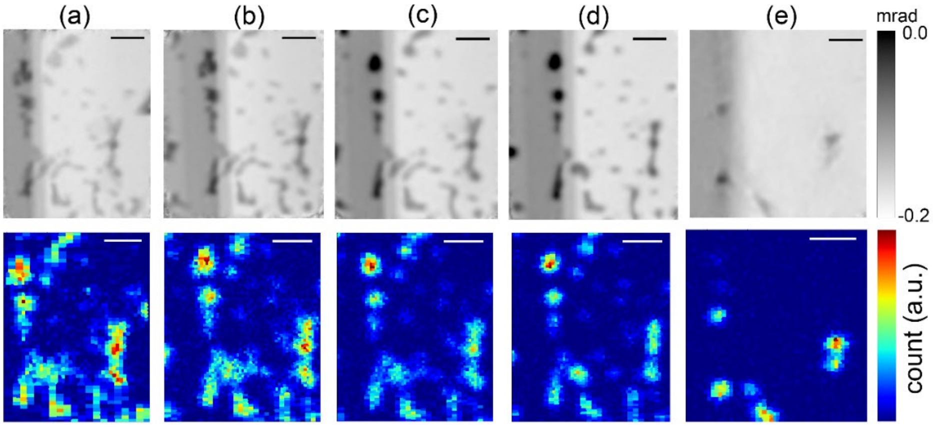

Figure 4.10: XRP images (top) and Au fluorescence maps (bottom) during thermal annealing of colloidal Au: (a) room temperature (293 K), (b) 423 K, (c) 573 K, (d) 723 K, and (e) 773 K. Dark spots in phase maps and high-count zones in fluorescence maps indicate areas most rich in Au. Scale bars = 500 nm (Fam, Sheppard et al. 2019).

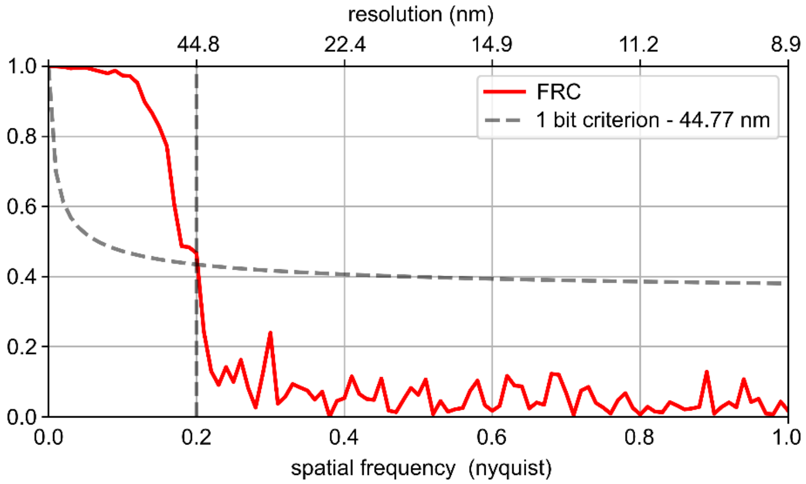

Figure 4.11: FRC of the ptychogram of AuNP (Fam, Sheppard et al. 2019).

4.4.2 *In situ* annealing of npAu materials in controlled gas environment using 2G cell

In order to demonstrate the full capability of 2G/3G cells and the corresponding infrastructure as shown in Figure 4.6 and 4.7, npAu materials were used due to its multiscalar feature and previous high spatial resolution resulted from *ex situ* PXCT measurement (Fam, Sheppard et al. 2018). The *in situ* studies began with pure npAu as the model and the results in Figure 4.12 exhibit its thermal stability under inert atmosphere up to 650 °C, which then started to show the coarsening process in terms of ligament collapse and became worse along with time. In comparison to our previous results using an older type of in situ cell (Baier, Wittstock et al. 2016), a much earlier temperature onset was observed at 300 °C, but this is undoubtedly expected due to its oxidizing environment under O_2/He, whereas our work was performed under He. This therefore implies that an inert atmosphere delays coarsening process of npAu.

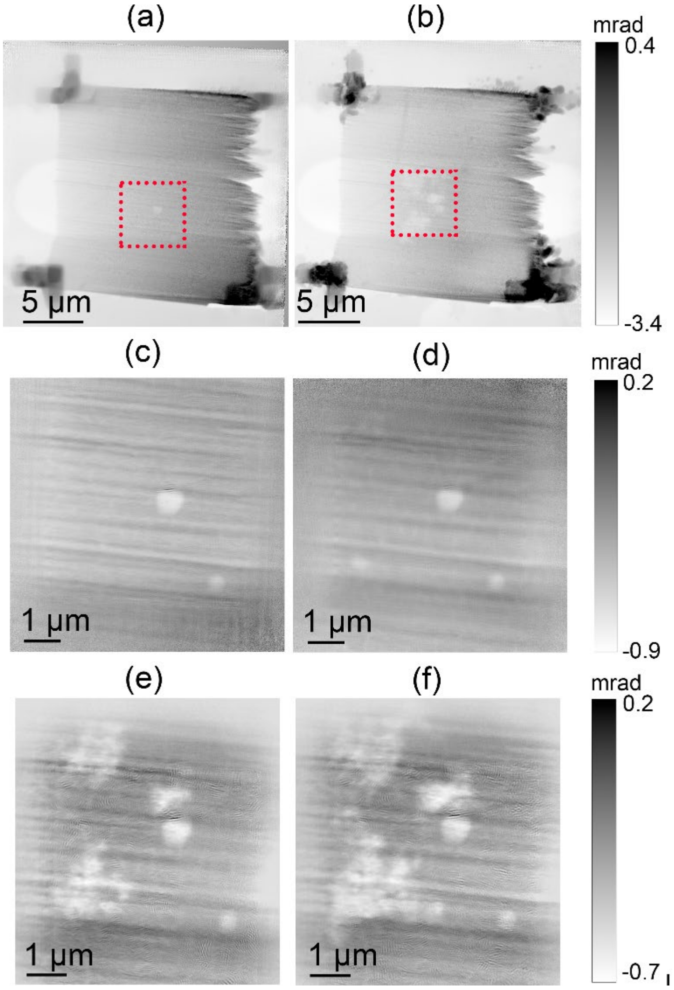

Figure 4.12: Ptychography images from thermal annealing of np-Au under He environment. Overview scans: (a) before and (b) after thermal annealing. Highlighted area in (a-b) shown: (c) at 293 K, (d) 923 K after 0 min, (e) 923 K after 15 min, (f) 923 K after 30 min. Darker intensity in phase maps indicates areas rich in Au, while brighter voids indicate annealing and absence of Au ligaments. Pt glue from FIB is visible as intense features in the corners of (a-b) (Fam, Sheppard et al. 2019).

TEM measurements on the thinner part of npAu wedge were also conducted before and after *in situ* XRP to approve the complementary benefit of using 2G/3G cells. Figure 4.13 exhibits that the morphological difference of npAu before (Figure 4.13a-b) and after (Figure 4.13c-d) annealing at 923 K is predictably discernible (Baier, Damsgaard et al. 2016, Baier, Wittstock et al. 2016), where the ligaments in Figure 4.13c-d are amalgamated and denser from the darker intensity. Besides, it should be noticed that there was unexpectedly a layer covering the sample, which was apparently confirmed to be somehow Si layer using EDX analysis in Figure 4.14 and the quantification analysis result in Table 2. Such Si layer should originate from the SiN layer on the MEMS chip since EDX-TEM works in transmission mode, so the sample should have not been the only one analysed. Moreover, the layer was still present even after thermal treatment as shown in the high resolution TEM image in Figure 4.5(h) although it became thinner probably due to the influence of high temperature. Another strange phenomenon was the presence of small nano-particles over the surface of np-Au, which was turned out to be Pt from the FIB cutting procedure as characterized by EDX in Figure 4.5d and the quantification analysis result in Table S1, although not evenly distributed on all the sample. Furthermore, high resolution TEM measurement was carried out to confirm the crystallinity of fresh np-Au, which was then proved to be crystalline owing to the existence of Au lattice spacing as shown in Figure 4.15. As a corroborative analysis, selected area electron diffraction measurement was also performed and Figure 4.16 reaffirms the presence of lattice spacing of Au with a value of 0.234 nm. This TEM study thus proves the importance of the setup to be able to conduct complementary techniques between X-ray and electron microscopy on the sample across multiple length scales from micro- to even sub-nanometer.

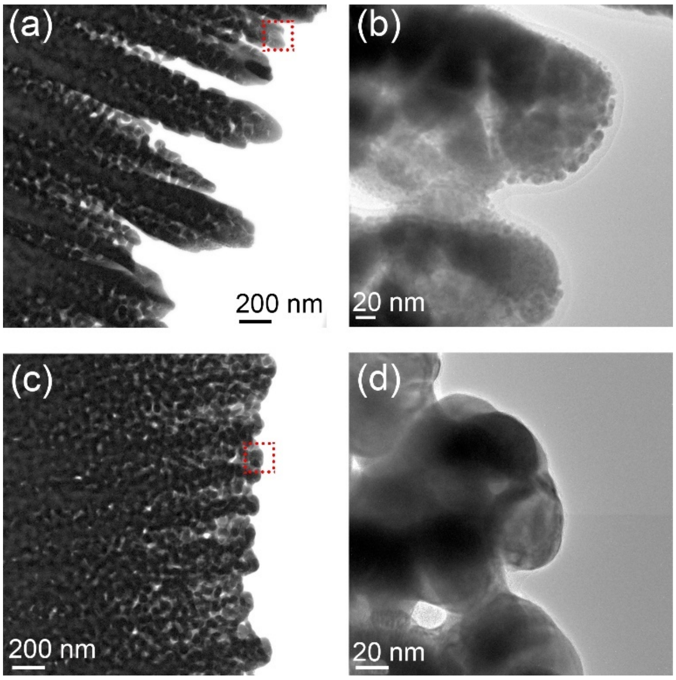

Figure 4.13: TEM images of np-Au: (a) before *in situ* thermal annealing and (b) zoom in on the highlighted area; (c) after *in situ* thermal annealing at 923 K and (d) zoom in on the highlighted area (Fam, Sheppard et al. 2019).

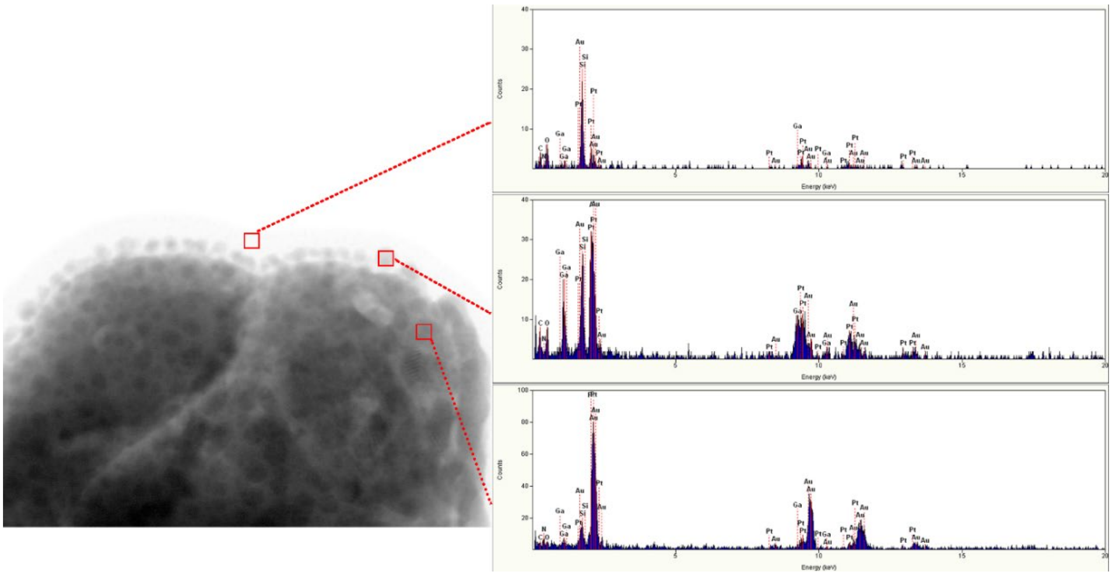

Figure 4.14: TEM-EDX data recorded on the nanoporous gold sample used for *in situ* ptychography. Analysis shows the presence of minor Si and Pt contaminants close to the Au ligament edges (Fam, Sheppard et al. 2019).

Table 6: Quantification of EDX spectra in Figure 4.14 (Fam, Sheppard et al. 2019).

Element	Atomic %		
	Area 1	Area 2	Area 3
C	6.2	29.6	29.1
N	6.9	0.0	3.9
O	5.2	13.1	14.2
Si	21.3	32.0	52.7
Ga	0.1	12.1	0.0
Pt	0.0	10.6	0.0
Au	60.2	2.6	0.0

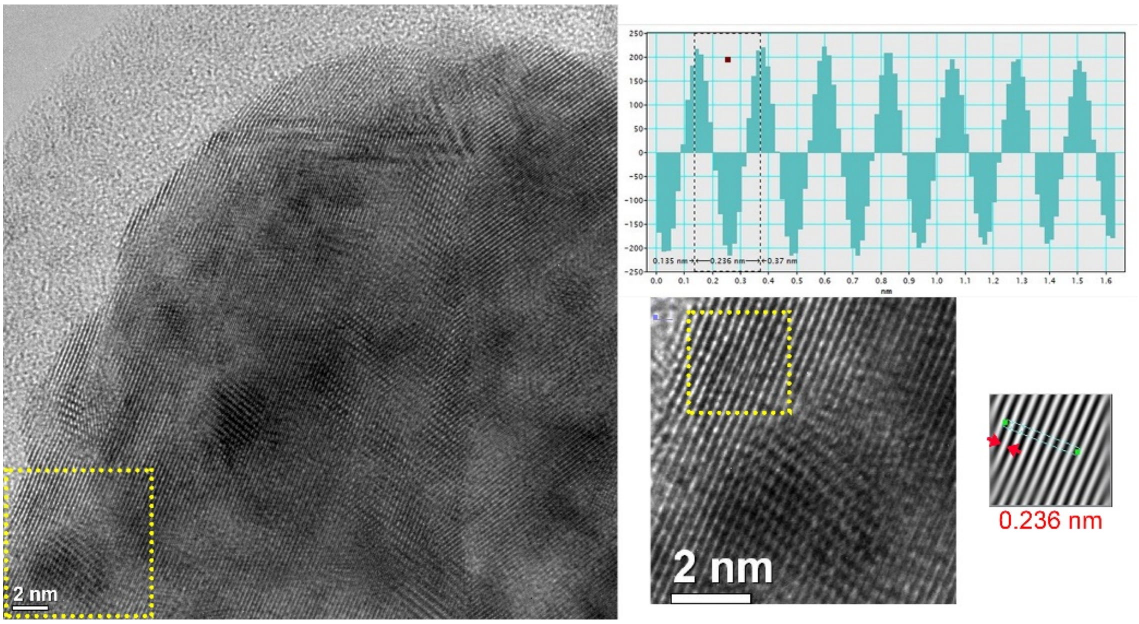

Figure 4.15: Lattice spacing measurement of fresh np-Au sample (highlighted area) via bright-field high resolution TEM, indicating d = 0.236 nm, belonging to (1 1 1) plane of Au metal (PDF 99-0056) (Fam, Sheppard et al. 2019).

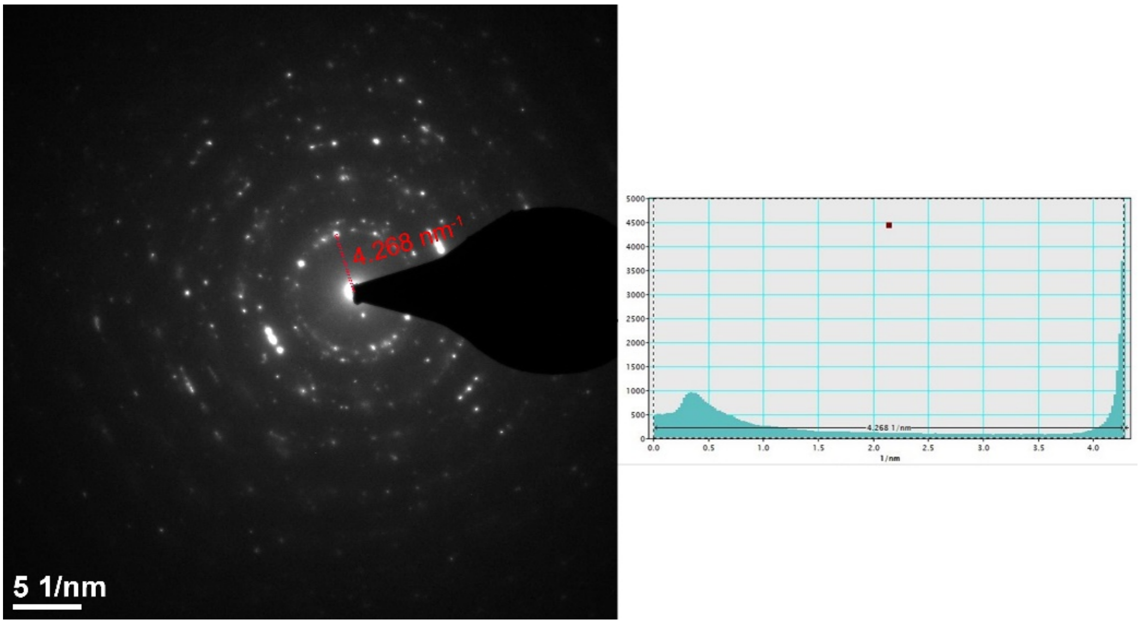

Figure 4.16: Lattice spacing measurement of fresh np-Au sample (between indicated points) via selected area electron diffraction, indicating d = 0.234 nm, belonging to (1 1 1) plane of Au metal (PDF 99-0056) (Fam, Sheppard et al. 2019).

To confirm the effect of thermal stabilization by metal oxides, the next sample of CeO_2/npAu was then investigated. Still under inert atmosphere, the results in Figure 4.17 show that the sample was stable up to 660 °C with an appearance of a crack (Figure 4.17d), which was later used a natural marker point. The crack was then observed to be spreading as the temperature went higher. This sample therefore verifies that the incorporation of CeO_2 delays the onset annealing temperature of np-Au under inert condition, even though the delay is slightly. Moreover, this result also corroborates the previous report carried out under N_2 stating that the same sample could maintain the structure up to 585 °C (Shi, Schaefer et al. 2014).

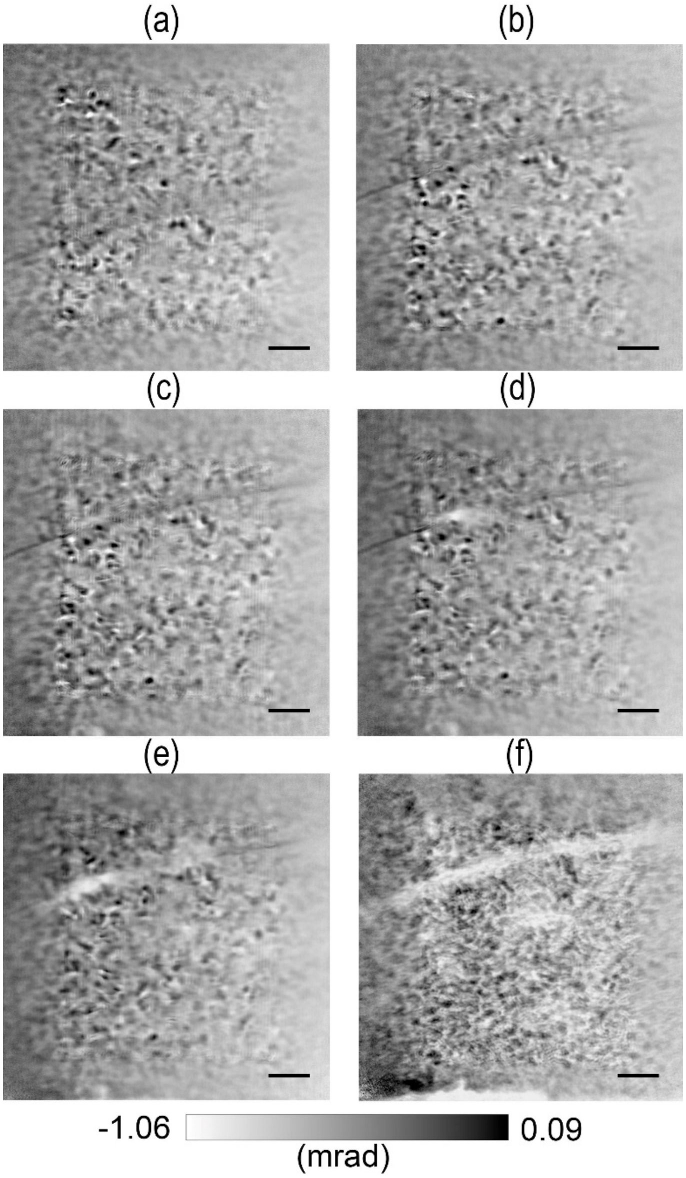

Figure 4.17: XRP images from thermal annealing of CeO_2/npAu under He environment at (a) 20 °C, (b) 600 °C, (c) 650 °C, (d) 660 °C, (e) 700 °C, and (f) 810 °C. The scalebar is 1 µm.

The next experiment probed TiO_2/npAu as the object under similarly inert He gas, in order to find which metal oxide is superior for thermal stabilization effect on npAu. The results in Figure 4.18 exhibit the superiority of TiO_2 as the stabilizer, where the morphology did not change even after heating up to 780 °C. Beyond that, it was unfortunately not possible due to a technical problem during measurement, but this sample was again re-studied with similar tendency in the coming section although it was under oxidizing atmosphere. Besides, an XRF measurement was eventually carried out for this sample and the results in Figure 4.18b and 4.18d indicate a good dispersion of TiO_2 particles over npAu before and after annealing even though the spatial resolution might be the bottleneck in this case.

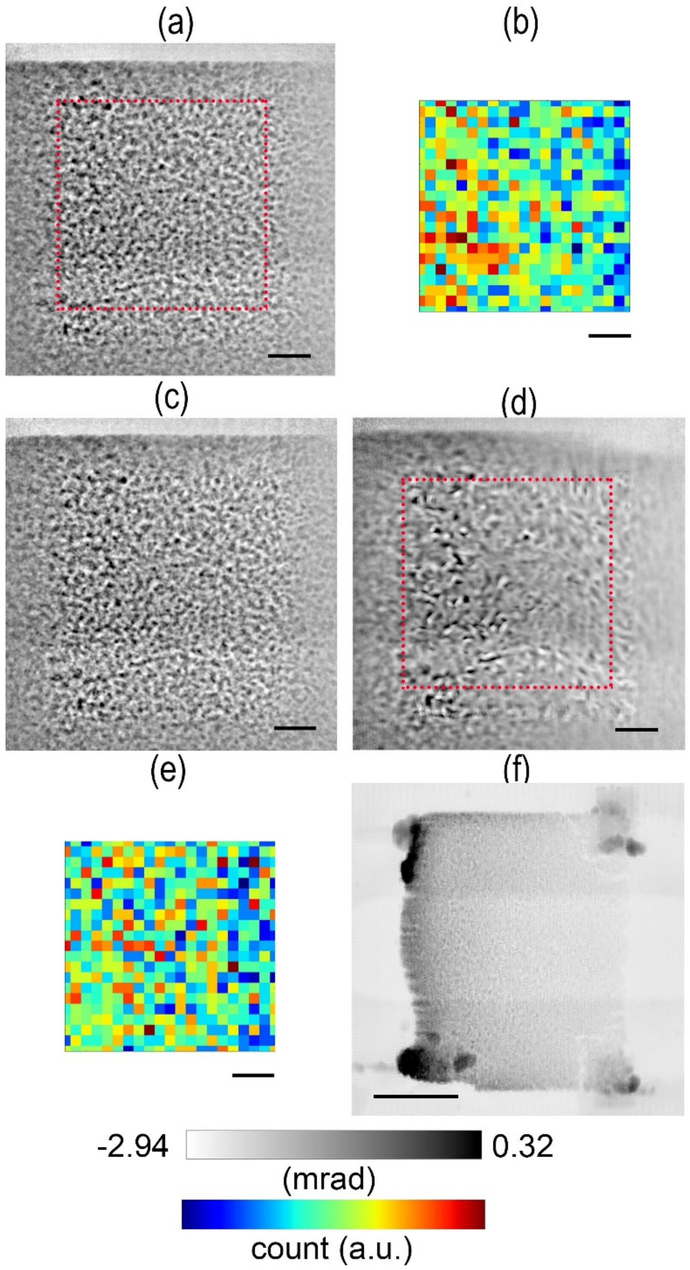

Figure 4.18: XRP images from thermal annealing of TiO_2/npAu under He environment at (a) 20 °C, (c) 600 °C, (d) 780 °C, and (f) its overview scan at 780 °C. Ti-signal XRF mapping (b) from the highlighted area in (a); (e) from the highlighted area in (d). The scalebar is 1 µm, except 5 µm in (f).

To investigate another variable, i.e. the effect of atmosphere, on the thermal annealing of npAu, the last two studies were performed under synthetic air (O_2/He) using CeO_2/npAu and TiO_2/npAu. For CeO_2/npAu, the results in Figure 4.19 indicate that the onset coarsening temperature was 550 °C and it became more progressive up to 800 °C. In comparison to the previous same sample study under inert environment, the oxidizing atmosphere triggered an earlier coarsening in terms of material loss. Moreover, the XRF mapping (Figure 4.19e) interestingly displays the agglomeration of CeO_2 particles over npAu, which was expected considering a Hüttig-temperature of metal oxides around 720 °C. Compared to our previous result using the older generation cell (Baier, Wittstock et al. 2016), the onset temperature was 355 °C. This discrepancy could result from the difference in sample amount/thickness or the amount of oxidizing gas flown onto the sample.

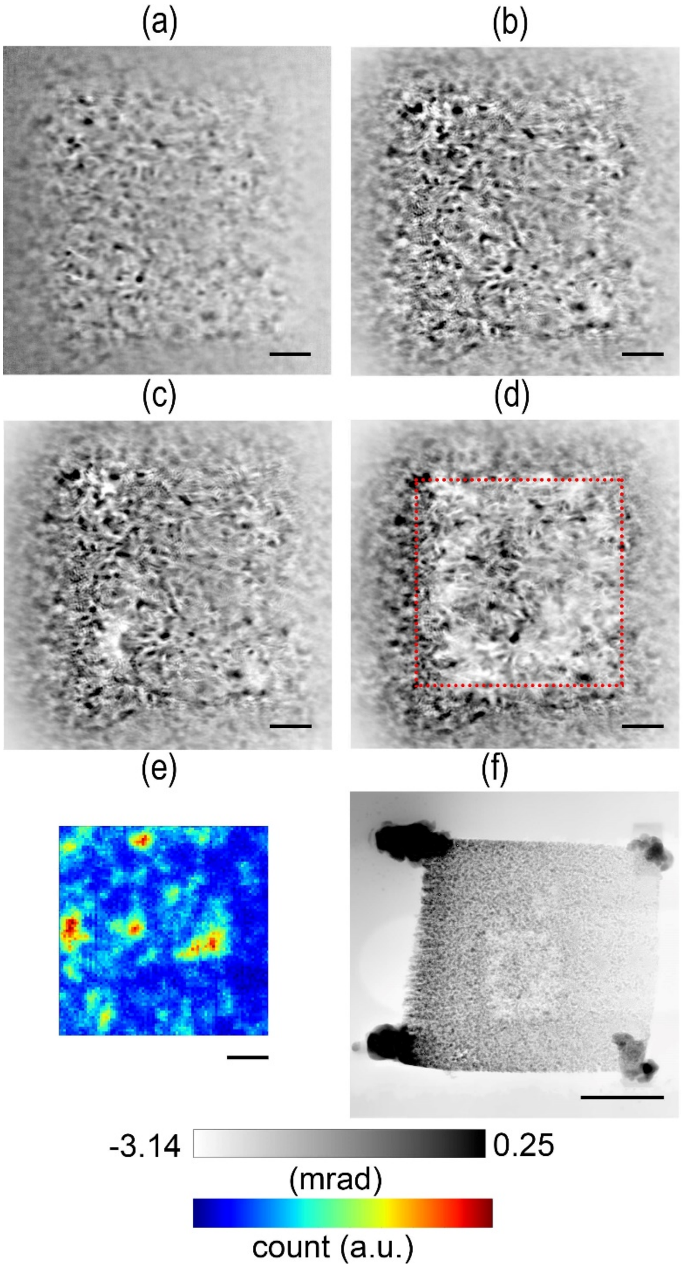

Figure 4.19: XRP images from thermal annealing of CeO_2/npAu under O_2/He environment at (a) 20 °C, (b) 550 °C, (c) 600 °C, (d) 800 °C, and (f) its overview scan at 800 °C. (e) Ce-signal XRF mapping from the highlighted area in (d). The scalebar is 1 µm, except 5 µm in (f).

The last experiment on TiO_2/npAu under synthetic air results in Figure 4.20, showing the stability up to 900 °C. Beyond that, the sample seemed to gradually melt and progressively worse until 1300 °C as it is the maximum temperature for the setup. It is obvious at 1300 °C that half of the sample had been melted away, but the Pt glue on the corner still existed owing to its higher melting point. Besides, the XRF mapping in Figure 4.20c and 20f visualize the contrast difference of TiO_2 distribution on npAu, where the latter depicts some aggregation on one side due to the coarsening of TiO_2. Another important point is the superiority of TiO_2 as the stabilizing agent, which corroborates the previously same sample studied under He gas. Besides, this result also corroborates the previous report carried out under air stating that the same sample could maintain the structure at 450 °C (Shi, Mahr et al. 2017), although they did not try higher temperatures.

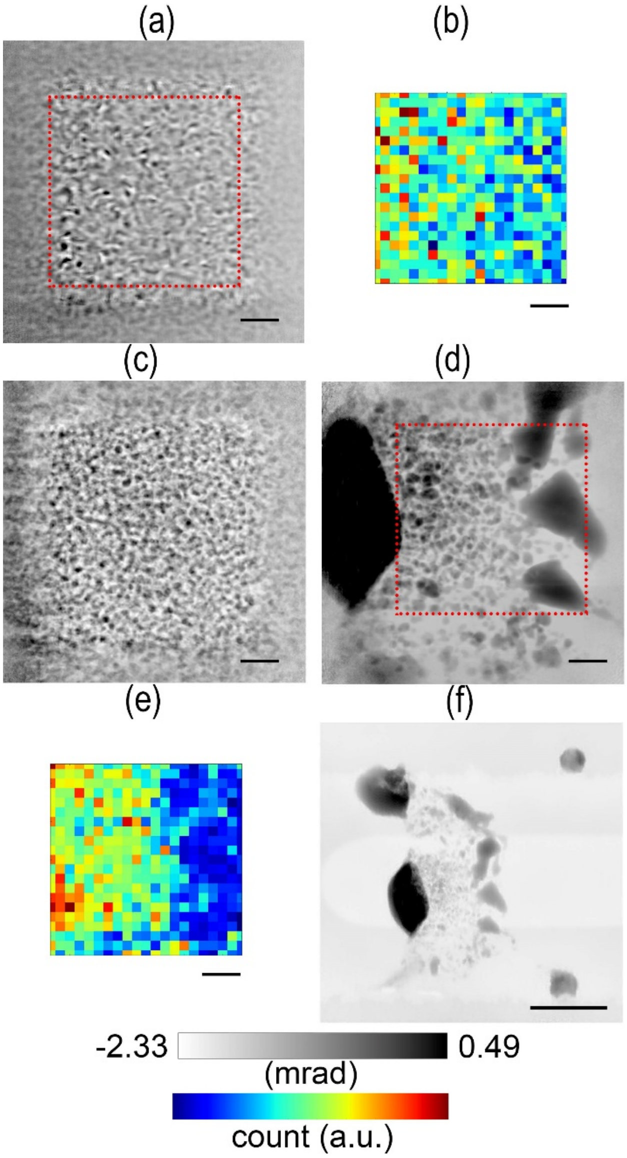

Figure 4.20: XRP images from thermal annealing of TiO_2/npAu under O_2/He environment at (b) 20 °C, (d) 900 °C, and (e) 1300 °C. An overview scan at (a) 20 °C and (g) 800 °C. Ce-signal XRF mapping (c) from the highlighted area in (b); (f) from the highlighted area in (e). The scalebar is 1 µm, except 5 µm in (f).

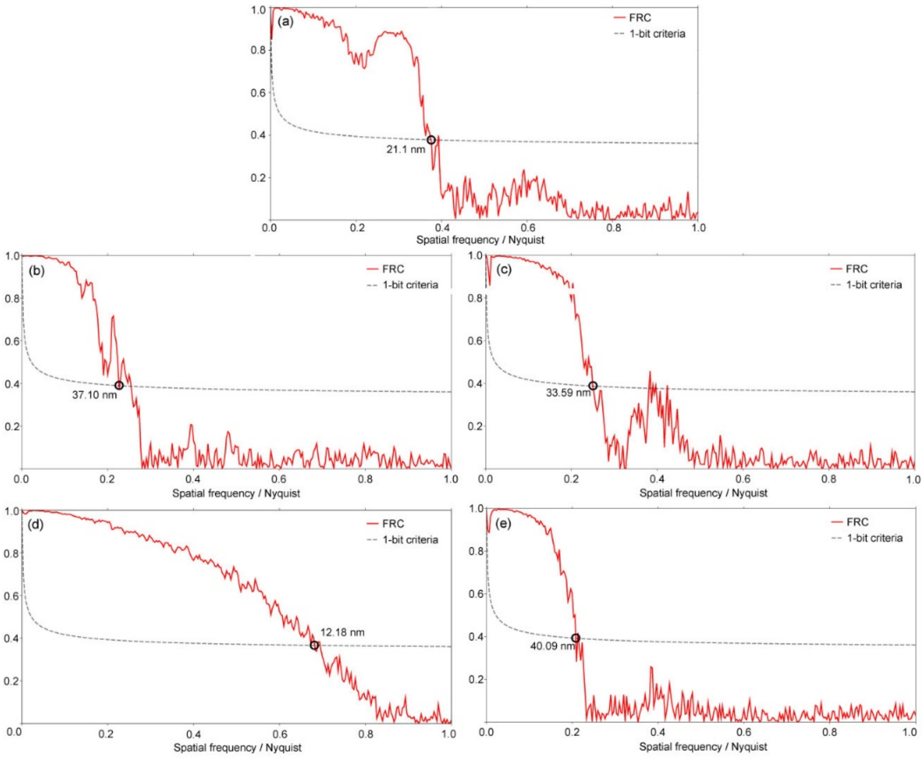

Figure 4.21: FRC for the ptychograms of npAu under He (a) in Figure 4.12, CeO_2/npAu under He (b) in Figure 4.17 and O_2/He (c) in Figure 4.18, TiO_2/npAu under He (d) in Figure 4.19 and O_2/He (e) in Figure 4.20.

4.4.3 Rotational angle test of 3G cell for *in situ* limited-angle PXCT experiments

Despite the same experimental capabilities for *in situ* XRP studies, the 3G cell allows a rotation/tilting feature for *in situ* PXCT in a closed cell. The ideal rotational/tilting angle for an optimized PXCT experiment is ±90°, but the requirement of closed cell makes it impossible to achieve such a demand, so the maximum possible angle preferably close to that ideal value for this cell was evaluated. Therefore, a PXCT experiment was performed using a single ZSM5 crystal and the cell without any heating treatment. This sample was suitably selected due to its well identifiable interior features comprising 2-4 µm crystals with micropores (< 2nm) together with voids of several hundred nm (Machoke, Beltrán et al. 2015, Schwieger, Machoke et al. 2016, Przybilla, Zubiri et al. 2018), but such extremely tiny micropores are unfortunately beyond the capability of PXCT, so the information in that scale has to be specifically obtained by ET measurement if necessary. Besides, the main reason to not involve any thermal treatment was because of the very high thermal stability of ZSM5, resulting in the lack of apparent annealing effect as in npAu. Nevertheless, this ZSM5 only serves as a proof-of-concept for *in situ* PXCT measurements, such as drying, annealing, gas storage and sensing of functional materials.

Here, an *ex situ* PXCT was carried out using the fully assembled 3G cell at room temperature under He gas environment. Figure 22d shows the projected 2D ptychogram of ZSM5 at a tilting angle of 0°, where the cell was positioned perpendicular to the incoming X-ray. After the trial of tilting angle, the maximum possible one with the fully assembled cell was apparently ±35° as shown in Figure 22b,f. Exceeding this limit would result in a blocked X-ray by the cell body, negatively affecting the scattering signals of the sample and thus the reconstruction quality. However, it is possible to attain rotational angles of ±65° if the MEMS chip is removed from the cell, which is useful later to help in improving the tomographic reconstruction. Since only limited projections at ±35° are possible, a common issue, known as “missing wedges” in ET measurement, for tomographic reconstruction is then inevitable (Arslan, Tong et al. 2006).

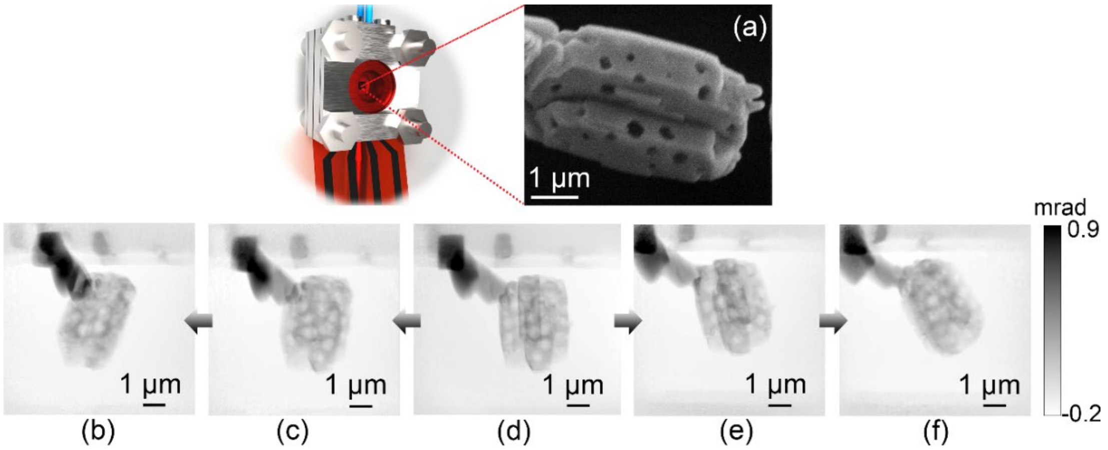

Figure 4.22: Tilting angle tests using micro/macroporous zeolite as a case study: (a) illustration of the 3G cell with corresponding SEM image of the zeolite crystal on a MEMS chip, and ptychograms of the specimen at tilting angles with respect to the incident beam: (b) 35°, (c) 15°, (d) 0°, (e) -15°, (f) -35°. Dark spots in phase maps indicate areas rich in Si/Al. Pt-glue is visible as the dark region in the upper left of each image (Fam, Sheppard et al. 2019).

Several reconstruction procedures, i.e. deep learning, simultaneous algebraic reconstruction technique (SART), simultaneous iterative reconstruction technique (SIRT), and maximum likelihood expectation maximization (MLEM), were carried out for comparison and shown in Figure 23. While the former is new and under development by P06 beamline scientists, the last three methods are already established and only make use of the limited angles of ±35°, so significant elongation and edge blurring effects (Kupsch, Lange et al. 2016) could be expectedly observed in Figure 23b-d due to the missing wedge during tomographic reconstruction. The former method based on machine learning with such a clearer and sharper result in Figure 23a is therefore the best one for *in situ* limited-angle PXCT, not to mention that there are definitely many rooms for improvement in the reconstruction quality. Since it is a new method, unpublished, and developed by P06 beamline scientists at DESY, the full reconstruction result or the 3D volume can’t be included in this dissertation owing to the copyright claim. Therefore, this work also clearly indicates the collaboration between KIT providing the *in situ* equipment and DESY with the beamline infrastructure/data processing.

With respect to the machine learning method, there are two feasible options to apply this algorithm in *in situ* limited angle PXCT experiments using 3G cell. First is by simply removing the MEMS chip for the desired PXCT scans if an atmospheric environment is not imperative for the entire study. Second is by conducting the PXCT scans before and after the *in situ* experiment in 2D if the sample is sensitive to the atmospheric air or a particular environment is required throughout the experiment. In general, the additional ±30°, which is nearly double than for the other three methods, are helpful to compensate the missing projections and it has often been used for similar missing-wedge data from ET measurements (Midgley and Dunin-Borkowski 2009, Zečević, de Jong et al. 2013).

Other considerable means to improve the reconstruction quality include increasing the number of projections by selecting a more refined increment of angles on the sample, where it was highly likely undersampled in this case, but the consequently extended measurement time has to be taken into account, particularly when the probed sample still undergoes some changes. Next, reduction of sample thickness is also another way to decrease the measurement while maintaining the data quality, even though it is not optimal for catalytic materials with an ideal requirement that the sample should be as intact as possible so as to keep the structure and activity (Madejski, Lucas et al. 2018).

In summary, this study confirms the potential of using 3G cell with limited-angle projections and a preliminary reconstruction algorithm for generating tomographic results, although further enhancement in acquisition parameters and reconstruction technique are anticipated in the future. By making use of 3G cell in its full capability, generating even limited 3D volume data series *in situ* should interest the public users in the development of synchrotron X-ray imaging works.

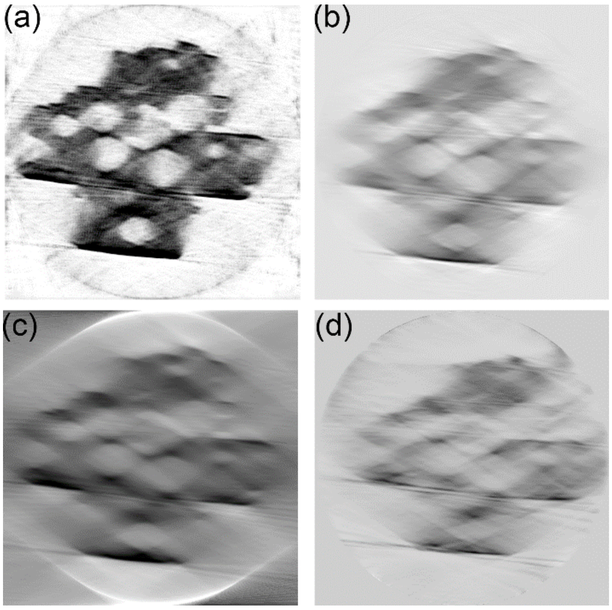

Figure 4.23: Single slice following tomographic reconstruction of the hierarchical zeolite sample from limited-angle data by: (a) an in-house deep learning method (under development at P06); (b) SART from the "scikit-image" Python package; (c) SIRT from the TomoJ plugin of FIJI software; (d) MLEM from the "TomoPy" Python toolbox (Fam, Sheppard et al. 2019).

4.4.4 *In situ* annealing of $CoMnO_2$-HS in controlled gas environment using 3G cell

As the first implementation of *in situ* PXCT experiment, an annealing of $CoMnO_2$-HS single crystal was selected as the model study. In order to avoid any unnecessary tomographic measurement on samples when there was not any obvious change, the study was conducted in such a way, where PXCT was carried out before and after the heating as well as when the dynamics were significant, while the in-between monitoring including temperature ramps were done using XRP. Figure 24 depicts the evolution of $CoMnO_2$-HS crystal (supported by Pt-glue for fixing the crystal on the hole of MEMS chip) along with the increasing temperatures. It began to slightly change at 130 °C, then barely at 200 °C, followed by an obvious shrinking at 410 °C until 720 °C. It should be noted that a hole inside the hollow structure is noticeable at 410 °C, meaning that the structural degradation occurred for both the external layer and hollow structure. Afterwards, the shrinking stopped and it started to gradually-yet-subtly expand until 1000 °C. From those 2D images, it can be inferred that drying should be the main process for such shrinking behaviour.

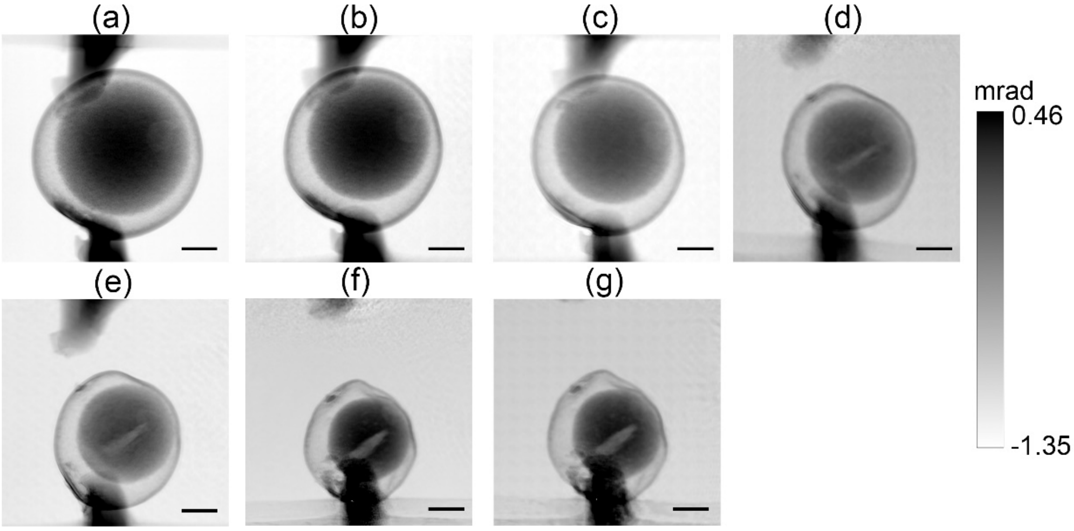

Figure 4.24: Ptychograms of $CoMnO_2$-HS during thermal treatment under He atmosphere at (a) 20 °C, (b) 130 °C, (c) 200 °C, (d) 410 °C, (e) 500 °C, (f) 720 °C, and (g) 1000 °C. All scale bars are 1 µm.

PXCT was carried out before and after thermal treatment at 1000 °C with the aim to investigate the dynamics of $CoMnO_2$-HS during annealing from various perspectives, unlike one perspective only from XRP. Figure 25 shows both axial and sagittal views of $CoMnO_2$-HS before and after heating. Although the reconstruction quality is not ideal with severe elongation effect due to the missing wedge situation without any machine-learning reconstruction method, this information is more informative than the ones from XRP. Comparing between Figure 25a-c indicate that the shrinking and displacement of $CoMnO_2$-HS happened not only in 2 axes (as shown in Figure 24), but also in 3 axes (x, y, and z). Despite the lack of 3D volume data, purely because of the ineligibility of reconstructed tomograms via TomoJ for segmentation, this study briefly verifies the versatility of 3D imaging under in situ via PXCT technique.

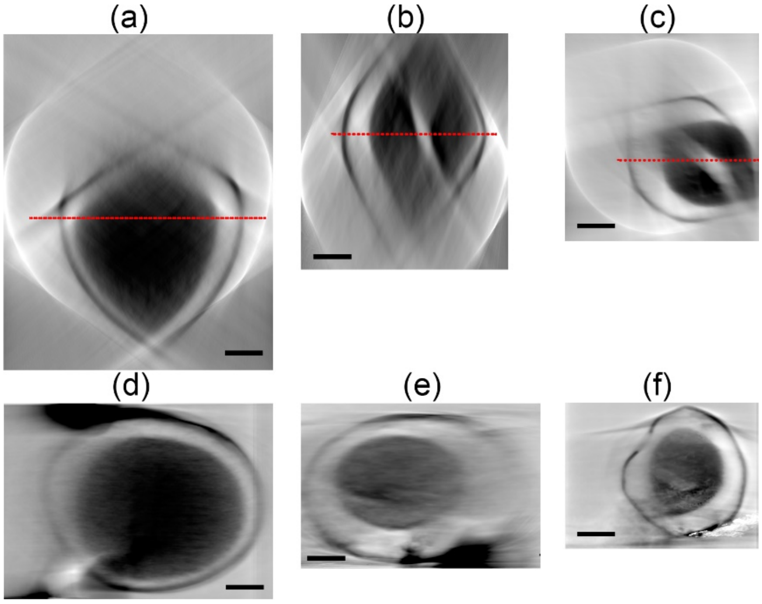

Figure 4.25: Tomogram slices of CoMnO$_2$-HS before (a,d) and after thermal treatment at 410 °C (b,e) and 1000 °C (c,f) via tomographic reconstruction by TomoJ plugin of FIJI software, where the views were performed in the form of (a-c) axial section and (d-f) sagittal section. The red dashed lines indicate the sagittal slices of (a-b). All scale bars are 1 µm.

4.5 Conclusions

Two *in situ* cells for complementary X-ray and electron microscopy have been developed and built for users at the hard X-ray nanoprobe endstation at P06 beamline of PETRA III synchrotron radiation source. They deliver more advantages than the formerly established nanoreactors for *in situ* XRP experiments. The feasibility studies for the cells were confirmed in the form of microscopic investigations during thermal annealing under particular gas atmospheres, using monolithic npAu within 2G cell for *in situ* XRP experiment and single-particle CoMnO$_2$-HS for *in situ* PXCT experiment. Aside from the cells, the precise control and user-friendliness of the heating interface system as well as gas flow setup are the other key factors in successfully performing thermal annealing studies of porous materials under controlled environments. Moreover, the complementary TEM measurements on the same sample before and after *in situ* XRP exhibit another vantage to showcase the versatility of the cells in performing multiscalar imaging experiments. With respect to 3D imaging, 3G cell has proved to be able to carry out the limited-angle *in situ* PXCT with a maximum angle of ±35° although the resulting missing projections severely hinder the tomographic reconstruction process. However, this limitation could be mitigated by imaging outside of the cell, allowing more projections ±35° acquired between sequential treatment under reaction conditions. Furthermore, other integrated techniques, such as XRF and EDX for elemental analysis, XRD and SAED for crystallinity analysis, XAS and EELS for oxidation state analysis, could also be complementarily executed for more informative analyses. Last, this setup is also a great potential for applications in redox reactions, gas storage, gas sensing, or catalysis, which will be made publicly available for users of P06 beamline at PETRA III.

5 General Conclusions and Outlook

Reflecting back to the aim of this dissertation, the work here can be concluded to have a synergistic effect between *in situ* studies, 3D imaging, and the complementary use of electron and X-ray techniques. It starts with chapter 2 introducing the benefit of 3D imaging as well as highlighting advantages and disadvantages, particularly for ET and PXCT, hence they should be combined to compensate their weaknesses. This is elaborated on chapter 3, where ET exhibited its superiority in resolving the small nanoparticles and PXCT proved its usefulness in probing more representative volume of the sample. Moreover, chapter 3 also inferred the important capability of PXCT for *in situ* experiments, which was later realized in chapter 4 by the eventual development of the 2G/3G cells. The establishment of those cells later helps in approaching the ideal goal, where *in situ* PXCT is complemented by *ex situ* ET.

Although XRM is the highlight of this dissertation, EM (particularly TEM) cannot be underestimated due to its powerful ability in resolving features beyond the capability of XRM. TEM is able to structurally resolve up to the sub-nm scale (0.5 nm in this work or even lower with other materials), whereas the highest spatial resolution from XRM is presently only 10 nm at best. However, the better resolution of TEM sacrifices the requirement of sample thickness limited only to a few hundreds nm, while XRM is relatively more lenient (several tens of µm or more depending on the material) in this regard. Moreover, TEM has another limitation in its working condition as it is typically performed under vacuum, especially for 3D imaging experiments, so as to prevent any interaction with particles, whereas X-ray is more flexible (up to 1.1 bar in this work) and relatively more inert, making it easier to apply in *in situ* studies. With respect to the experimental access and instrument availability, TEM definitely wins over XRM, where TEM is more commercially available and affordable and many techniques of XRM requires synchrotron facilities, whose access is very limited in terms of time and place. Considering both pluses and minuses between both techniques, the complementarity is therefore imperative to benefit from the best of both worlds.

With respect to the 3D imaging, the resulting information is indeed more useful and informative than the 2D counterpart, but one should also consider whether the time is always worth spending on it when only 2D is enough? As there is an analogy about using microscope to study an elephant, one should also wisely think before one act. Nevertheless, the abundance of hidden benefits of 3D imaging are surely too tempting to refuse. The calculation of surface area, porosity, mass density, their corresponding mapping in 3D, not to mention the accurate morphology depiction in 3D, and even further use for simulation/modelling to reveal the intrinsic physical properties (fluid permeability and diffusivity, electrical and thermal conductivity); all of those can be extracted by only a single technique, which seems to be too good to be true, yet it apparently is not. While ET data with superior spatial resolutions have been commonly used for simulations, PXCT with larger fields of view due to the higher penetration depth cannot be underestimated, particularly for inhomogeneous samples in order to better represent the sample. Moreover, among other X-ray imaging techniques, PXCT is promising for tomography-based simulation due to its highest spatial resolution so far, which can reach up to sub-nm with the arrival of 4th generation synchrotron radiation facilities. Furthermore, the fact that the models were simulated using the actual measurement data via PXCT in this case, makes an appealing factor to save the time in optimization for further applications of the materials.

As for the *in situ* part, not only the possibility to see “live” the dynamics of materials under controlled environments and heating exists, but also the potential to unravel that in 3D is even more captivating with all the aforesaid benefits. However, such an ideal case comes with a great price, where challenges in the gas-leak, accurate heating control, the internal volume minimization, setup stability, fast image acquisition, and image reconstruction are difficult since they are dependent on each other. In this work, the feasibility of online 2D morphological monitoring has been approved by performing *in situ* XRP to resolve nanoscale (down to 12 nm) structural features of several functional materials, partly complemented by *ex situ* TEM (before and after *in situ* XRP) to investigate the atomic structures. Furthermore, it is still a proof of concept for the online 3D structural monitoring via *in situ* PXCT due to the limitation in developing limited-angle tomographic reconstruction. Despite the limited angles leading to missing wedge problem, the reconstruction process to generate 3D volume is still possible and promising thanks to the machine learning algorithm developed by the beamline scientists at DESY.

Several improvements and continuing works have to be conducted, especially for the X-ray imaging part in this case. While electron imaging techniques have been far ahead in development and even commercialized by several famous companies in the world, X-ray imaging techniques are still in development and progressively, aside from the fact that X-ray computed tomography is the only one famous technique under the big umbrella of X-ray microscopy, having been applied in many fields. Other than that, many other X-ray imaging techniques (scanning transmission X-ray microscopy, or coherent diffraction imaging, or Bragg diffraction imaging, or phase-contrast imaging, let alone XRP) are less known or specifically overshadowed by electron imaging techniques and even worse that the implementation opportunity is limited only in synchrotron radiation facilities. Therefore, the application of portable or lab-scale instruments for those other techniques are essential to compete against the electron imaging techniques. In terms of spatial resolution, the development of optics and beam brightness for X-ray imaging is also crucial, but this will be realized by the arrival of 4th generation synchrotron radiation facility in the next ten years. Besides, the concern for beam damage should also be put into consideration with the arrival of higher power of the source. Depending on the material, it is advised to initially carry out *ex situ* to find an optimized parameter under the beam. Image acquisition and reconstruction algorithm for any tomography method should also be more time-efficient, but this can be expected quite soon as the hardware and computational resources have been growing rapidly in the past decade. For the *in situ* cells themselves, a structural optimization to reduce the internal volume and an upgrade to have a 4G cell with a full rotation are surely desired. Implementation of *in situ* PXCT, complemented by *ex situ* ET before and after *in situ* PXCT should be carried out for other advanced experiments, such as redox reactions, gas storage, gas sensing, or even catalysis for *operando* experiments. Furthermore, other integrated techniques, such as *in situ* XRF with *ex situ* EDX for elemental analysis, XRD with SAED for crystallinity analysis, XAS with EELS for oxidation state analysis, should also be carried out along with *in situ* XRP with *ex situ* TEM or PXCT with ET for more informative analyses. This also points out the benefit of complementary XRM and EM, where EM is useful for high resolution imaging and XRM is great for representation of larger sample areas and ease of adaptation for *in situ* studies.

Last for the sample preparation, another technique other than FIB is strongly required as there are not many other options so far, except for plasma FIB or helium ion microscopy, which can accelerate the milling process significantly. This can be a great solution although the instruments have not yet been widespreadly available due to the accesibility issues. Another solution worth consideration is the laser cutting process. Despite the limitations in spatial resolution (maximum in sub-mm regions) and thermal stability inducing possibly worse damage than FIB, it can also be included as the initial cutting step from the bulk material to save the time for FIB milling.

Bibliography

Alton, G. D. and P. M. Read (1989). "The emittance characteristics of a gallium liquid-metal ion source." J. Appl. Phys. **66**(3): 1018-1022.

Andersen, A. H. and A. C. Kak (1984). "Simultaneous Algebraic Reconstruction Technique (SART): A superior implementation of the ART algorithm." Ultrason. Imaging **6**(1): 81-94.

Andrews, J. C. and B. M. Weckhuysen (2013). "Hard X-ray Spectroscopic Nano-Imaging of Hierarchical Functional Materials at Work." ChemPhysChem **14**(16): 3655-3666.

Aramburo, L. R., E. de Smit, B. Arstad, M. M. van Schooneveld, L. Sommer, A. Juhin, T. Yokosawa, H. W. Zandbergen, U. Olsbye, F. M. F. de Groot and B. M. Weckhuysen (2012). "X-ray Imaging of Zeolite Particles at the Nanoscale: Influence of Steaming on the State of Aluminum and the Methanol-To-Olefin Reaction." Angew. Chem. Int. Ed. **51**(15): 3616-3619.

Aramburo, L. R., S. Wirick, P. S. Miedema, I. L. C. Buurmans, F. M. F. de Groot and B. M. Weckhuysen (2012). "Styrene oligomerization as a molecular probe reaction for Brønsted acidity at the nanoscale." Phys. Chem. Chem. Phys. **14**(19): 6967-6973.

Arslan, I., J. R. Tong and P. A. Midgley (2006). "Reducing the missing wedge: High-resolution dual axis tomography of inorganic materials." Ultramicroscopy **106**(11): 994-1000.

Bagge-Hansen, M., A. Wichmann, A. Wittstock, J. R. I. Lee, J. Ye, T. M. Willey, J. D. Kuntz, T. van Buuren, J. Biener, M. Bäumer and M. M. Biener (2014). "Quantitative Phase Composition of TiO2-Coated Nanoporous Au Monoliths by X-ray Absorption Spectroscopy and Correlations to Catalytic Behavior." J. Phys. Chem. C **118**(8): 4078-4084.

Baier, S., C. D. Damsgaard, M. Klumpp, J. Reinhardt, T. Sheppard, Z. Balogh, T. Kasama, F. Benzi, J. B. Wagner, W. Schwieger, C. G. Schroer and J.-D. Grunwaldt (2017). "Stability of a Bifunctional Cu-Based Core@Zeolite Shell Catalyst for Dimethyl Ether Synthesis Under Redox Conditions Studied by Environmental Transmission Electron Microscopy and In Situ X-Ray Ptychography." Microsc. Microanal.: 1-12.

Baier, S., C. D. Damsgaard, M. Scholz, F. Benzi, A. Rochet, R. Hoppe, T. Scherer, J. Shi, A. Wittstock, B. Weinhausen, J. B. Wagner, C. G. Schroer and J.-D. Grunwaldt (2016). "In Situ Ptychography of Heterogeneous Catalysts using Hard X-Rays: High Resolution Imaging at Ambient Pressure and Elevated Temperature." Microsc. Microanal. **22**(1): 178-188.

Baier, S., A. Wittstock, C. D. Damsgaard, A. Diaz, J. Reinhardt, F. Benzi, J. J. Shi, T. Scherer, D. Wang, C. Kubel, C. G. Schroer and J.-D. Grunwaldt (2016). "Influence of gas atmospheres and ceria on the stability of nanoporous gold studied by environmental electron microscopy and in situ ptychography." RSC Adv. **6**(86): 83031-83043.

Bañares, M. A. (2005). "Operando methodology: Combination of in situ spectroscopy and simultaneous activity measurements under catalytic reaction conditions." Catal. Today **100**(1-2): 71-77.

Bar Sadan, M., L. Houben, S. G. Wolf, A. Enyashin, G. Seifert, R. Tenne and K. Urban (2008). "Toward Atomic-Scale Bright-Field Electron Tomography for the Study of Fullerene-Like Nanostructures." Nano Lett. **8**(3): 891-896.

Barnard, J. S., J. Sharp, J. R. Tong and P. A. Midgley (2006). "High-Resolution Three-Dimensional Imaging of Dislocations." Science **313**(5785): 319-319.

Barnard, J. S., J. Sharp, J. R. Tong and P. A. Midgley (2006). "Three-dimensional analysis of dislocation networks in GaN using weak-beam dark-field electron tomography." Philos. Mag. **86**(29-31): 4901-4922.

Basile, D. P. (1992). Specimen Preparation for Transmission Electron Microscopy of Materials-III. Mater. Res. Soc. Symp. Proc., Pittsburgh, Pennsylvania, USA, Materials Research Society.

Basile, F., P. Benito, S. Bugani, W. De Nolf, G. Fornasari, K. Janssens, L. Morselli, E. Scavetta, D. Tonelli and A. Vaccari (2010). "Combined Use of Synchrotron-Radiation-Based Imaging Techniques for the Characterization of Structured Catalysts." Adv. Funct. Mater. **20**(23): 4117-4126.

Beale, A. M., S. D. M. Jacques and B. M. Weckhuysen (2010). "Chemical imaging of catalytic solids with synchrotron radiation." Chem. Soc. Rev. **39**(12): 4656-4672.

Behrens, M., F. Studt, I. Kasatkin, S. Kühl, M. Hävecker, F. Abild-Pedersen, S. Zander, F. Girgsdies, P. Kurr, B.-L. Kniep, M. Tovar, R. W. Fischer, J. K. Nørskov and R. Schlögl (2012). "The Active Site of Methanol Synthesis over Cu/ZnO/Al₂O₃ Industrial Catalysts." Science **336**(6083): 893-897.

Biener, M. M., J. Biener, A. Wichmann, A. Wittstock, T. F. Baumann, M. Bäumer and A. V. Hamza (2011). "ALD Functionalized Nanoporous Gold: Thermal Stability, Mechanical Properties, and Catalytic Activity." Nano Lett. **11**(8): 3085-3090.

Bleuet, P., E. Welcomme, E. Dooryhée, J. Susini, J.-L. Hodeau and P. Walter (2008). "Probing the structure of heterogeneous diluted materials by diffraction tomography." Nat. Mater. **7**(6): 468-472.

Borisevich, A. Y., S. Wang, S. N. Rashkeev, M. Glazoff, S. J. Pennycook and S. T. Pantelides (2007). "Dual Nanoparticle/Substrate Control of Catalytic Dehydrogenation." Adv. Mater. **19**(16): 2129-2133.

Bruyant, P. P. (2002). "Analytic and iterative reconstruction algorithms in SPECT." J. Nucl. Med. **43**(10): 1343-1358.

Buurmans, I. L. C., J. Ruiz-Martínez, W. V. Knowles, D. van der Beek, J. A. Bergwerff, E. T. C. Vogt and B. M. Weckhuysen (2011). "Catalytic activity in individual cracking catalyst particles imaged throughout different life stages by selective staining." Nat. Chem. **3**: 862.

Buurmans, I. L. C. and B. M. Weckhuysen (2012). "Heterogeneities of individual catalyst particles in space and time as monitored by spectroscopy." Nat. Chem. **4**(11): 873-886.

Cantoni, M. and L. Holzer (2014). "Advances in 3D focused ion beam tomography." MRS Bull. **39**(4): 354-360.

Carmona, A., P. Cloetens, G. Devès, S. Bohic and R. Ortega (2008). "Nano-imaging of trace metals by synchrotron X-ray fluorescence into dopaminergic single cells and neurite-like processes." J. Anal. Atom Spectrom. **23**(8): 1083-1088.

Cavalca, F., A. B. Laursen, B. E. Kardynal, R. E. Dunin-Borkowski, S. Dahl, J. B. Wagner and T. W. Hansen (2012). "In situtransmission electron microscopy of light-induced photocatalytic reactions." Nanotechnology **23**(7): 075705.

Cesar da Silva, J., A. Pacureanu, Y. Yang, S. Bohic, C. Morawe, R. Barrett and P. Cloetens (2017). "Efficient concentration of high-energy x-rays for diffraction-limited imaging resolution." Optica **4**(5): 492-495.

Che, M. and J. C. Védrine (2012). Characterization of Solid Materials and Heterogeneous Catalysts: From Structure to Surface Reactivity. Weinheim, Wiley-VCH.

Chen-Wiegart, Y.-c. K., S. Wang, Y. S. Chu, W. Liu, I. McNulty, P. W. Voorhees and D. C. Dunand (2012). "Structural evolution of nanoporous gold during thermal coarsening." Acta Mater. **60**(12): 4972-4981.

Chew, N. G. and A. G. Cullis (1987). "The preparation of transmission electron microscope specimens from compound semiconductors by ion milling." Ultramicroscopy **23**(2): 175-198.

Chorkendorff, I. and J. W. Niemantsverdriet (2003). Concepts of Modern Catalysis and Kinetics. Weinheim, Wiley-VCH.

Cooper, S. J., M. Kishimoto, F. Tariq, R. S. Bradley, A. J. Marquis, N. P. Brandon, J. A. Kilner and P. R. Shearing (2013). "Microstructural Analysis of an LSCF Cathode Using In Situ Tomography and Simulation." ECS Transac. **57**(1): 2671-2678.

Creemer, J. F., S. Helveg, G. H. Hoveling, S. Ullmann, A. M. Molenbroek, P. M. Sarro and H. W. Zandbergen (2008). "Atomic-scale electron microscopy at ambient pressure." Ultramicroscopy **108**(9): 993-998.

Cuesta, A., A. G. De la Torre, I. Santacruz, A. Diaz, P. Trtik, M. Holler, B. Lothenbach and M. A. G. Aranda (2019). "Quantitative disentanglement of nanocrystalline phases in cement pastes by synchrotron ptychographic X-ray tomography." IUCrJ **6**(3): 473-491.

Cuesta, A., A. G. De la Torre, I. Santacruz, P. Trtik, J. C. da Silva, A. Diaz, M. Holler and M. A. G. Aranda (2017). "Chemistry and Mass Density of Aluminum Hydroxide Gel in Eco-Cements by Ptychographic X-ray Computed Tomography." J. Phys. Chem. C **121**(5): 3044-3054.

da Silva, J. C., K. Mader, M. Holler, D. Haberthür, A. Diaz, M. Guizar-Sicairos, W.-C. Cheng, Y. Shu, J. Raabe, A. Menzel and J. A. van Bokhoven (2015). "Assessment of the 3 D Pore Structure and Individual Components of Preshaped Catalyst Bodies by X-Ray Imaging." ChemCatChem **7**(3): 413-416.

de Groot, F. M. F., E. de Smit, M. M. van Schooneveld, L. R. Aramburo and B. M. Weckhuysen (2010). "In-situ Scanning Transmission X-Ray Microscopy of Catalytic Solids and Related Nanomaterials." ChemPhysChem **11**(5): 951-962.

de Smit, E., I. Swart, J. F. Creemer, G. H. Hoveling, M. K. Gilles, T. Tyliszczak, P. J. Kooyman, H. W. Zandbergen, C. Morin, B. M. Weckhuysen and F. M. F. de Groot (2008). "Nanoscale chemical imaging of a working catalyst by scanning transmission X-ray microscopy." Nature **456**(7219): 222-225.

de Winter, D. A. M., F. Meirer and B. M. Weckhuysen (2016). "FIB-SEM Tomography Probes the Mesoscale Pore Space of an Individual Catalytic Cracking Particle." ACS Catal. **6**(5): 3158-3167.

Delattre, B., R. Amin, J. Sander, J. De Coninck, A. P. Tomsia and Y.-M. Chiang (2018). "Impact of Pore Tortuosity on Electrode Kinetics in Lithium Battery Electrodes: Study in Directionally Freeze-Cast LiNi0.8Co0.15Al0.05O2 (NCA)." J. Electrochem. Soc. **165**(2): A388-A395.

Dembélé, K., M. Bahri, G. Melinte, C. Hirlimann, A. Berliet, S. Maury, A.-S. Gay and O. Ersen (2018). "Insight by In Situ Gas Electron Microscopy on the Thermal Behaviour and Surface Reactivity of Cobalt Nanoparticles." ChemCatChem **10**(18): 4004-4009.

Deutschmann, O. (2012). Modeling and Simulation of Heterogeneous Catalytic Reactions, John Wiley & Sons.

Dierolf, M., A. Menzel, P. Thibault, P. Schneider, C. M. Kewish, R. Wepf, O. Bunk and F. Pfeiffer (2010). "Ptychographic X-ray computed tomography at the nanoscale." Nature **467**(7314): 436-439.

Donnelly, C., M. Guizar-Sicairos, V. Scagnoli, M. Holler, T. Huthwelker, A. Menzel, I. Vartiainen, E. Müller, E. Kirk, S. Gliga, J. Raabe and L. J. Heyderman (2015). "Element-Specific X-Ray Phase Tomography of 3D Structures at the Nanoscale." Phys. Rev. Lett. **114**(11): 115501.

Echigo, T., N. Monsegue, D. M. Aruguete, M. Murayama and M. F. Hochella, Jr. (2013). "Nanopores in hematite (α-Fe2O3) nanocrystals observed by electron tomography." Am. Mineral. **98**(1): 154-162.

Egerton, R. F. (2005). Physical Principles of Electron Microscopy: An Introduction to TEM, SEM, and AEM. New York, Springer.

Erlebacher, J., M. J. Aziz, A. Karma, N. Dimitrov and K. Sieradzki (2001). "Evolution of nanoporosity in dealloying." Nature **410**: 450.

Erni, R., M. D. Rossell, C. Kisielowski and U. Dahmen (2009). "Atomic-Resolution Imaging with a Sub-50-pm Electron Probe." Phys. Rev. Lett. **102**(9): 096101.

Ertl, G., H. Knözinger, F. Schüth and J. Weitkamp (2008). Handbook of Heterogeneous Catalysis. Weinheim, Wiley-VCH.

Esmaeili, M., J. B. Fløystad, A. Hipp, M. Willner, M. Bech, A. Diaz, A. Røyset, J. W. Andreasen, F. Pfeiffer and D. W. Breiby (2015). "Monitoring moisture distribution in textile materials using grating interferometry and ptychographic X-ray imaging." Text. Res. J. **85**(1): 80-90.

Ewers, B. W., A. S. Crampton, M. M. Biener and C. M. Friend (2017). "Thermally Activated Formation of Reactive Lattice Oxygen in Titania on Nanoporous Gold." J. Phys. Chem. C **121**(39): 21405-21410.

Fam, Y. and T. Imae (2015). "Catalytic oxidation of formaldehyde in water by calcium phosphate-based Pt composites." RSC Adv. **5**(21): 15944-15953.

Fam, Y., T. L. Sheppard, J. Becher, D. Scherhaufer, H. Lambach, S. Kulkarni, T. F. Keller, A. Wittstock, F. Wittwer, M. Seyrich, D. Brueckner, M. Kahnt, A. Schropp, A. Stierle, C. G. Schroer and J.-D. Grunwaldt (2019). "A versatile nanoreactor for complementary in situ X-ray and electron microscopy studies in catalysis and materials science." J. Synchrotron Radiat.

Fam, Y., T. L. Sheppard, A. Diaz, T. Scherer, M. Holler, W. Wang, D. Wang, P. Brenner, A. Wittstock and J.-D. Grunwaldt (2018). "Correlative Multiscale 3D Imaging of a Hierarchical Nanoporous Gold Catalyst by Electron, Ion and X-ray Nanotomography." ChemCatChem **10**(13): 2858-2867.

Fan, Z., L. Zhang, D. Baumann, L. Mei, Y. Yao, X. Duan, Y. Shi, J. Huang, Y. Huang and X. Duan (2019). "In Situ Transmission Electron Microscopy for Energy Materials and Devices." Adv. Mater. **31**(33): 1900608.

Freitag, B., S. Kujawa, P. M. Mul, J. Ringnalda and P. C. Tiemeijer (2005). "Breaking the spherical and chromatic aberration barrier in transmission electron microscopy." Ultramicroscopy **102**(3): 209-214.

Frenkel, A. I. and J. A. Van Bokhoven (2014). "X-ray spectroscopy for chemical and energy sciences: The case of heterogeneous catalysis." J. Synchrotron Radiat. **21**(5): 1084-1089.

Fujita, T., L.-H. Qian, K. Inoke, J. Erlebacher and M.-W. Chen (2008). "Three-dimensional morphology of nanoporous gold." Appl. Phys. Lett. **92**(25): 251902.

Fujita, T., T. Tokunaga, L. Zhang, D. Li, L. Chen, S. Arai, Y. Yamamoto, A. Hirata, N. Tanaka, Y. Ding and M. Chen (2014). "Atomic Observation of Catalysis-Induced Nanopore Coarsening of Nanoporous Gold." Nano Lett. **14**(3): 1172-1177.

Fultz, B. and J. M. Howe (2012). Transmission Electron Microscopy and Diffractometry of Materials. New York, Springer Science and Business Media.

Giannuzi, L. A. and F. A. Stevie (2005). Introduction to Focused Ion Beams: Instrumentation, Theory, Techniques., and Practice. New York, Springer**:** 173.

Giannuzzi, L. A., R. Geurts and J. Ringnalda (2005). "2 keV Ga+ FIB Milling for Reducing Amorphous Damage in Silicon." Microsc. Microanal. **11**(S02): 828-829.

Giannuzzi;, L. A. and F. A. Stevie (2005). Introduction to focused ion beams : instrumentation, theory, techniques, and practice. New York, USA, Springer.

Gocyla, M., S. Kuehl, M. Shviro, H. Heyen, S. Selve, R. E. Dunin-Borkowski, M. Heggen and P. Strasser (2018). "Shape Stability of Octahedral PtNi Nanocatalysts for Electrochemical Oxygen Reduction Reaction Studied by in situ Transmission Electron Microscopy." ACS Nano **12**(6): 5306-5311.

Goldstein, J., D. Newbury, D. Joy, C. Lyman, P. Echlin, E. Lifshin, L. Sawyer and J. Michael (2003). Scanning Electron Microscopy and X-ray Microanalysis. New York, Kluwer Academic / Plenum**:** 21.

Gontard, L. C., L.-Y. Chang, C. J. D. Hetherington, A. I. Kirkland, D. Ozkaya and R. E. Dunin-Borkowski (2007). "Aberration-Corrected Imaging of Active Sites on Industrial Catalyst Nanoparticles." Angew. Chem. Int. Ed. **46**(20): 3683-3685.

Goris, B., S. Bals, W. Van den Broek, J. Verbeeck and G. Van Tendeloo (2011). "Exploring different inelastic projection mechanisms for electron tomography." Ultramicroscopy **111**(8): 1262-1267.

Goris, B., W. Van den Broek, K. J. Batenburg, H. Heidari Mezerji and S. Bals (2012). "Electron tomography based on a total variation minimization reconstruction technique." Ultramicroscopy **113**: 120-130.

Gröger, H., C. Kind, P. Leidinger, M. Roming and C. Feldmann (2010). "Nanoscale Hollow Spheres: Microemulsion-Based Synthesis, Structural Characterization and Container-Type Functionality." Materials **3**(8): 4355-4386.

Grunwaldt, J.-D., L. Basini and B. S. Clausen (2001). "In Situ EXAFS Study of Rh/Al2O3 Catalysts for Catalytic Partial Oxidation of Methane." J. Catal. **200**(2): 321-329.

Grunwaldt, J.-D., S. Hannemann, C. G. Schroer and A. Baiker (2006). "2D-Mapping of the Catalyst Structure Inside a Catalytic Microreactor at Work: Partial Oxidation of Methane over Rh/Al2O3." J. Phys. Chem. B **110**(17): 8674-8680.

Grunwaldt, J.-D., B. Kimmerle, A. Baiker, P. Boye, C. G. Schroer, P. Glatzel, C. N. Borca and F. Beckmann (2009). "Catalysts at work: From integral to spatially resolved X-ray absorption spectroscopy." Catal. Today **145**(3): 267-278.

Grunwaldt, J.-D. and C. G. Schroer (2010). "Hard and soft X-ray microscopy and tomography in catalysis: bridging the different time and length scales." Chem. Soc. Rev. **39**(12): 4741-4753.

Grunwaldt, J.-D., J. B. Wagner and R. E. Dunin-Borkowski (2013). "Imaging Catalysts at Work: A Hierarchical Approach from the Macro- to the Meso- and Nano-scale." ChemCatChem **5**(1): 62-80.

Grunwaldt, J. D. and B. S. Clausen (2002). "Combining XRD and EXAFS with on-line catalytic studies for in situ characterization of catalysts." Top. Catal. **18**(1-2): 37-43.

Guizar-Sicairos, M., A. Diaz, M. Holler, M. S. Lucas, A. Menzel, R. A. Wepf and O. Bunk (2011). "Phase tomography from x-ray coherent diffractive imaging projections." Opt. Express **19**(22): 21345-21357.

Guizar-Sicairos, M., S. T. Thurman and J. R. Fienup (2008). "Efficient subpixel image registration algorithms." Opt. Lett. **33**(2): 156-158.

Güttel, R. (2015). "Structuring of Reactors and Catalysts on Multiple Scales: Potential and Limitations for Fischer-Tropsch Synthesis." Chem. Ing. Tech. **87**(6): 694-701.

Hansen, T. W., A. T. DeLaRiva, S. R. Challa and A. K. Datye (2013). "Sintering of Catalytic Nanoparticles: Particle Migration or Ostwald Ripening?" Acc. Chem. Res. **46**(8): 1720-1730.

Hansen, T. W., J. B. Wagner and R. E. Dunin-Borkowski (2010). "Aberration corrected and monochromated environmental transmission electron microscopy: challenges and prospects for materials science." Mater. Sci. Technol. **26**(11): 1338-1344.

Haw, J. F. (2002). In-Situ Spectroscopy in Heterogeneous Catalysis. Weinheim, Wiley-VCH.

Hayashida, M. and M. Malac (2016). "Practical electron tomography guide: Recent progress and future opportunities." Micron **91**: 49-74.

He, X., Y. Wang, X. Zhang, M. Dong, G. Wang, B. Zhang, Y. Niu, S. Yao, X. He and H. Liu (2019). "Controllable in Situ Surface Restructuring of Cu Catalysts and Remarkable Enhancement of Their Catalytic Activity." ACS Catalysis **9**(3): 2213-2221.

Hémonnot, C. Y. J., J. Reinhardt, O. Saldanha, J. Patommel, R. Graceffa, B. Weinhausen, M. Burghammer, C. G. Schroer and S. Köster (2016). "X-rays Reveal the Internal Structure of Keratin Bundles in Whole Cells." ACS Nano **10**(3): 3553-3561.

Herzing, A. A., C. J. Kiely, A. F. Carley, P. Landon and G. J. Hutchings (2008). "Identification of Active Gold Nanoclusters on Iron Oxide Supports for CO Oxidation." Science **321**(5894): 1331-1335.

Hirose, M., N. Ishiguro, K. Shimomura, N. Burdet, H. Matsui, M. Tada and Y. Takahashi (2018). "Visualization of Heterogeneous Oxygen Storage Behavior in Platinum-Supported Cerium-Zirconium Oxide Three-Way Catalyst Particles by Hard X-ray Spectro-Ptychography." Angew. Chem. Int. Ed. **57**(6): 1474-1479.

Hirsch, P., A. Howie, R. B. Nicholson, D. W. Pashley and M. J. Whelan (1977). Electron Microscopy of Thin Crystals. New York, Robert E. Krieger Publishing**:** 2.

Hodge, A. M., J. Biener, L. L. Hsiung, Y. M. Wang, A. V. Hamza and J. H. Satcher (2005). "Monolithic nanocrystalline Au fabricated by the compaction of nanoscale foam." J. Mater. Res. **20**(3): 554-557.

Hodge, A. M., J. R. Hayes, J. A. Caro, J. Biener and A. V. Hamza (2006). "Characterization and Mechanical Behavior of Nanoporous Gold." Adv. Eng. Mater. **8**(9): 853-857.

Hofmann, S., R. Sharma, C. Ducati, G. Du, C. Mattevi, C. Cepek, M. Cantoro, S. Pisana, A. Parvez, F. Cervantes-Sodi, A. C. Ferrari, R. Dunin-Borkowski, S. Lizzit, L. Petaccia, A. Goldoni and J. Robertson (2007). "In situ Observations of Catalyst Dynamics during Surface-Bound Carbon Nanotube Nucleation." Nano Lett. **7**(3): 602-608.

Holler, M., A. Diaz, M. Guizar-Sicairos, P. Karvinen, E. Färm, E. Härkönen, M. Ritala, A. Menzel, J. Raabe and O. Bunk (2014). "X-ray ptychographic computed tomography at 16 nm isotropic 3D resolution." Sci. Rep. **4**: 3857.

Holler, M., M. Guizar-Sicairos, E. H. R. Tsai, R. Dinapoli, E. Müller, O. Bunk, J. Raabe and G. Aeppli (2017). "High-resolution non-destructive three-dimensional imaging of integrated circuits." Nature **543**(7645): 402-406.

Holler, M. and J. Raabe (2015). "Error motion compensating tracking interferometer for the position measurement of objects with rotational degree of freedom." Opt. Eng. **54**(5): 7.

Holler, M., J. Raabe, A. Diaz, M. Guizar-Sicairos, C. Quitmann, A. Menzel and O. Bunk (2012). "An instrument for 3D x-ray nano-imaging." Rev. Sci. Instrum. **83**(7): 073703.

Holler, M., J. Raabe, R. Wepf, S. H. Shahmoradian, A. Diaz, B. Sarafimov, T. Lachat, H. Walther and M. Vitins (2017). "OMNY PIN—A versatile sample holder for tomographic measurements at room and cryogenic temperatures." Rev. Sci. Instrum. **88**(11): 113701.

Holzer, L. and M. Cantoni (2012). Nanofabrication Using Focused Ion and Electron Beams: Principles and Applications. New York, Oxford University Press**:** 410.

Hoppe, R., J. Reinhardt, G. Hofmann, J. Patommel, J.-D. Grunwaldt, C. D. Damsgaard, G. Wellenreuther, G. Falkenberg and C. G. Schroer (2013). "High-resolution chemical imaging of gold nanoparticles using hard x-ray ptychography." Appl. Phys. Lett. **102**(20).

Høydalsvik, K., J. Bø Fløystad, T. Zhao, M. Esmaeili, A. Diaz, J. W. Andreasen, R. H. Mathiesen, M. Rønning and D. W. Breiby (2014). "In situ X-ray ptychography imaging of high-temperature CO2 acceptor particle agglomerates." Appl. Phys. Lett. **104**(24): 241909.

Huang, X., R. Conley, N. Bouet, J. Zhou, A. Macrander, J. Maser, H. Yan, E. Nazaretski, K. Lauer, R. Harder, I. K. Robinson, S. Kalbfleisch and Y. S. Chu (2015). "Achieving hard X-ray nanofocusing using a wedged multilayer Laue lens." Opt. Express **23**(10): 12496-12507.

Huang, X., R. Farra, R. Schlögl and M.-G. Willinger (2019). "Growth and Termination Dynamics of Multiwalled Carbon Nanotubes at Near Ambient Pressure: An in Situ Transmission Electron Microscopy Study." Nano Lett. **19**(8): 5380-5387.

Huang, X., H. Yan, R. Harder, Y. Hwu, I. K. Robinson and Y. S. Chu (2014). "Optimization of overlap uniformness for ptychography." Opt. Express **22**(10): 12634-12644.

Huang, Z. (2004). "Combining Ar ion milling with FIB lift-out techniques to prepare high quality site-specific TEM samples." J. Microsc. **215**(3): 219-223.

Huber, R., G. Haberfehlner, M. Holler, G. Kothleitner and K. Bredies (2019). "Total generalized variation regularization for multi-modal electron tomography." Nanoscale **11**(12): 5617-5632.

Humphreys, J., R. Beanland and P. J. Goodhew (2001). Electron Microscopy and Analysis. New York, USA, Taylor & Francis.

Humphry, M. J., B. Kraus, A. C. Hurst, A. M. Maiden and J. M. Rodenburg (2012). "Ptychographic electron microscopy using high-angle dark-field scattering for sub-nanometre resolution imaging." Nat. Commun. **3**(1): 730.

Ianiro, A., H. Wu, M. M. J. van Rijt, M. P. Vena, A. D. A. Keizer, A. C. C. Esteves, R. Tuinier, H. Friedrich, N. A. J. M. Sommerdijk and J. P. Patterson (2019). "Liquid–liquid phase separation during amphiphilic self-assembly." Nat. Chem. **11**(4): 320-328.

Ihli, J., A. Diaz, Y. Shu, M. Guizar-Sicairos, M. Holler, K. Wakonig, M. Odstrcil, T. Li, F. Krumeich, E. Müller, W.-C. Cheng, J. Anton van Bokhoven and A. Menzel (2018). "Resonant Ptychographic Tomography Facilitates Three-Dimensional Quantitative Colocalization of Catalyst Components and Chemical Elements." J. Phys. Chem. C **122**(40): 22920-22929.

Ihli, J., R. R. Jacob, M. Holler, M. Guizar-Sicairos, A. Diaz, J. C. da Silva, D. Ferreira Sanchez, F. Krumeich, D. Grolimund, M. Taddei, W. C. Cheng, Y. Shu, A. Menzel and J. A. van Bokhoven (2017). "A three-dimensional view of structural changes caused by deactivation of fluid catalytic cracking catalysts." Nat. Commun. **8**(1): 809.

Jeangros, Q., A. Faes, J. B. Wagner, T. W. Hansen, U. Aschauer, J. Van herle, A. Hessler-Wyser and R. E. Dunin-Borkowski (2010). "In situ redox cycle of a nickel–YSZ fuel cell anode in an environmental transmission electron microscope." Acta Mater. **58**(14): 4578-4589.

JEOL. (2019). "Transmission Electron Microscope (TEM)." Retrieved 1 July 2019, from www.jeol.co.jp/en/science/em.html.

Jinschek, J. R. and S. Helveg (2012). "Image resolution and sensitivity in an environmental transmission electron microscope." Micron **43**(11): 1156-1168.

Jr., J. D. C., M. Phaneuf, C. Chandler, M. Megorden, K. E. Noll, R. Schuman, T. J. Gannon, A. Krechmer, D. Monforte, N. Antoniou, N. Bassom, J. Li, P. Carleson and C. Huynh (2002). "Copper device editing: Strategy for focused ion beam milling of copper." J. Vac. Sci. Technol. B **20**(6): 2682-2685.

Kalirai, S., U. Boesenberg, G. Falkenberg, F. Meirer and B. M. Weckhuysen (2015). "X-ray Fluorescence Tomography of Aged Fluid-Catalytic-Cracking Catalyst Particles Reveals Insight into Metal Deposition Processes." ChemCatChem **7**(22): 3674-3682.

Kalz, K. F., R. Kraehnert, M. Dvoyashkin, R. Dittmeyer, R. Gläser, U. Krewer, K. Reuter and J.-D. Grunwaldt (2017). "Future Challenges in Heterogeneous Catalysis: Understanding Catalysts under Dynamic Reaction Conditions." ChemCatChem **9**(1): 17-29.

Kamino, T., T. Yaguchi, Y. Kuroda, T. Ohnishi, T. Ishitani, Y. Miyahara and Z. Horita (2004). "Evaluation of TEM samples of an Mg-Al alloy prepared using FIB milling at the operating voltages of 10 kV and 40 kV." Microscopy **53**(5): 459-463.

Kato, N. I. (2004). "Reducing focused ion beam damage to transmission electron microscopy samples." Microscopy **53**(5): 451-458.

Kawasaki, T., Y. Takai and R. Shimizu (2001). "Distorted surface and interface structures of catalytic gold nanoparticles observed by spherical aberration-free phase electron microscopy." Appl. Phys. Lett. **79**(21): 3509-3511.

Ketchie, W. C., Y.-L. Fang, M. S. Wong, M. Murayama and R. J. Davis (2007). "Influence of gold particle size on the aqueous-phase oxidation of carbon monoxide and glycerol." J. Catal. **250**(1): 94-101.

Kirk, E. C., D. A. Williams and H. Ahmed (1989). "Cross-sectional transmission electron microscopy of precisely selected regions from semiconductor devices." Inst. Phys. Conf. Series **100**: 501.

Kirkland, A., L.-Y. Chang, S. Haigh and C. Hetherington (2008). "Transmission electron microscopy without aberrations: Applications to materials science." Curr. Appl. Phys. **8**(3): 425-428.

Klumpp, M., L. Zeng, S. A. Al-Thabaiti, A. P. Weber and W. Schwieger (2016). "Building concept inspired by raspberries: From microporous zeolite nanocrystals to hierarchically porous assemblies." Microporous Mesoporous Mater. **229**: 155-165.

Koneti, S., L. Roiban, F. Dalmas, C. Langlois, A.-S. Gay, A. Cabiac, T. Grenier, H. Banjak, V. Maxim and T. Epicier (2019). "Fast electron tomography: Applications to beam sensitive samples and in situ TEM or operando environmental TEM studies." Mater. Charact. **151**: 480-495.

Kooyman, P. J., J. G. Buglass, H. R. Reinhoudt, A. D. van Langeveld, E. J. M. Hensen, H. W. Zandbergen and J. A. R. van Veen (2002). "Quasi in Situ Sequential Sulfidation of CoMo/Al2O3 Studied Using High-Resolution Electron Microscopy." J. Phys. Chem. B **106**(45): 11795-11799.

Koster, A. J., U. Ziese, A. J. Verkleij, A. H. Janssen and K. P. de Jong (2000). "Three-Dimensional Transmission Electron Microscopy: A Novel Imaging and Characterization Technique with Nanometer Scale Resolution for Materials Science." J. Phys. Chem. B **104**(40): 9368-9370.

Kosuda, K. M., A. Wittstock, C. M. Friend and M. Bäumer (2012). "Oxygen-Mediated Coupling of Alcohols over Nanoporous Gold Catalysts at Ambient Pressures." Angew. Chem. Int. Ed. **51**(7): 1698-1701.

Kraft, P., A. Bergamaschi, C. Broennimann, R. Dinapoli, E. F. Eikenberry, B. Henrich, I. Johnson, A. Mozzanica, C. M. Schleputz, P. R. Willmott and B. Schmitt (2009). "Performance of single-photon-counting PILATUS detector modules." J. Synchrotron Radiat. **16**(3): 368-375.

Krivanek, O. L., M. F. Chisholm, V. Nicolosi, T. J. Pennycook, G. J. Corbin, N. Dellby, M. F. Murfitt, C. S. Own, Z. S. Szilagyi, M. P. Oxley, S. T. Pantelides and S. J. Pennycook (2010). "Atom-by-atom structural and chemical analysis by annular dark-field electron microscopy." Nature **464**(7288): 571-574.

Krumeich, F., J. Ihli, Y. Shu, W.-C. Cheng and J. A. van Bokhoven (2018). "Structural Changes in Deactivated Fluid Catalytic Cracking Catalysts Determined by Electron Microscopy." ACS Catal. **8**(5): 4591-4599.

Kupsch, A., A. Lange, M. P. Hentschel, S. Lueck, V. Schmidt, R. Grothausmann, A. Hilger and I. Manke (2016). "Missing wedge computed tomography by iterative algorithm DIRECTT." J. Microsc. **261**(1): 36-45.

Lackmann, A., M. Bäumer, G. Wittstock and A. Wittstock (2018). "Independent control over residual silver content of nanoporous gold by galvanodynamically controlled dealloying." Nanoscale **10**(36): 17166-17173.

Larsson, E., D. Gursoy, F. De Carlo, E. Lilleodden, M. Storm, F. Wilde, K. Hu, M. Muller and I. Greving (2019). "Nanoporous gold: a hierarchical and multiscale 3D test pattern for characterizing X-ray nano-tomography systems." J. Synchrotron Radiat. **26**(1): 194-204.

Li, J. (2012). Advanced Techniques in TEM Specimen Preparation. The Transmission Electron Microscope. K. Maaz. London, UK, IntechOpen: 69-84.

Li, K. and D. W. Reeve (2005). "Sample Contamination in Analysis of Wood Pulp Fibers with X-ray Photoelectron Spectroscopy." J. Wood Chem. Tech. **24**(3): 183-200.

Li, T., J. Ihli, Z. Ma, F. Krumeich and J. A. van Bokhoven (2019). "Composition and Structure Dependent Mesopore/Macropore Formation in Zeolites by Desilication." J. Phys. Chem. C **123**(14): 8793-8801.

Li, Z., J. Luo, X. Tan, Q. Fang, Y. Zeng, M. Zhou, W. Wu and J. Zhang (2017). "X-ray nanotomography characterizations of gold foams." Mater. Lett. **205**: 215-218.

Liu, H. W., R. Nishitani, T. Fujita, W. Li, L. Zhang, X. Y. Lang, P. Richard, K. S. Nakayama, X. Chen, M. W. Chen and Q. K. Xue (2014). "Inelastic electron-tunneling spectroscopy of nanoporous gold films." Phys. Rev. B **89**(3): 035426.

Liu, Y., F. Meirer, C. M. Krest, S. Webb and B. M. Weckhuysen (2016). "Relating structure and composition with accessibility of a single catalyst particle using correlative 3-dimensional micro-spectroscopy." Nat. Commun. **7**: 12634.

Lu, Y., W.-J. Yin, K.-L. Peng, K. Wang, Q. Hu, A. Selloni, F.-R. Chen, L.-M. Liu and M.-L. Sui (2018). "Self-hydrogenated shell promoting photocatalytic H2 evolution on anatase TiO2." Nat. Commun. **9**(1): 2752.

Machoke, A. G., A. M. Beltrán, A. Inayat, B. Winter, T. Weissenberger, N. Kruse, R. Güttel, E. Spiecker and W. Schwieger (2015). "Micro/Macroporous System: MFI-Type Zeolite Crystals with Embedded Macropores." Adv. Mater. **27**(6): 1066-1070.

Madejski, G., K. Lucas, F. C. Pascut, K. F. Webb and J. L. McGrath (2018). "TEM Tomography of Pores with Application to Computational Nanoscale Flows in Nanoporous Silicon Nitride (NPN)." Membranes **8**(2): 26.

Mahr, C., P. Kundu, A. Lackmann, D. Zanaga, K. Thiel, M. Schowalter, M. Schwan, S. Bals, A. Wittstock and A. Rosenauer (2017). "Quantitative determination of residual silver distribution in nanoporous gold and its influence on structure and catalytic performance." J. Catal. **352**: 52-58.

Maiden, A. M. and J. M. Rodenburg (2009). "An improved ptychographical phase retrieval algorithm for diffractive imaging." Ultramicroscopy **109**(10): 1256-1262.

Malm, J. O. and M. A. O'Keefe (1997). "Deceptive “lattice spacings” in high-resolution micrographs of metal nanoparticles." Ultramicroscopy **68**(1): 13-23.

Mangipudi, K. R., V. Radisch, L. Holzer and C. A. Volkert (2016). "A FIB-nanotomography method for accurate 3D reconstruction of open nanoporous structures." Ultramicroscopy **163**: 38-47.

Marks, L. D. (1983). "Direct Imaging of Carbon-Covered and Clean Gold (110) Surfaces." Phys. Rev. Lett. **51**(11): 1000-1002.

Marks, L. D. and D. J. Smith (1983). "Direct surface imaging in small metal particles." Nature **303**(5915): 316-317.

Matera, S. and K. Reuter (2012). "When atomic-scale resolution is not enough: Spatial effects on in situ model catalyst studies." J. Catal. **295**: 261-268.

Mayer, J., L. A. Giannuzzi, T. Kamino and J. Michael (2007). "TEM Sample Preparation and FIB-Induced Damage." MRS Bull. **32**(5): 400-407.

Meirer, F., J. Cabana, Y. Liu, A. Mehta, J. C. Andrews and P. Pianetta (2011). "Three-dimensional imaging of chemical phase transformations at the nanoscale with full-field transmission X-ray microscopy." J. Synchrotron Radiat. **18**(5): 773-781.

Meirer, F., D. T. Morris, S. Kalirai, Y. Liu, J. C. Andrews and B. M. Weckhuysen (2015). "Mapping Metals Incorporation of a Whole Single Catalyst Particle Using Element Specific X-ray Nanotomography." J. Am. Chem. Soc. **137**(1): 102-105.

Meirer, F. and B. M. Weckhuysen (2018). "Spatial and temporal exploration of heterogeneous catalysts with synchrotron radiation." Nat. Rev. Mater. **3**(9): 324-340.

Méndez-Vilas, A. and J. Díaz (2010). Microscopy : science, technology, applications and education. Badajoz, Spain, Formatex Research Center.

Meng-Burany, X. (2010). Analysis of Electroplated Films Using Dual-Beam FIB/SEM and TEM Techniques. Modern Electroplating, John Wiley & Sons, Inc.**:** 637-663.

Messaoudii, C., T. Boudier, C. O. Sanchez Sorzano and S. Marco (2007). "TomoJ: tomography software for three-dimensional reconstruction in transmission electron microscopy." BMC Bioinformatics **8**: 288-288.

Miao, J., P. Ercius and S. J. L. Billinge (2016). "Atomic electron tomography: 3D structures without crystals." Science **353**(6306).

Midgley, P. A. and R. E. Dunin-Borkowski (2009). "Electron tomography and holography in materials science." Nat. Mater. **8**: 271.

Midgley, P. A., E. P. W. Ward, A. B. Hungria and J. M. Thomas (2007). "Nanotomography in the chemical, biological and materials sciences." Chem. Soc. Rev. **36**(9): 1477-1494.

Mimura, H., S. Handa, T. Kimura, H. Yumoto, D. Yamakawa, H. Yokoyama, S. Matsuyama, K. Inagaki, K. Yamamura, Y. Sano, K. Tamasaku, Y. Nishino, M. Yabashi, T. Ishikawa and K. Yamauchi (2010). "Breaking the 10 nm barrier in hard-X-ray focusing." Nat. Phys. **6**(2): 122-125.

Mishra, A. K., C. Bansal and H. Hahn (2008). "Surface charge induced variation in the electrical conductivity of nanoporous gold." J. Appl. Phys. **103**(9): 094308.

Molina-Luna, L., S. Wang, Y. Pivak, A. Zintler, H. H. Pérez-Garza, R. G. Spruit, Q. Xu, M. Yi, B.-X. Xu and M. Acosta (2018). "Enabling nanoscale flexoelectricity at extreme temperature by tuning cation diffusion." Nat. Commun. **9**(1): 4445.

Munroe, P. R. (2009). "The application of focused ion beam microscopy in the material sciences." Mater. Charact. **60**(1): 2-13.

Nelson, J., S. Misra, Y. Yang, A. Jackson, Y. Liu, H. Wang, H. Dai, J. C. Andrews, Y. Cui and M. F. Toney (2012). "In Operando X-ray Diffraction and Transmission X-ray Microscopy of Lithium Sulfur Batteries." J. Am. Chem. Soc. **134**(14): 6337-6343.

Nelson Weker, J. and M. F. Toney (2015). "Emerging In Situ and Operando Nanoscale X-Ray Imaging Techniques for Energy Storage Materials." Adv. Funct. Mater. **25**(11): 1622-1637.

Neusser, G., S. Eppler, J. Bowen, C. J. Allender, P. Walther, B. Mizaikoff and C. Kranz (2017). "FIB and MIP: understanding nanoscale porosity in molecularly imprinted polymers via 3D FIB/SEM tomography." Nanoscale **9**(38): 14327-14334.

Newton, M. A. (2017). "Time Resolved Operando X-ray Techniques in Catalysis, a Case Study: CO Oxidation by O2 over Pt Surfaces and Alumina Supported Pt Catalysts." Catalysts **7**(2): 58.

Ng, K. M., R. Gani and K. Dam-Johansen (2006). Chemical Product Design: Towards a Perspective through Case Studies, Elsevier.

Nicoletti, O., F. de la Peña, R. K. Leary, D. J. Holland, C. Ducati and P. A. Midgley (2013). "Three-dimensional imaging of localized surface plasmon resonances of metal nanoparticles." Nature **502**: 80.

Niehle, M. and A. Trampert (2015). "Electron tomography on nanopores embedded in epitaxial GaSb thin films." Micron **73**: 54-62.

Niemantsverdriet, J. W. (2007). Spectroscopy in Catalysis - An Introduction. Weinheim, Wiley-VCH.

Odstrcil, M., M. Holler, J. Raabe and M. Guizar-Sicairos (2018). "High resolution 3D imaging of integrated circuits by x-ray ptychography." Proc. SPIE **10656**: 10656OU.

Padgett, E., R. Hovden, J. C. DaSilva, B. D. A. Levin, J. L. Grazul, T. Hanrath and D. A. Muller (2017). "A Simple Preparation Method for Full-Range Electron Tomography of Nanoparticles and Fine Powders." Microsc. Microanal. **23**(6): 1150-1158.

Pfeiffer, F. (2018). "X-ray ptychography." Nat. Photonics **12**(1): 9-17.

Piazza, V., B. Weinhausen, A. Diaz, C. Dammann, C. Maurer, M. Reynolds, M. Burghammer and S. Köster (2014). "Revealing the Structure of Stereociliary Actin by X-ray Nanoimaging." ACS Nano **8**(12): 12228-12237.

Polavarapu, L., D. Zanaga, T. Altantzis, S. Rodal-Cedeira, I. Pastoriza-Santos, J. Pérez-Juste, S. Bals and L. M. Liz-Marzán (2016). "Galvanic Replacement Coupled to Seeded Growth as a Route for Shape-Controlled Synthesis of Plasmonic Nanorattles." J. Am. Chem. Soc. **138**(36): 11453-11456.

Przybilla, T., B. A. Zubiri, A. M. Beltrán, B. Butz, A. G. F. Machoke, A. Inayat, M. Distaso, W. Peukert, W. Schwieger and E. Spiecker (2018). "Transfer of Individual Micro- and Nanoparticles for High-Precision 3D Analysis Using 360° Electron Tomography." Small Methods **2**(1): 1700276.

Pyrz, W. D., D. A. Blom, T. Vogt and D. J. Buttrey (2008). "Direct Imaging of the MoVTeNbO M1 Phase Using An Aberration-Corrected High-Resolution Scanning Transmission Electron Microscope." Angew. Chem. Int. Ed. **47**(15): 2788-2791.

Qadir, K., B. T. P. Quynh, H. Lee, S. Y. Moon, S. H. Kim and J. Y. Park (2015). "Tailoring metal–oxide interfaces of inverse catalysts of TiO2/nanoporous-Au under hydrogen oxidation." Chem. Commun. **51**(47): 9620-9623.

Radermacher, M. (1988). "Three-Dimensional reconstruction of single particles from random and nonrandom tilt series." J. Electron Microsc. Tech. **9**(4): 359-394.

Radon, J. (1986). "On the determination of functions from their integral values along certain manifolds." IEEE Trans. Med. Imag. **5**(4): 170-176.

Ramachandramoorthy, R., R. Bernal and H. D. Espinosa (2015). "Pushing the Envelope of In Situ Transmission Electron Microscopy." ACS Nano **9**(5): 4675-4685.

Ren, G. Q., Y. Tang, K. P. Liu, Y. Su, S. Miao, W. Liu, W. M. Cong, X. D. Wang, W. Z. Li, J. Li and T. Zhang (2018). "Exceptional Antisintering Gold Nanocatalyst for Diesel Exhaust Oxidation." Nano. Lett. **18**(10): 6489-6493.

Rodenburg, J. M., A. C. Hurst, A. G. Cullis, B. R. Dobson, F. Pfeiffer, O. Bunk, C. David, K. Jefimovs and I. Johnson (2007). "Hard-X-Ray Lensless Imaging of Extended Objects." Phys. Rev. Lett. **98**(3): 034801.

Roiban, L., S. Li, M. Aouine, A. Tuel, D. Farrusseng and T. Epicier (2018). "Fast 'Operando' electron nanotomography." J. Microsc. **269**(2): 117-126.

Rösner, H., S. Parida, D. Kramer, C. A. Volkert and J. Weissmüller (2007). "Reconstructing a Nanoporous Metal in Three Dimensions: An Electron Tomography Study of Dealloyed Gold Leaf." Adv. Eng. Mater. **9**(7): 535-541.

Saghi, Z., D. J. Holland, R. Leary, A. Falqui, G. Bertoni, A. J. Sederman, L. F. Gladden and P. A. Midgley (2011). "Three-Dimensional Morphology of Iron Oxide Nanoparticles with Reactive Concave Surfaces. A Compressed Sensing-Electron Tomography (CS-ET) Approach." Nano Letters **11**(11): 4666-4673.

Sala, S., V. S. C. Kuppili, S. Chalkidis, D. J. Batey, X. Shi, C. Rau and P. Thibault (2018). "Multiscale X-ray imaging using ptychography." J. Synchrotron Radiat. **25**(4): 1214-1221.

Schindelin, J., I. Arganda-Carreras, E. Frise, V. Kaynig, M. Longair, T. Pietzsch, S. Preibisch, C. Rueden, S. Saalfeld, B. Schmid, J.-Y. Tinevez, D. J. White, V. Hartenstein, K. Eliceiri, P. Tomancak and A. Cardona (2012). "Fiji: an open-source platform for biological-image analysis." Nat. Methods **9**: 676.

Schroer, C. G., I. Agapov, W. Brefeld, R. Brinkmann, Y.-C. Chae, H.-C. Chao, M. Eriksson, J. Keil, X. Nuel Gavalda, R. Rohlsberger, O. H. Seeck, M. Sprung, M. Tischer, R. Wanzenberg and E. Weckert (2018). "PETRA IV: the ultralow-emittance source project at DESY." J. Synchrotron Radiat. **25**(5): 1277-1290.

Schroer, C. G., P. Boye, J. M. Feldkamp, J. Patommel, A. Schropp, A. Schwab, S. Stephan, M. Burghammer, S. Schöder and C. Riekel (2008). "Coherent X-Ray Diffraction Imaging with Nanofocused Illumination." Phys. Rev. Lett. **101**(9): 090801.

Schroer, C. G., P. Cloetens, M. Rivers, A. Snigirev, A. Takeuchi and W. Yun (2004). "High-Resolution 3D Imaging Microscopy Using Hard X-Rays." MRS Bull. **29**(3): 157-165.

Schroer, C. G. and J.-D. Grunwaldt (2009). "X-ray Absorption Spectroscopic Microscopy: From the Micro- to the Nanoscale." Synchrotron Radiat. News **22**(2): 23-28.

Schroer, C. G., M. Kuhlmann, T. F. Günzler, B. Lengeler, M. Richwin, B. Griesebock, D. Lützenkirchen-Hecht, R. Frahm, E. Ziegler, A. Mashayekhi, D. R. Haeffner, J.-D. Grunwaldt and A. Baiker (2003). "Mapping the chemical states of an element inside a sample using tomographic x-ray absorption spectroscopy." Appl. Phys. Lett. **82**(19): 3360-3362.

Schroer, C. G., M. Kuhlmann, S. V. Roth, R. Gehrke, N. Stribeck, A. Almendarez-Camarillo and B. Lengeler (2006). "Mapping the local nanostructure inside a specimen by tomographic small-angle x-ray scattering." Appl. Phys. Lett. **88**(16): 164102.

Schroer, C. G., M. Seyrich, M. Kahnt, S. Botta, R. Döhrmann, G. Falkenberg, J. Garrevoet, M. Lyubomirskiy, M. Scholz, A. Schropp and F. Wittwer (2017). PtyNAMi: Ptychographic nano-analytical microscope at PETRA III - Interferometrically tracking positions for 3D x-ray scanning microscopy using a ball-lens retroreflector. SPIE Optical Engineering + Applications, San Diego, California, USA, SPIE.

Schropp, A., P. Boye, A. Goldschmidt, S. Hönig, R. Hoppe, J. Patommel, C. Rakete, D. Samberg, S. Stephan, S. Schöder, M. Burghammer and C. G. Schröer (2011). "Non-destructive and quantitative imaging of a nano-structured microchip by ptychographic hard X-ray scanning microscopy." J. Microsc. **241**(1): 9-12.

Schropp, A., R. Hoppe, J. Patommel, D. Samberg, F. Seiboth, S. Stephan, G. Wellenreuther, G. Falkenberg and C. G. Schroer (2012). "Hard x-ray scanning microscopy with coherent radiation: Beyond the resolution of conventional x-ray microscopes." Appl. Phys. Lett. **100**(25): 253112.

Schwieger, W., A. G. Machoke, T. Weissenberger, A. Inayat, T. Selvam, M. Klumpp and A. Inayat (2016). "Hierarchy concepts: classification and preparation strategies for zeolite containing materials with hierarchical porosity." Chem. Soc. Rev. **45**(12): 3353-3376.

Scientific, T. F. (2019). "Gallium Liquid Metal Ion Source Handling and Operating Instructions." Retrieved 1 July 2019, from https://www.fei.com/products/components/electron-ion-sources.

SCM. (2019). "ReaxPro: Mulitscale Modeling Software for Reactive Materials." Retrieved 2 October 2019, from https://www.scm.com/about-us/eu-projects/reaxpro-multiscalereactormodeling/.

Scott, M. C., C.-C. Chen, M. Mecklenburg, C. Zhu, R. Xu, P. Ercius, U. Dahmen, B. C. Regan and J. Miao (2012). "Electron tomography at 2.4-ångström resolution." Nature **483**: 444.

Seiboth, F., A. Schropp, M. Scholz, F. Wittwer, C. Rödel, M. Wünsche, T. Ullsperger, S. Nolte, J. Rahomäki, K. Parfeniukas, S. Giakoumidis, U. Vogt, U. Wagner, C. Rau, U. Boesenberg, J. Garrevoet, G. Falkenberg, E. C. Galtier, H. Ja Lee, B. Nagler and C. G. Schroer (2017). "Perfect X-ray focusing via fitting corrective glasses to aberrated optics." Nat. Commun. **8**.

Shi, J., C. Mahr, M. M. Murshed, T. M. Gesing, A. Rosenauer, M. Bäumer and A. Wittstock (2017). "Steam reforming of methanol over oxide decorated nanoporous gold catalysts: a combined in situ FTIR and flow reactor study." Phys. Chem. Chem. Phys. **19**(13): 8880-8888.

Shi, J., C. Mahr, M. M. Murshed, V. Zielasek, A. Rosenauer, T. M. Gesing, M. Baumer and A. Wittstock (2016). "A versatile sol-gel coating for mixed oxides on nanoporous gold and their application in the water gas shift reaction." Catal. Sci. Technol. **6**(14): 5311-5319.

Shi, J., A. Schaefer, A. Wichmann, M. M. Murshed, T. M. Gesing, A. Wittstock and M. Bäumer (2014). "Nanoporous Gold-Supported Ceria for the Water–Gas Shift Reaction: UHV Inspired Design for Applied Catalysis." J. Phys. Chem. C **118**(50): 29270-29277.

Slater, T. J. A., A. Janssen, P. H. C. Camargo, M. G. Burke, N. J. Zaluzec and S. J. Haigh (2016). "STEM-EDX tomography of bimetallic nanoparticles: A methodological investigation." Ultramicroscopy **162**: 61-73.

Slater, T. J. A., A. Macedo, S. L. M. Schroeder, M. G. Burke, P. O'Brien, P. H. C. Camargo and S. J. Haigh (2014). "Correlating Catalytic Activity of Ag–Au Nanoparticles with 3D Compositional Variations." Nano Lett. **14**(4): 1921-1926.

Somorjai, G. A. and Y. Li (2010). Introduction to Surface Chemistry and Catalysis. Hoboken, John Wiley & Sons.

Song, Z. and Z.-H. Xie (2018). "A literature review of in situ transmission electron microscopy technique in corrosion studies." Micron **112**: 69-83.

Spolenak, R., L. Sauter and C. Eberl (2005). "Reversible orientation-biased grain growth in thin metal films induced by a focused ion beam." Scr. Mater. **53**(11): 1291-1296.

Stavitski, E. and B. M. Weckhuysen (2010). "Infrared and Raman imaging of heterogeneous catalysts." Chem. Soc. Rev. **39**(12): 4615-4625.

Stierle, A., T. F. Keller, H. Noei, V. Vonk and R. Roehlsberger (2016). "DESY NanoLab." J. Large-Scale Res. Fac. **2**(A76): 1-9.

Su, D. S., T. Jacob, T. W. Hansen, D. Wang, R. Schlögl, B. Freitag and S. Kujawa (2008). "Surface Chemistry of Ag Particles: Identification of Oxide Species by Aberration-Corrected TEM and by DFT Calculations." Angew. Chem. Int. Ed. **120**(27): 5083-5086.

Takahashi, Y., Y. Nishino, R. Tsutsumi, H. Kubo, H. Furukawa, H. Mimura, S. Matsuyama, N. Zettsu, E. Matsubara, T. Ishikawa and K. Yamauchi (2009). "High-resolution diffraction microscopy using the plane-wave field of a nearly diffraction limited focused x-ray beam." Phys. Rev. B **80**(5): 054103.

Tan, C., M. D. R. Kok, S. R. Daemi, D. J. L. Brett and P. R. Shearing (2019). "Three-dimensional image based modelling of transport parameters in lithium–sulfur batteries." Phys. Chem. Chem. Phys. **21**(8): 4145-4154.

Tan, Y. H., J. A. Davis, K. Fujikawa, N. V. Ganesh, A. V. Demchenko and K. J. Stine (2012). "Surface area and pore size characteristics of nanoporous gold subjected to thermal, mechanical, or surface modification studied using gas adsorption isotherms, cyclic voltammetry, thermogravimetric analysis, and scanning electron microscopy." J. Mater. Chem. **22**(14): 6733-6745.

Tanaka, M., K. Higashida, K. Kaneko, S. Hata and M. Mitsuhara (2008). "Crack tip dislocations revealed by electron tomography in silicon single crystal." Scr. Mater. **59**(8): 901-904.

Tanaka, N. (2008). "Present status and future prospects of spherical aberration corrected TEM/STEM for study of nanomaterials∗." Sci. Technol. Adv. Mat. **9**(1): 014111.

Tao, F. and P. A. Crozier (2016). "Atomic-Scale Observations of Catalyst Structures under Reaction Conditions and during Catalysis." Chem. Rev. **116**(6): 3487-3539.

Tao, F. and M. Salmeron (2011). "In Situ Studies of Chemistry and Structure of Materials in Reactive Environments." Science **331**(6014): 171-174.

Telari, K. A., B. R. Rogers, H. Fang, L. Shen, R. A. Weller and D. N. Braski (2002). "Characterization of platinum films deposited by focused ion beam-assisted chemical vapor deposition." J. Vac. Sci. Technol. B **20**(2): 590-595.

Thibault, P., M. Dierolf, O. Bunk, A. Menzel and F. Pfeiffer (2009). "Probe retrieval in ptychographic coherent diffractive imaging." Ultramicroscopy **109**(4): 338-343.

Thibault, P., M. Dierolf, A. Menzel, O. Bunk, C. David and F. Pfeiffer (2008). "High-Resolution Scanning X-ray Diffraction Microscopy." Science **321**(5887): 379-382.

Thibault, P. and M. Guizar-Sicairos (2012). "Maximum-likelihood refinement for coherent diffractive imaging." New J. Phys. **14**(6): 063004.

Thomas, J. M. and J.-C. Hernandez-Garrido (2009). "Probing Solid Catalysts under Operating Conditions: Electrons or X-rays?" Angew. Chem. Int. Ed. **48**(22): 3904-3907.

Topsøe, H. (2003). "Developments in operando studies and in situ characterization of heterogeneous catalysts." J. Catal. **216**(1-2): 155-164.

Torruella, P., R. Arenal, F. de la Peña, Z. Saghi, L. Yedra, A. Eljarrat, L. López-Conesa, M. Estrader, A. López-Ortega, G. Salazar-Alvarez, J. Nogués, C. Ducati, P. A. Midgley, F. Peiró and S. Estradé (2016). "3D Visualization of the Iron Oxidation State in FeO/Fe3O4 Core–Shell Nanocubes from Electron Energy Loss Tomography." Nano Lett. **16**(8): 5068-5073.

Tsen, S. C. Y., P. A. Crozier and J. Liu (2003). "Lattice measurement and alloy compositions in metal and bimetallic nanoparticles." Ultramicroscopy **98**(1): 63-72.

Van Aert, S., K. J. Batenburg, M. D. Rossell, R. Erni and G. Van Tendeloo (2011). "Three-dimensional atomic imaging of crystalline nanoparticles." Nature **470**(7334): 374-377.

Van den Brande, N., N. Patil, M. Guizar-Sicairos, R. Claessens, G. Van Assche, D. W. Breiby and B. Van Mele (2017). "Probing the bulk heterojunction morphology in thermally annealed active layers for polymer solar cells." Org. Electron. **41**: 319-326.

van der Walt, S., J. L. Schönberger, J. Nunez-Iglesias, F. Boulogne, J. D. Warner, N. Yager, E. Gouillart and T. Yu (2014). "scikit-image: image processing in Python." PeerJ **2**: e453.

van Heel, M. and M. Schatz (2005). "Fourier shell correlation threshold criteria." J. Struct. Biol. **151**(3): 250-262.

Van Riessen, A., W. D. A. Rickard, R. P. Williams and G. A. Van Riessen (2017). "Methods for geopolymer formulation development and microstructural analysis." J. Ceram. Sci. Technol. **8**(3): 421-431.

Vantomme, A., A. Léonard, Z.-Y. Yuan and B.-L. Su (2007). "Self-formation of hierarchical micro-meso-macroporous structures: Generation of the new concept “Hierarchical Catalysis”." Colloids Surf. A **300**(1): 70-78.

Venkatakrishnan, S. V., L. F. Drummy, M. A. Jackson, M. D. Graef, J. Simmons and C. A. Bouman (2013). "A Model Based Iterative Reconstruction Algorithm For High Angle Annular Dark Field-Scanning Transmission Electron Microscope (HAADF-STEM) Tomography." IEEE Trans. Image Process **22**(11): 4532-4544.

Vila-Comamala, J., A. Diaz, M. Guizar-Sicairos, A. Mantion, C. M. Kewish, A. Menzel, O. Bunk and C. David (2011). "Characterization of high-resolution diffractive X-ray optics by ptychographic coherent diffractive imaging." Opt. Express **19**(22): 21333-21344.

Volkert, C. A. and A. M. Minor (2007). "Focused Ion Beam Microscopy and Micromachining." MRS Bull. **32**(5): 389-399.

Wagner, J. B., F. Cavalca, C. D. Damsgaard, L. D. L. Duchstein and T. W. Hansen (2012). "Exploring the environmental transmission electron microscope." Micron **43**(11): 1169-1175.

Wang, Y.-C., T. J. A. Slater, G. M. Leteba, A. M. Roseman, C. P. Race, N. P. Young, A. I. Kirkland, C. I. Lang and S. J. Haigh (2019). "Imaging Three-Dimensional Elemental Inhomogeneity in Pt–Ni Nanoparticles Using Spectroscopic Single Particle Reconstruction." Nano Lett. **19**(2): 732-738.

Wang, Z., T. Kato, T. Hirayama, N. Kato, K. Sasaki and H. Saka (2005). "Surface damage induced by focused-ion-beam milling in a Si/Si p–n junction cross-sectional specimen." Appl. Surf. Sci. **241**(1): 80-86.

Weckhuysen, B. M. (2002). "Snapshots of a working catalyst: Possibilities and limitations of in situ spectroscopy in the field of heterogeneous catalysis." Chem. Commun. **2**(2): 97-110.

Weckhuysen, B. M. (2004). In-situ Spectroscopy of Catalysts, American Scientific Publishers.

Weckhuysen, B. M. (2009). "Chemical imaging of spatial heterogeneities in catalytic solids at different length and time scales." Angew. Chem. Int. Ed. **48**(27): 4910-4943.

Weker, J. N., X. Huang and M. F. Toney (2016). "In situ X-ray-based imaging of nano materials." Curr. Opin. Chem. Eng. **12**: 14-21.

Weyland, M. and P. A. Midgley (2004). "Electron tomography." Mater. Today **7**(12): 32-40.

Whiting, G. T., F. Meirer and B. M. Weckhuysen (2017). Operando EXAFS and XANES of Catalytic Solids and Related Materials. I. Yasuhiro, A. Kiyotaka and T. Mizuki. Berlin, Springer.

Wichmann, A., M. Bäumer and A. Wittstock (2015). "Oxidative Coupling of Alcohols and Amines over Bimetallic Unsupported Nanoporous Gold: Tailored Activity through Mechanistic Predictability." ChemCatChem **7**(1): 70-74.

Wichmann, A., A. Wittstock, K. Frank, M. M. Biener, B. Neumann, L. Mädler, J. Biener, A. Rosenauer and M. Bäumer (2013). "Maximizing Activity and Stability by Turning Gold Catalysis Upside Down: Oxide Particles on Nanoporous Gold." ChemCatChem **5**(7): 2037-2043.

Winter, D. A. M. d. and J. J. L. Mulders (2007). "Redeposition characteristics of focused ion beam milling for nanofabrication." J. Vac. Sci. Technol. B **25**(6): 2215-2218.

Wise, A. M., J. N. Weker, S. Kalirai, M. Farmand, D. A. Shapiro, F. Meirer and B. M. Weckhuysen (2016). "Nanoscale Chemical Imaging of an Individual Catalyst Particle with Soft X-ray Ptychography." ACS Catal. **6**(4): 2178-2181.

Wittstock, A. and M. Bäumer (2014). "Catalysis by Unsupported Skeletal Gold Catalysts." Acc. Chem. Res. **47**(3): 731-739.

Wittstock, A., J. Biener and M. Baumer (2010). "Nanoporous gold: a new material for catalytic and sensor applications." Phys. Chem. Chem. Phys. **12**(40): 12919-12930.

Wittstock, A., A. Wichmann and M. Bäumer (2012). "Nanoporous Gold as a Platform for a Building Block Catalyst." ACS Catal. **2**(10): 2199-2215.

Wittstock, A., V. Zielasek, J. Biener, C. M. Friend and M. Bäumer (2010). "Nanoporous Gold Catalysts for Selective Gas-Phase Oxidative Coupling of Methanol at Low Temperature." Science **327**(5963): 319-322.

Xia, R., J. L. Wang, R. Wang, X. Li, X. Zhang, X.-Q. Feng and Y. Ding (2010). "Correlation of the thermal and electrical conductivities of nanoporous gold." Nanotechnology **21**(8): 085703.

Xu, C., J. Su, X. Xu, P. Liu, H. Zhao, F. Tian and Y. Ding (2007). "Low Temperature CO Oxidation over Unsupported Nanoporous Gold." J. Am. Chem. Soc. **129**(1): 42-43.

Xu, M., Y. Sui, G. Xiao, X. Yang, Y. Wei and B. Zou (2017). "Kinetically controlled synthesis of nanoporous Au and its enhanced electrocatalytic activity for glucose-based biofuel cells." Nanoscale **9**(7): 2514-2520.

Xu, R., C.-C. Chen, L. Wu, M. C. Scott, W. Theis, C. Ophus, M. Bartels, Y. Yang, H. Ramezani-Dakhel, M. R. Sawaya, H. Heinz, L. D. Marks, P. Ercius and J. Miao (2015). "Three-dimensional coordinates of individual atoms in materials revealed by electron tomography." Nat. Mater. **14**: 1099.

Yaguchi, T., T. Kamino, T. Ishitani and R. Urao (1999). "Method for Cross-sectional Transmission Electron Microscopy Specimen Preparation of Composite Materials Using a Dedicated Focused Ion Beam System." Microsc. Microanal. **5**(5): 365-370.

Yaguchi, T., M. Suzuki, A. Watabe, Y. Nagakubo, K. Ueda and T. Kamino (2011). "Development of a high temperature-atmospheric pressure environmental cell for high-resolution TEM." J. Electron Microsc. **60**(3): 217-225.

Yan, H., R. Conley, N. Bouet and Y. S. Chu (2014). "Hard x-ray nanofocusing by multilayer Laue lenses." J. Phys. D **47**(26): 263001.

Yan, H., E. Nazaretski, K. Lauer, X. Huang, U. Wagner, C. Rau, M. Yusuf, I. Robinson, S. Kalbfleisch, L. Li, N. Bouet, J. Zhou, R. Conley and Y. S. Chu (2016). "Multimodality hard-x-ray imaging of a chromosome with nanoscale spatial resolution." Sci. Rep. **6**: 20112.

Yan, H., V. Rose, D. Shu, E. Lima, H. C. Kang, R. Conley, C. Liu, N. Jahedi, A. T. Macrander, G. B. Stephenson, M. Holt, Y. S. Chu, M. Lu and J. Maser (2011). "Two dimensional hard x-ray nanofocusing with crossed multilayer Laue lenses." Opt. Express **19**(16): 15069-15076.

Yedra, L., A. Eljarrat, J. M. Rebled, L. López-Conesa, N. Dix, F. Sánchez, S. Estradé and F. Peiró (2014). "EELS tomography in multiferroic nanocomposites: from spectrum images to the spectrum volume." Nanoscale **6**(12): 6646-6650.

Yeoh, C. S. M., D. Rossouw, Z. Saghi, P. Burdet, R. K. Leary and P. A. Midgley (2015). "The Dark Side of EDX Tomography: Modeling Detector Shadowing to Aid 3D Elemental Signal Analysis." Microsc. Microanal. **21**(3): 759-764.

Yokosawa, T., T. Alan, G. Pandraud, B. Dam and H. Zandbergen (2012). "In-situ TEM on (de)hydrogenation of Pd at 0.5–4.5bar hydrogen pressure and 20–400°C." Ultramicroscopy **112**(1): 47-52.

Yoshida, H., Y. Kuwauchi, J. R. Jinschek, K. Sun, S. Tanaka, M. Kohyama, S. Shimada, M. Haruta and S. Takeda (2012). "Visualizing Gas Molecules Interacting with Supported Nanoparticulate Catalysts at Reaction Conditions." Science **335**(6066): 317-319.

Zabihzadeh, S., J. Cugnoni, L. I. Duarte, S. Van Petegem and H. Van Swygenhoven (2017). "Deformation behavior of nano-porous polycrystalline silver. Part II: Simulations." Acta Mater. **131**: 564-573.

Zabihzadeh, S., S. Van Petegem, M. Holler, A. Diaz, L. I. Duarte and H. Van Swygenhoven (2017). "Deformation behavior of nanoporous polycrystalline silver. Part I: Microstructure and mechanical properties." Acta Mater. **131**: 467-474.

Zečević, J., K. P. de Jong and P. E. de Jongh (2013). "Progress in electron tomography to assess the 3D nanostructure of catalysts." Curr. Opin. Solid State Mater. Sci. **17**(3): 115-125.

Zhang, B., W. Zhang and D. S. Su (2011). "Towards a More Accurate Particle Size Distribution of Supported Catalyst by using HAADF-STEM." ChemCatChem **3**(6): 965-968.

Zhang, W., A. Trunschke, R. Schlögl and D. Su (2010). "Real-Space Observation of Surface Termination of a Complex Metal Oxide Catalyst." Angew. Chem. Int. Ed. **49**(35): 6084-6089.

Zhou, W., E. I. Ross-Medgaarden, W. V. Knowles, M. S. Wong, I. E. Wachs and C. J. Kiely (2009). "Identification of active Zr–WOx clusters on a ZrO2 support for solid acid catalysts." Nat. Chem. **1**(9): 722-728.

Zhu, C., R. Harder, A. Diaz, V. Komanicky, A. Barbour, R. Xu, X. Huang, Y. Liu, M. S. Pierce, A. Menzel and H. You (2015). "Ptychographic x-ray imaging of surfaces on crystal truncation rod." Appl. Phys. Lett. **106**(10): 101604.

Zielasek, V., B. Jurgens, C. Schulz, J. Biener, M. M. Biener, A. V. Hamza and M. Bäumer (2006). "Gold catalysts: nanoporous gold foams." Angew. Chem. Int. Ed. **45**(48): 8241-8244.

Ziese, U., A. H. Janssen, J.-L. Murk, W. J. C. Geerts, T. Van der Krift, A. J. Verkleij and A. J. Koster (2002). "Automated high-throughput electron tomography by pre-calibration of image shifts." J. Microsc. **205**(2): 187-200.

Zugic, B., S. Karakalos, K. J. Stowers, M. M. Biener, J. Biener, R. J. Madix and C. M. Friend (2016). "Continuous Catalytic Production of Methyl Acrylates from Unsaturated Alcohols by Gold: The Strong Effect of C═C Unsaturation on Reaction Selectivity." ACS Catal. **6**(3): 1833-1839.

Author Contributions

- Yakub Fam analysed all the data of ET, PXCT, FIB-SV, in situ XRP and limited-angle PXCT measurements (after ptychographic/tomographic reconstructions), designed the cells, wrote the cSAXS and P06 beamtime proposal drafts, wrote the ChemCatChem and JSynchrotronRadiat journal article drafts, carried out the simulations, prepared the in situ equipments (electrical contacts and gas connections), joined all the experiments at P06 (10-16 October 2017, 9-20 June 2018, 3-10 December 2018, 18-24 May 2019) and cSAXS beamtimes (25 February 2017, 6-10 March 2018, 4-9 April 2019), reconstructed some ptychograms and tomograms in Chapter 4, prepared the samples using FIB Strata 400S at the KIT-INT in Chapter 3 and FIB SCIOS at the DESY Nanolab in Chapter 4.
- Prof. Jan-Dierk Grunwaldt guided and discussed the experiment at cSAXS beamline (25 February 2017), provided the dissertation topic, guided on dissertation and preparation of journal articles, wrote and approved the cSAXS and P06 beamtime proposals, gave insight in designing the cells, provided the in situ equipments (MS, MFC, gas connections).
- Dr. Thomas Sheppard guided and discussed the experiments at P06 (10-16 October 2017, 9-20 June 2018, 3-10 December 2018, 18-24 May 2019) and cSAXS beamline (6-10 March 2018, 4-9 April 2019), guided in preparing journal articles and dissertation, wrote the cSAXS and P06 beamtime proposals, gave insight in designing the cells, prepared the in situ equipments (MS, MFC, gas connections).
- Mr. Johannes Becher helped in the experiments at the P06 beamline (10-16 October 2017, 9-20 June 2018, 3-10 December 2018, 18-24 May 2019) and wrote the ChemCatChem journal article.
- Mr. Sebastian Weber helped in the experiments at the P06 beamline (18-24 May 2019).
- Dr. Torsten Scherer and Dr. Peter Marek prepared the CeO_2/npAu samples for ET, PXCT, and FIB-SV measurements in Chapter 2 using focused ion beam Strata 400S at the INT-KIT. Dr. Torsten Scherer also wrote the ChemCatChem journal article.
- Dr. Wang Wu and Dr. Wang Di conducted ET measurements on npAu samples in Chapter 2 and 3 and TEM measurements in Chapter 4 using transmission electron microscope Titan 80-300 at the INT-KIT. They also wrote the ChemCatChem journal article.
- Mr. Dennis Scherhaufer and Mr. Heinz Lambach fabricated the *in situ* cells in Chapter 4 using micromachining instrument at the IMVT-KIT and wrote the JSnchrotronRadiat journal article.
- Dr. Patrice Brenner conducted the FIB-SV measurement in Chapter 2 using FIB EsB 1540 at the CFN-KIT and wrote the ChemCatChem journal article.
- Dr. Thomas Keller and Mr. Satishkumar Kulkarni provided access to FIB SCIOS at the DESY Nanolab, prepared the samples for experiments in Chapter 4, and wrote the JSnchrotronRadiat journal article.
- Dr. Andreas Schropp wrote the beamtime proposals, set up the infrastructure and helped in the in situ XRP and PXCT beamtimes at the P06 beamline (10-16 October 2017, 9-20 June 2018, 3-10 December 2018, 18-24 May 2019), , wrote the JSnchrotronRadiat journal article, and carried out most of the ptychographic and tomographic reconstructions in Chapter 4.
- Mr. Dennis Brükner set up the infrastructure, helped in the in situ XRP and PXCT beamtimes at the P06 beamline (10-16 October 2017, 9-20 June 2018, 3-10 December 2018, 18-24 May 2019), wrote the JSnchrotronRadiat journal article, and carried out the MLEM reconstruction in Chapter 4.
- Mr. Maik Kahnt set up the infrastructure, helped in the in situ XRP and PXCT beamtimes at the P06 beamline (10-16 October 2017, 9-20 June 2018, 3-10 December 2018), wrote the JSnchrotronRadiat journal article, and carried out the SART reconstruction in Chapter 4.

- Mr. Martin Seyrich and Mr. Felix Wittwer set up the infrastructure, helped in the in situ XRP and PXCT beamtimes at the P06 beamline (10-16 October 2017, 9-20 June 2018, 3-10 December 2018), wrote the JSnchrotronRadiat journal article, and carried out some ptychographic reconstructions in Chapter 4.
- Dr. Xiaogang Yang provided his original machine-learning algorithm to recontruct tomograms from the in situ limited-angle PXCT experiments at the P06 beamline (3-10 December 2018) and wrote the JSnchrotronRadiat journal article.
- Prof. Christian Schroer wrote the beamtime proposals, wrote the JSnchrotronRadiat journal article, provided the beamtime access and infrastructure at the P06 beamline (DESY).
- Dr. Ana Diaz, Dr. Johannes Ihli, Dr. Michal Odstrcil, and Dr. Mirko Holler set up the flOMNI instrument, reconstructed the PXCT data at the cSAXS beamline (25 February 2017, 6-10 March 2018, 4-9 April 2019), also wrote the ChemCatChem journal article. Dr. Ana Diaz also wrote the beamtime proposals for all experiments at the cSAXS beamline.
- Dr. Arne Wittstock provided nanoporous gold samples, wrote and submitted the KNMF proposal.
- Prof. Wilhelm Schwieger provided zeolite samples.
- Prof. Claus Feldmann provided cobalt-manganese-oxide hollow spheres samples.